universität innsbruck

Radio frequency control of a trapped-ion quantum network node

A master's thesis submitted to the faculty of mathematics, computer science and physics, of the University of Innsbruck in partial fulfilment of the requirements for the degree of

Master of Science (MSc)

carried out at the Institute of Experimental Physics
under the supervision of

assoc. Prof. Dr. Benjamin P. Lanyon,

presented by

Johannes Helgert

08.01.2024

Eidesstattliche Erklärung

Ich erkläre hiermit an Eides statt durch meine eigenhändige Unterschrift, dass ich die vorliegende Arbeit selbständig verfasst und keine anderen als die angegebenen Quellen und Hilfsmittel verwendet habe. Alle Stellen, die wörtlich oder inhaltlich den angegebenen Quellen entnommen wurden, sind als solche kenntlich gemacht. Die vorliegende Arbeit wurde bisher in gleicher oder ähnlicher Form noch nicht als Magister-/Master-/Diplomarbeit/Dissertation eingereicht.

Innsbruck, 08.01.2024 Johannes Helgert

Note: This version of the thesis was compiled after submitting and includes small corrections to the text and equations. No data or data analysis was changed.

Abstract

This master's thesis presents two implementations of radio frequency control for a quantum network node. The quantum network node is based on a string of single trapped atomic ions, held in a linear Paul trap with an integrated optical cavity. For the first radio frequency control implementation, a feedback loop was set up to stabilise the motional frequencies of the ions in the plane perpendicular to the string axis (radial modes). Stabilised radial mode frequencies open up the possibility of using them to mediate quantum logic gates in long ion strings. After stabilisation, a standard deviation of 35(3) Hz around a mean radial mode frequency of 2.682 342(10) MHz was observed for a single ion over one hour. Over such timescales, the stability is limited by fluctuations in the laboratory humidity and noise in the control electronics. The motional coherence time of a qubit stored in a radial motional mode was observed to be 13(1) ms, not limited by the surrounding 50 Hz power lines but by noise in the control electronics. This level of stability is sufficient for implementing quantum logic gates in future work.

For the second radio frequency control implementation, an antenna, capable of directly driving of the $^{40}Ca^{+}$ ground-state qubit at 11.62 MHz, was integrated into the quantum network node. Such a direct drive is expected to significantly improve the ground-state qubit's coherence time, providing the quantum network node with a long-lasting quantum memory. A Rabi frequency of $2\pi \cdot 8.637(6)$ kHz was achieved, limited to a large degree by the distance between the radio frequency antenna and the ion. The precision of the rotation angle of individual π-pulses was found to be in the 10^{-4} regime and power drifts in the antenna's drive circuit were identified as the dominant imperfection. When using the antenna to perform dynamical decoupling on the ground-state qubit, a Ramsey contrast of 0.81^{+9}_{-15} after 4.16 s was found. This represents a significant improvement over the best previous result in our system, in which a Ramsey contrast of 0.67(3) was observed after 66 ms, without the radio frequency antenna. Finally, the dynamically decoupled ground-state qubit is a quantum memory that can store arbitrary qubit states. A single qubit was stored over 4.16 s with an average fidelity of $F = 0.80^{+6}_{-10}$, proving that storage times of multiple seconds are now available in our quantum network node.

Zusammenfassung

Diese Masterarbeit beschreibt zwei Implementierungen von Radiofrequenz Steuerung eines Quantennetzwerkknotens. Der Quantennetzwerkknotens basiert auf einer Kette einzelner atomarer Ionen, gefangen in einer linearen Paul-Falle mit integriertem optischen Resonator. Die erste beider Implementierungen von Radiofrequenz-Steuerung ist der Aufbau einer Rückkopplungsschaltung um die Schwingungsfrequenzen der Ionen in der Ebene orthogonal zur Ionenkette zu stabilisieren (radiale Moden). Stabile radiale Modenfrequenzen eröffnen die Möglichkeit, diese zur Ausführung von Quantenlogik-Gattern in langen Ionenketten zu nutzen. Zukünftig sollen derartig stabilisierte Schwingungsfrequenzen die Ausführung von Quantenlogik-Operationen in der Ionenkette ermöglichen, welche die radialen Schwingungsmoden nutzen. Nach Stabilisierung wurde über einen Zeitraum von einer Stunde an einem einzelnen Ion eine Standardabweichung von 35(3) Hz um eine mittlere radiale Modenfrequenz von 2,682342(10) MHz gemessen. Auf diesen Zeitskalen ist die Stabilität sowohl durch Schwankungen in der Luftfeuchtigkeit im Labor, sowie durch Rauschen in der Steuerungselektronik limitiert. Die Kohärenzzeit eines Qubits, welches in einer radialen Schwingungsmode gespeichert ist, wurde auf 13(1) ms bestimmt. Diese Kohärenzzeit ist nicht durch den Einfluss des umgebenden 50 Hz Stromnetztes limitiert, jedoch durch Rauschen in der Steuerungselektronik. Dieses Stabilitätslevel ist ausreichend um in zukünftigen Arbeiten Quantenlogik-Gatter zu implementieren.

Die zweite beider Implementierung von Radiofrequenz-Steuerung ist die Integration einer Antenne in den Quantennetzwerkknoten, welche eine direkte Kopplung des $^{40}Ca^{+}$ Grundzustands-Qubits bei einer Frequenz von 11,62 MHz ermöglicht. Es wird erwartet, dass eine derartige direkte Kopplung die Kohärenzzeit des Grundzustands-Qubits verbessert und damit einen langlebigen Quantenspeicher für den Quantennetzwerkknoten bereitstellt. Die erreichte Rabi Frequenz von $2\pi \cdot 8{,}637(6)$ kHz ist hauptsächlich durch die Entfernung zwischen der Radiofrequenz-Antenne und dem Ion begrenzt. Die Genauigkeit des Rotationswinkels einzelner π-Pulse liegt im 10^{-4} Bereich und als dominierende Fehlerquelle wurden Leistungsabweichungen im Antennen-Schaltkreis identifiziert. Unter Nutzung der Antenne zur dynamischen Entkopplung des Grundzustand-Qubits wurde ein Ramsey Kontrast von $0{,}81^{+9}_{-15}$ nach 4,16 s ermittelt. Dies repräsentiert eine signifikante Verbesserung verglichen mit dem zuvor besten Ergebnis in unserem System, in welchem ein Ramsey Kontrast von 0,67(3) nach 66 ms ohne die Radiofrequenz-Antenne gemessen wurde. Abschließend ist das dynamisch entkoppelte Grundzustands-Qubit ein Quantenspeicher welcher beliebige Qubit-Zustände speichern kann. Ein Qubit wurde über 4.16 s mit einer durchschnittlichen Zustands-Ähnlichkeit von $F = 0.80^{+6}_{-10}$ gespeichert, was beweist dass Speicherzeiten von mehreren Sekunden nun in unserem Quantennetzwerkknoten verfügbar sind.

Acknowledgements

Here I like to thank every person who encouraged, helped and supported me during my studies in Innsbruck, especially during the time of my master.

I have to start with Ben Lanyon, my supervisor and the head of our experiment. He seemed excited from the point on where I asked him about possible projects and it never stopped. His clear vision in times of chaotic experiment results was one of the main reasons why the whole project worked out so smoothly for me. It was never a problem to discuss things, in particular if there was physics involved.

Although I am one of the very few master students in more than two decades of the Quantum Optics & Spectroscopy group who was not under supervision by Rainer Blatt, I cannot let him go unmentioned here. The scientific environment and the group of people he built up here in Innsbruck is hard to find elsewhere and made problem solving both easier and a team activity.

Those who helped me directly are my team members — the Mpreis gang — James Bate, Marco Canteri, Tabea Stroinski, Armin Winkler and Pascal Wintermeyer. Marco and James spent a solid amount of time together with me in the control room, sharing moments of confusion and success. Besides that, hanging out with you guys was always enjoyable and I wish you all the best for your continuing work at our experiment. Sitting in an office together with both of the experiment's postdocs Zhe "Zak" Xian Koong and comrade Viktor Krutianskii was a beyond helpful experience. Viktor never seemed to be tired of my endless questions on experimental details and he always delivered the enlightening answer I needed. Zak brought the vibe to the lab. Absolutely! His mood for doing some shenanigans is for sure something to remember when having a hard time in the lab.

A big contribution to the success of my projects also came from the next door 2D crystals lab in the person of postdoc Matthias Bock. He knows how to design proper electronics, how keep the lab tidy (the next door lab has always been the unmatched benchmark for experiment performance), but also how to set the record time for running up to Rauschbrunnen. Besides that he has always been open to share his deep insights and neat tricks for getting things running smoothly. I further have to thank Wolfgang Kuen and Kilian Prokop from the electronic workshop, providing me help for some specific electronics problems while on the administrative side Claudia Mevenkamp helped me sorting out the non-scientific aspects.

This thesis certainly took its time, especially towards the end when I had to work on it remotely. I'm very grateful that Ben was up for such an odd ending and that despite the delays, I already got the opportunity to start my work at the VU in Amsterdam. Thank you for your patience Laura and Kjeld!

I also want to thank all the studying colleagues I met through the years in and around Innsbruck who proved that there is a life outside the university. Specifically Luca Mastrangelo as well as the circle of people around him made the final year insanely fun. You guys have always been up for a proper rave, no matter if at Emma, Cubique or elsewhere.

Also my east German friends from home, Grybsch, Köhlex, Kobster and Freytag from Team Quattro Formaggi, have earned their place here. They poned[1] me when things got too serious but have also been there for the occasional deep talk.

Finally I want to say thank you to my family for all the support throughout the years, in particular my grandparents, my uncle Lars, my siblings and of course my parents Claudia and Michael. Especially my dad has been responsible for me falling back in love with science again during troubled times.

They all made this whole journey possible. The fun has just started...

[1]Yes, not phoned, you read it correctly. Because when I say Ponis, I really do mean this.

Contents

1. Introduction

The first quantum revolution in the mid-20th century brought arguably one of the biggest technological advancements in human history [1]. Inventions like the laser, the atomic clock, and the transistor enabled large scale industrial applications that had tremendous impact on the development of the globalised society that we live in today [2]. Modern information and communication technology relies on those three inventions. Transistors, as microscopic electronic logical elements, form large scale information processing units, commonly known as computers [3]. Multiple local computers are connected for the exchange of information in a global network, the internet, whose communication channels are to a large degree implemented by laser light in optical fibres [4]. The complete network is time-synchronised by a frequency standard provided from several atomic clocks [5].

Lasers, atomic clocks and transistors, referred to below as *classical* technology, are only the inception of technological developments that rely on quantum physics. In this classical technology, the potential of quantum mechanics has not been fully exploited, justifying the term *first* quantum revolution. A second quantum revolution has started already more than three decades ago, which goes that step further by making use of the properties of individual quantum systems [6]. The basic research field that underpins the emerging technology of the second quantum revolution is called *quantum information science*. Theoretical studies predict that the encoding of information directly into a quantum system is capable of yielding technologies and devices that outperform the best known classical technology in the areas of computation [7], simulation [8, 9], communication [10] and metrology [11]. Overcoming the challenges of putting these theoretical ideas into practice has been, and continues to be, the central goal of quantum information science. During recent years, the first experiments with quantum technologies that outperform conventional ones have been demonstrated [12, 13, 14], motivating the ongoing efforts to make the next generation of quantum technology a reality.

One of the goals is building the quantum analogy of the internet [15]. Even on smaller scales, such *quantum networks* have applications proposed in some of the mentioned four key areas of quantum information science. To overcome scalability problems in quantum computing, a modular architecture was suggested, requiring a local quantum network of multiple processors [16]. It is expected that such a scalable quantum processor is also able to perform digital quantum simulation [9].

In the area of metrology, it has been shown that using quantum states as sensors increases the precision [17]. There also already exist classical networks of clocks [18] which, combined with quantum states as sensors, will enable distributed quantum sensing [19]. Quantum

networks of clocks have been proposed for the detection of mass flows under the earth's crust to monitor seismic activities [20] using the methods of relativistic geodesy [21]. Further, the current limitation for the separations in interferometric telescope arrays could be overcome by sharing a non-local entangled quantum state between individual telescopes [22].

In communication, there is a need to close the security gap emerging from algorithms for quantum computers [23] that undermine widely used classical security protocols [24]. A possible solution is to use a quantum scheme based on non-local entangled states for the distribution of cryptographic keys - a method proven to be fundamentally secure [25]. The variety of proposed protocols for quantum key distribution makes communication a highly promising application of quantum networks. Developing methods to faithfully establish and distribute entanglement to remote locations is one of the main foci of current research that aims to realise quantum networks.

During the past decades of experimental quantum information research, several different physical platforms were investigated, including superconducting circuits [26], solid state spins [27], photonic systems [28], neutral atoms [29] and trapped atomic ions [30, 31]. The latter was found to offer an exceptional versatility for all the above mentioned key areas of quantum information applications. For quantum networks, the connection between individual nodes must be established by a flying quantum system, naturally chosen to be a single photon [32]. Quantum network nodes therefore require an interface for coupling the locally-stored and processed information to a single photon, which has been achieved by different trapped-ion implementations [33, 34]. Quantum networks of two remote ions in different traps, in the same laboratory [35] as well as, in our group, between different buildings [36], have demonstrated the basic functionality of remote entanglement. Similar capabilities have also been demonstrated with quantum networks of neutral atoms [37] and solid-state vacancy centres [38]. For most of the mentioned future applications, larger node separations are required, spanning from inter-city to global distances. To transmit photons over those distances, the existing infrastructure of classical communication in the form of optical fibres can be used. However in the quantum case, photon absorption, even when minimised at the telecom-wavelength [39], is a serious problem. Unlike classical information, a quantum state cannot be copied, preventing direct amplification of quantum states to overcome loss [40].

The most promising solution to this problem is the concept of *quantum repeaters*. Quantum repeaters split up a network link into individual segments and establish the entanglement on the shorter links, before swapping the entanglement out to being across the entire channel [41]. The original proposal stated two requirements for a quantum repeater: First, the repeater needs an interface between stationary matter qubits and photons, preferably at the telecom-wavelength to enable longer communication channels. Second, the repeater has to include a memory which is capable of storing quantum states significantly longer than the time needed to establish entanglement on one adjacent segment. In addition to these two requirements, it was suggested that a quantum repeater will benefit from having deterministic quantum information processing capabilities as these enable entanglement

distillation techniques [10]. In 2023[1], these requirements were demonstrated in a trapped-ion implementation of a quantum repeater node by the Distributed Quantum Systems group at the University of Innsbruck [42], where I carried out my master's thesis. The work presented in this thesis is aimed at extending the capabilities of the quantum network node that was used for this trapped-ion quantum repeater demonstration. The presented work consists of two projects, both relying heavily on radio frequency (RF) technology.

The first project is about stabilising the frequencies of the ion string's radial motional modes, motivated by the desire to increase the number of ions over which we can perform quantum logic gates. To increase the number of ions to ten or more, we need to relax the trap confinement in the axial direction in order to keep the ion string linear. Entangling operations based on coherent motional excitation will slow down when lowering the used motional mode frequency [43]. Further, their fidelity reduces due to increased heating rates and off-resonant excitation. Using radial instead of axial motional modes retains fast high-fidelity entangling operations. However, the radial modes' frequencies were previously not stable enough for coherent operations in our network node. Drifts of 6 kHz during approximately 10 min around a centre-of-mass radial mode frequency of 2.3 MHz were measured by PhD student Marco Canteri in May 2022. The goal for the first project is to reduce the frequency changes to less than 100 Hz over one hour. Further, it should be tested if the radial motional modes can be driven coherently and limitations should be identified.

The goal of the second project is to significantly extend the coherence time of the quantum memory in our network node. In our experiment, the quantum memory is implemented by the $^{40}Ca^{+}$ ground-state qubit [42], which is directly coupled by a magnetic dipole transition in the radio frequency regime. At this transition frequency, spontaneous emission is strongly suppressed compared to optical transitions [44]. Previously, we were not able to drive the ground-state qubit directly at radio frequency, but instead used laser pulses to manipulate its state indirectly. Our group achieved a ground-state qubit coherence time of 108 ms with a Ramsey contrast of 0.67(3) measured after 66 ms (see supplementary material of [42]), which limited the key performance metrics of the quantum repeater demonstration in that paper. The 108 ms coherence time was achieved using a sequence of laser pulses to implement dynamical decoupling [45] on the ground-state qubit. Errors in those pulses, due to the coupling of the laser field to the ion's motional state, were found to be a leading contribution to the finite coherence time. An appealing solution is to implement the dynamical decoupling pulses using radio frequency pulses, which do not couple to the ion's motional state. As such, the second project within this master's thesis is to set up and characterise a direct RF drive for the $^{40}Ca^{+}$ ground-state qubit.

[1]Published in May 2023. The measurements were already carried out in March 2021.

The structure of this document is as follows: The theoretical framework for the thesis is presented in Chapter 2, starting with a section introducing the mathematical description of quantum bits (qubits), followed by an overview of the theory of linear Paul traps, the relevant atomic level structure of $^{40}Ca^{+}$ and the interaction of a trapped ion with electromagnetic fields. After these sections, the basic principles and description of alternating current electronic circuits are introduced. The final section of the theoretical framework introduces a method for measuring a qubit's coherence, discusses the influence of environmental noise on the coherence, and presents a method for suppressing such noise. Chapter 3 presents the experimental setup as it existed when I started my master's project, as well as established relevant experimental methods. Chapters 4 and 5 present the two projects, namely the stabilisation of the radial motional mode frequencies in our ion trap, and the implementation of a direct RF drive for the $^{40}Ca^{+}$ ground-state qubit, respectively. These chapters first introduce the corresponding setup and hardware before presenting characterisation measurements and their results. Chapter 5 concludes with a section that reports on additional measurements which investigate the ground-state qubit's coherence using the RF drive. Chapter 6 presents a summary and outlook for future developments of the experiment in the context of the new capabilities developed in this thesis. The appendix is divided into chapters covering details of experimental setups, information on additional measurements and details of advanced analysis methods that have been used.

2. Theoretical concepts

2.1. Quantum bits

State vectors

Information is encoded in physical systems [46]. For information encoded into a physical two-level system that is accurately described by classical physics, the fundamental unit of information is the bit. A bit is either in the state 0 *or* the state 1. For information encoded into a two-level quantum system, the fundamental unit of information is called the quantum bit - in short *qubit*. An arbitrary qubit state can be expressed as a *superposition*

$$|\psi\rangle = \alpha|0\rangle + \beta|1\rangle \tag{2.1}$$

of orthogonal basis states

$$|0\rangle = \begin{pmatrix} 1 \\ 0 \end{pmatrix} \qquad \text{and} \qquad |1\rangle = \begin{pmatrix} 0 \\ 1 \end{pmatrix} \tag{2.2}$$

where α and β are complex numbers with the normalisation constraint $|\alpha|^2 + |\beta|^2 = 1$ [40]. An alternative parametrisation in spherical coordinates is given by

$$|\psi\rangle = e^{i\gamma}\left(\cos\left(\frac{\vartheta}{2}\right)|0\rangle + e^{i\varphi}\sin\left(\frac{\vartheta}{2}\right)|1\rangle\right) \tag{2.3}$$

with polar and azimuthal angles φ and ϑ, respectively, and a global phase γ which plays no role in the outcome of any measurement of the qubit. Such a parametrisation allows for a visual representation on the so called *Bloch sphere* [47] as shown in Figure 2.1a. The poles of the Bloch sphere at ± 1 on the z-axis represent the basis states of the logical basis $|0\rangle$ and $|1\rangle$. Two other bases that are orthonormal in the qubit's state space are formed by the basis states

$$|\pm\rangle = \frac{1}{\sqrt{2}}(|0\rangle \pm |1\rangle) \quad \text{and} \quad |\pm i\rangle = \frac{1}{\sqrt{2}}(|0\rangle \pm i|1\rangle). \tag{2.4}$$

The states $|+\rangle$ and $|-\rangle$ sit on the equator of the Bloch sphere at ± 1 on the x-axis. The states $|+i\rangle$ and $|-i\rangle$ sit on the equator of the Bloch sphere at ± 1 on the y-axis.

State evolution

An initial single qubit state $|\psi_0\rangle$ is converted into another state $|\psi\rangle$ via a two-by-two unitary operator $\hat{U}$ by

$$|\psi\rangle = \hat{U}|\psi_0\rangle. \tag{2.5}$$

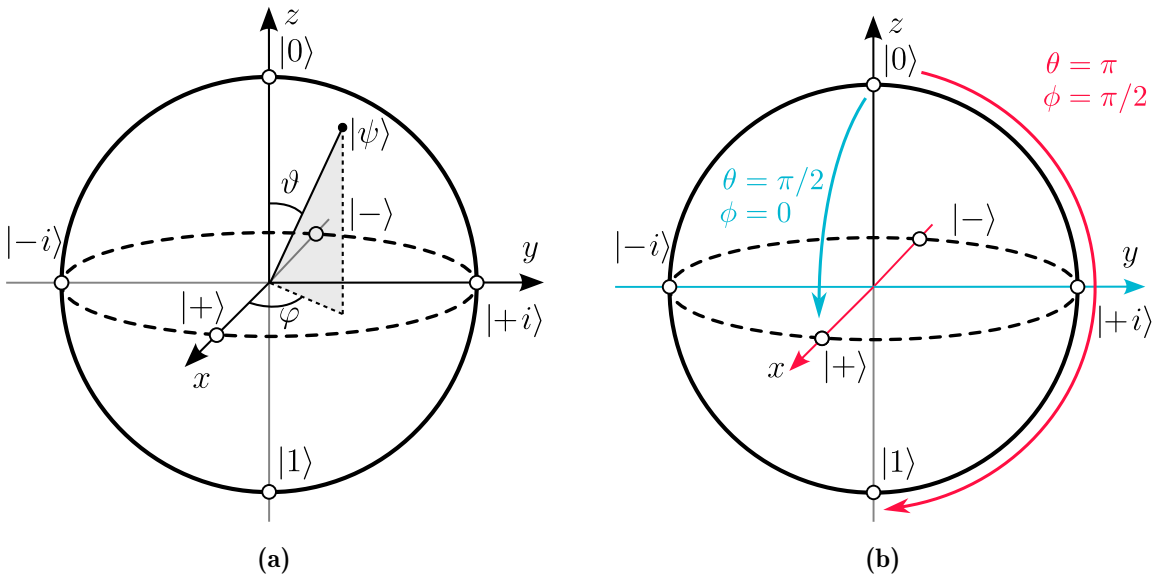

Figure 2.1.: a) Bloch sphere with qubit state vector $|\psi\rangle$ at azimuthal angle ϑ and polar angle φ. Canonical basis states are indicated at the intersections between axes and the sphere surface. **b)** Visualisation of rotations based on the unitary from Equation 2.8, starting in the state $|0\rangle$. Setting $\phi = 0$ rotates around the y-axis (blue). Setting $\phi = \pi/2$ rotates around the x-axis (red). For $\theta = \pi/2$, the state $|0\rangle$ at the pole is rotated to the equator at $|+\rangle$, for $\theta = \pi$ a full flip to the opposite pole with the state $|1\rangle$ is performed.

Such unitary operators of qubit states can be seen as *rotations* on the Bloch sphere as exemplified in Figure 2.1b. Rotations around the canonical axes of the Bloch sphere are generated by the Pauli matrices

$$\begin{aligned}
\hat{\sigma}_\mathrm{X} &= \begin{pmatrix} 0 & 1 \\ 1 & 0 \end{pmatrix} = |+\rangle\langle+| - |-\rangle\langle-|, \\
\hat{\sigma}_\mathrm{Y} &= \begin{pmatrix} 0 & -i \\ i & 0 \end{pmatrix} = |+i\rangle\langle+i| - |-i\rangle\langle-i|, \\
\hat{\sigma}_\mathrm{Z} &= \begin{pmatrix} 1 & 0 \\ 0 & -1 \end{pmatrix} = |0\rangle\langle0| - |1\rangle\langle1|
\end{aligned} \tag{2.6}$$

and are represented by the unitaries

$$\hat{U}_\mathrm{X}(\theta) = e^{-i\theta\hat{\sigma}_\mathrm{X}/2} \quad , \quad \hat{U}_\mathrm{Y}(\theta) = e^{-i\theta\hat{\sigma}_\mathrm{Y}/2} \quad \text{and} \quad \hat{U}_\mathrm{Z}(\theta) = e^{-i\theta\hat{\sigma}_\mathrm{Z}/2} \tag{2.7}$$

where θ is the rotation angle. A rotation with angle θ around an arbitrary axis in the xy-plane angled at ϕ to the y-axis is given by

$$\hat{U}_{\mathrm{X,Y}}(\theta, \phi) = e^{-i\theta(\cos(\phi)\hat{\sigma}_\mathrm{Y} - \sin(\phi)\hat{\sigma}_\mathrm{X})/2} \tag{2.8}$$

which becomes relevant for the implementation of single qubit rotations described in Section 2.3.3. Any two rotations out of the set in Equation 2.7 are sufficient to construct an

arbitrary rotation as a series of three of such rotations [48]. Throughout this thesis, a rotation of the form in Equation 2.8 with angle $\theta = \pi$ will be called a π-*pulse* and a rotation with angle $\theta = \pi/2$ will be called a $\pi/2$-*pulse*.

Projective measurements

A special case of measurements in quantum mechanics are *projective measurements*. A projective measurement is described by an observable $\hat{M}$ in the qubit's state space. The observable is decomposed into a linear combination of its eigenvalues m with a set of projectors $\{\hat{P}_m\}$ by

$$\hat{M} = \sum_m m\hat{P}_m. \tag{2.9}$$

These projectors have to fulfil the completeness relation $\sum_m \hat{P}_m = \hat{I}$ with the identity $\hat{I}$, reflecting the fact that the probabilities for all measurement outcomes have to sum up to one, that is: $\sum_m p_m = 1$. Further, the projectors have to be orthogonal such that $\hat{P}_m\hat{P}_n = \delta_{m,n}\hat{P}_m$ where $\delta_{m,n}$ is the Kronecker delta. With these conditions, the projectors can be expressed using the observable's eigenstates $|m\rangle$ by $\hat{P}_m = |m\rangle\langle m|$. The probability to find the eigenvalue m as the projective measurement's outcome is given by

$$p_m = \langle\psi|\hat{P}_m|\psi\rangle \tag{2.10}$$

and after the measurement, the state is projected into the outcome state

$$\frac{\hat{P}_m}{\sqrt{p_m}}|\psi\rangle = |m\rangle. \tag{2.11}$$

The expectation value of the observable can then be written as

$$\langle\hat{M}\rangle = \langle\psi|\hat{M}|\psi\rangle. \tag{2.12}$$

Density matrices

If the qubit is part of an open quantum system, as in any implementation in the laboratory, a more general definition of its state is given by the *density matrix* formalism [49]. A density matrix can be written as a statistical mixture

$$\hat{\rho} = \sum_{i=0}^{N} p_i|\psi_i\rangle\langle\psi_i| \tag{2.13}$$

of N different states $|\psi_i\rangle$ which are found with probabilities p_i. Quantum states represented by ket vectors like in Equation 2.1 are included in the density matrix formalism as a subset for $N = 1$, $p_0 = 1$, and are henceforth called *pure* states. The purity of a state is defined by $P = \mathrm{Tr}(\hat{\rho}^2)$ which for pure states yields a value of 1. In the case of $P < 1$, the state is henceforth called a *mixed* state. Compared to a pure state, which has a unit length vector

in the picture of the Bloch sphere, the length of a mixed state's Bloch sphere vector is reduced. Time evolution of a density matrix $\hat{\rho}_0$ under a unitary $\hat{U}$ is given by

$$\hat{\rho}(t) = \hat{U}(t)\hat{\rho}_0\hat{U}^\dagger(t). \tag{2.14}$$

The unitaries from Equation 2.7 remain valid for expressing rotations around the Bloch sphere's canonical axis. For density matrices, the formalism of projective measurements extends in the following way: The probability to find the eigenvalue m as the projective measurement's outcome is given by

$$p_m = \mathrm{Tr}(\hat{P}_m\hat{\rho}) \tag{2.15}$$

and after the measurement, the state is projected into the outcome state

$$\frac{\hat{P}_m\hat{\rho}\hat{P}_m}{p_m} = |m\rangle\langle m|. \tag{2.16}$$

The expectation value of the observable $\hat{M}$ is then expressed by

$$\langle\hat{M}\rangle = \mathrm{Tr}(\hat{M}\hat{\rho}). \tag{2.17}$$

State tomography

The density matrix of a single qubit can be written as a linear combination of the identity $\hat{I}$ and the Pauli matrices (Equation 2.6) with their expectation values as

$$\hat{\rho} = \frac{1}{2}(\langle\hat{I}\rangle\hat{I} + \langle\hat{\sigma}_\mathrm{X}\rangle\hat{\sigma}_\mathrm{X} + \langle\hat{\sigma}_\mathrm{Y}\rangle\hat{\sigma}_\mathrm{Y} + \langle\hat{\sigma}_\mathrm{Z}\rangle\hat{\sigma}_\mathrm{Z}). \tag{2.18}$$

Inserting the projector notation of the Pauli matrices from Equation 2.6 and $\hat{I} = |0\rangle\langle 0| + |1\rangle\langle 1|$ gives terms that are identified by Equation 2.15 as the probabilities for obtaining as projective measurement outcome the basis states $|0\rangle$, $|1\rangle$, $|+\rangle$, $|-\rangle$, $|+i\rangle$ and $|-i\rangle$. That is:

$$\begin{aligned}
\langle\hat{I}\rangle &= \mathrm{Tr}(|0\rangle\langle 0|\hat{\rho}) + \mathrm{Tr}(|1\rangle\langle 1|\hat{\rho}) = p_0 + p_1 \\
\langle\hat{\sigma}_\mathrm{X}\rangle &= \mathrm{Tr}(|+\rangle\langle +|\hat{\rho}) - \mathrm{Tr}(|-\rangle\langle -|\hat{\rho}) = p_+ - p_- \\
\langle\hat{\sigma}_\mathrm{Y}\rangle &= \mathrm{Tr}(|+i\rangle\langle +i|\hat{\rho}) - \mathrm{Tr}(|-i\rangle\langle -i|\hat{\rho}) = p_{+i} - p_{-i} \\
\langle\hat{\sigma}_\mathrm{Z}\rangle &= \mathrm{Tr}(|0\rangle\langle 0|\hat{\rho}) - \mathrm{Tr}(|1\rangle\langle 1|\hat{\rho}) = p_0 - p_1.
\end{aligned} \tag{2.19}$$

The single qubit density matrix can then be expressed by

$$\hat{\rho} = \begin{pmatrix} p_0 & (p_+ - p_- + ip_{+i} - ip_{-i})/2 \\ (p_+ - p_- - ip_{+i} + ip_{-i})/2 & p_1 \end{pmatrix}. \tag{2.20}$$

In an experimental setting that allows for the preparation of multiple copies of an unknown state $\hat{\rho}$, the probabilities p_0, p_1, p_+, p_-, p_{+i} and p_{-i} can be estimated from repeated experiments with projective measurements. The quantum state $\hat{\rho}$ can then be reconstructed.

The process of the reconstruction of a quantum state, via the estimation of the probabilities shown in Equation 2.20, is known as *quantum state tomography* [50]. More information on commonly used methods for quantum state tomography is given in Appendix C.2.

A measure for comparing a reconstructed state in the laboratory $\hat{\rho}_{\text{lab}}$ with an ideal state $\hat{\rho}_{\text{th}}$ is the *fidelity*, defined as [51]

$$F(\hat{\rho}_{\text{lab}}, \hat{\rho}_{\text{th}}) = \text{Tr}\left(\sqrt{\sqrt{\hat{\rho}_{\text{lab}}}\hat{\rho}_{\text{th}}\sqrt{\hat{\rho}_{\text{lab}}}}\right)^2. \tag{2.21}$$

Fidelity of $F = 1$ represents identical states $\hat{\rho}_{\text{lab}}$ and $\hat{\rho}_{\text{th}}$, while for $F = 0$ the states $\hat{\rho}_{\text{lab}}$ and $\hat{\rho}_{\text{th}}$ are orthogonal.

Multiple qubits

This thesis presents experiments done with only a single qubit. However, it is worth pointing out a few basic considerations when introducing more qubits since this is where quantum information processing becomes particularly powerful. For two qubits, the logical basis vectors for the state space are given by $|00\rangle, |11\rangle, |01\rangle$ and $|10\rangle$. For N qubits, there are 2^N basis vectors, corresponding to the number of possible combinations of N qubits being either in $|0\rangle$ or $|1\rangle$. Specifying an arbitrary N-qubit superposition state therefore requires specifying all 2^N complex parameters of these basis vectors. It is this exponential scaling which makes simulating large quantum systems impractical on a classical computer. Furthermore, there is strong evidence that encoding and processing information in such a vast state space allows for speeding up finding the solution to certain problems [23, 52, 53]. As the topic of quantum computation and corresponding algorithms goes beyond the scope of this thesis, I refer to [40] for more information on that subject.

What is further intriguing when dealing with multiple qubits is that there exist superposition states which cannot be written in the form $|\psi_1\rangle \otimes |\psi_2\rangle$ where $\otimes$ denotes the tensor product. These are called *entangled* states and the most prominent examples are the four Bell states of two qubits [40]

$$|\Phi_\pm\rangle = \frac{1}{\sqrt{2}}(|00\rangle \pm |11\rangle), \qquad |\Psi_\pm\rangle = \frac{1}{\sqrt{2}}(|01\rangle \pm |10\rangle). \tag{2.22}$$

When measuring the logical state of one of the two participating qubits, the outcome perfectly defines the other qubit's state. Furthermore, such correlations are not restricted to just the logical basis but remain when measuring in any other basis. These correlations have so far proven to be independent of the physical distance between the two qubits, motivating their use for secure communication [10].

2.2. Linear Paul traps

A possible option for implementing a qubit is to use the electronic states of single charged atoms confined in space [30]. For charged atoms, strong potentials with respect to typical kinetic energies can be produced using electric fields [54]. Such electric potentials are independent of the atom's internal electronic state. In order to confine a particle in a given dimension, a potential minimum has to be produced in that dimension. Earnshaw's theorem [55] states that it is not possible to create confinement simultaneously in three dimensions using static electric fields. Two techniques have been developed to circumvent the problem and allow charged particles to be effectively trapped in three dimensions. One can either use additional magnetic fields, forming a *Penning trap* [56], or introduce a time dependence for parts of the electric potential. The latter case is the foundation for *Paul traps* [57], which will be discussed in this section and is used in our experimental setup.

Figure 2.2a shows a schematic drawing of an example of a linear Paul trap. The z-axis is referred to as the *axial direction* and the xy-plane perpendicular to it is also called the *radial plane*. The trap's potential has a time-independent (DC) part

$$\Phi_{\mathrm{DC}}(x,y,z) = \frac{V_{\mathrm{DC}}}{2d_0^2}(2z^2 - x^2 - y^2), \tag{2.23}$$

which is produced by electrodes that are spaced by $2d_0$ along the z-axis, both at a voltage V_{DC}. Additionally, a time dependent (AC) part oscillating at a radio frequency Ω is produced by four *radial* electrodes in the radial plane. The radial electrodes are extruded along the z-axis and diagonal radial electrodes have a distance of $2r_0$. In many linear Paul traps, one pair of diagonal electrodes is set to an oscillating voltage with maximum amplitude V_{RF} and the other pair is kept at electrical ground[1]. The potential produced by the radial electrodes is given by

$$\Phi_{\mathrm{AC}}(x,y,z,t) = \frac{V_{\mathrm{RF}}}{2r_0^2}(x^2 - y^2)\sin(\Omega t). \tag{2.24}$$

At every point in time, the configuration of the radial electrodes forms a quadrupole potential for every axial position z, as exemplified in Figure 2.2b.

An atom at the position $\vec{r}(t)$ with mass m and charge Q moves in the superposition of the two potentials according to

$$m\frac{\mathrm{d}^2}{\mathrm{d}t^2}\vec{r}(t) = \vec{F}(\vec{r}(t),t) = -Q\vec{\nabla}(\Phi_{\mathrm{DC}}(x,y,z) + \Phi_{\mathrm{AC}}(x,y,z,t)). \tag{2.25}$$

The general method to solve for the atom's motion transforms Equation 2.25 to the form of the Mathieu equation [58], also yielding stability criteria based on the atom's charge-to-mass ratio [54]. The derivation for the trapping frequencies presented here follows the

[1] Typically, the electrical ground at the radial electrodes is lifted from the ground reference of the DC electrodes. The potential in the radial plane then becomes slightly asymmetric and leads to different oscillation frequencies of trapped particles in directions along the x and y axes.

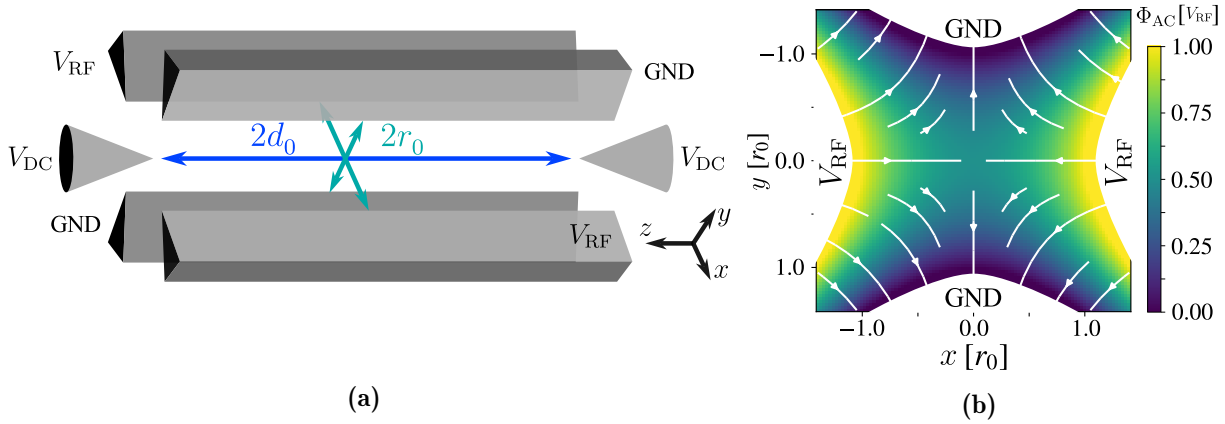

Figure 2.2.: a) Schematic drawing of a linear Paul trap. Electrodes (grey blocks) are labelled with their applied voltages. Electrode distances in the axial direction and the radial plane are indicated by the blue arrows. **b)** Contour plot of the radial electrode's quadrupole potential Φ_{AC} in the radial plane. The white lines with arrows indicate the direction of the electric field.

pseudopotential approach [59], which is equivalent to the lowest order approximation of the Mathieu equation solution: At the potential minimum in axial direction at $z \approx 0$, the atom's radial motion is split up into a slower part $\vec{r}(t)$ (secular motion) and a faster part $\vec{\xi}(t)$ (micromotion). The first step is to solve for the micromotion dynamics, for which the *secular approximation* is made [54]. In the secular approximation, the amplitude of micromotion is significantly smaller than the amplitude of the secular motion and the spatial dependence of the force can then be neglected, yielding the equation of motion

$$m\frac{\mathrm{d}^2}{\mathrm{d}t^2}\vec{\xi}(t) = \vec{F}(\vec{r}, t). \tag{2.26}$$

Integrating twice yields

$$\vec{\xi}(t) = \frac{QV_{RF}}{m\Omega^2 r_0^2}\sin(\Omega t)\begin{pmatrix}\bar{x}\\ -\bar{y}\\ 0\end{pmatrix}. \tag{2.27}$$

Micromotion therefore vanishes at the trap centre and increases with the displacement in the radial plane. The second step is to solve for the secular motion $\vec{r}(t)$ using the time-averaged force at a displacement $\vec{r}$ which is

$$\bar{\vec{F}}(\vec{r}) = \langle \vec{F}(\vec{r}, t)\rangle. \tag{2.28}$$

When plugging in the time varying potential Φ_{AC} and Equation 2.27, the time-averaged force becomes

$$\bar{\vec{F}}(\vec{r}) = -\begin{pmatrix}k_r\bar{x}\\ k_r\bar{y}\\ k_z\bar{z}\end{pmatrix} \tag{2.29}$$

with

$$k_r = \frac{QV_{DC}}{d_0^2} - \frac{Q^2V_{RF}^2}{2mr_0^4\Omega^2} \quad \text{and} \quad k_z = \frac{2QV_{DC}}{md_0^2}. \tag{2.30}$$

The force $\vec{F}(\vec{r})$ scales linear with the displacements $\bar{x}$, $\bar{y}$ and $\bar{z}$, therefore producing a harmonic oscillation in the radial and axial trap directions. The axial secular angular frequency ω_z and the radial secular angular frequency $\widetilde{\omega}_r$ are given by

$$\omega_z = \sqrt{\frac{k_z}{m}} = \sqrt{\frac{2QV_{DC}}{md_0^2}} \tag{2.31}$$

and

$$\widetilde{\omega}_r = \sqrt{\frac{k_r}{m}} = \sqrt{\omega_r^2 - \frac{1}{2}\omega_z^2} \tag{2.32}$$

with

$$\omega_r = \frac{QV_{RF}}{\sqrt{2}mr_0^2\Omega}. \tag{2.33}$$

If the charge-to-mass ratio of atoms fulfils the trap's stability criteria [54], multiple charged atoms with the same polarity arrange along the z-axis and, by repelling each other, form an ion string.

2.3. Atomic physics

Utilising the techniques from the previous section, atomic ions can be confined spatially, allowing their internal degrees of freedom to be addressed. The internal energy levels of individual atomic ions can be used for encoding information, allowing for quantum information processing [40]. This section first gives an example for the energy level structure in a singularly-ionised alkaline-earth atom, then describes how the atom's motional and electronic state can be manipulated by electromagnetic radiation.

2.3.1. Level structure of $^{40}Ca^+$

There are several choices of ion species to use for quantum information experiments. Singularly-ionised alkaline-earth atoms have proven to be suitable for such experiments [16, 31]. As they only have a single outer valence electron, such ions exhibit properties similar to the neutral hydrogen atom, which is a well known physical system [44]. An energy level diagram of the single outer valence electron of $^{40}Ca^+$ is shown in Figure 2.3.

The lowest energy level manifold of the $^{40}Ca^+$ ion is $4^2S_{1/2}$, where the subscript denotes the angular momentum quantum number J. The orbitals with the next higher energies are 3^2D and 4^2P with each consisting of two fine structure manifolds due to coupling of the electron's spin and its orbital angular momentum. In the case of a nuclear spin, there also emerges a hyperfine structure from coupling between nuclear spin and angular momentum of the outer valence electron. However, $^{40}Ca^+$ has no nuclear spin. Transitions from 4^2S to 4^2P and from 3^2D to 4^2P are based on an electric dipole interaction. Transitions from 4^2S to 3^2D are based on an electric quadrupole interaction. The lifetime of the $3^2D_{5/2}$ state is 1.15 s, giving a linewidth of $\Gamma = 2\pi \cdot 0.138\,\mathrm{Hz}$ [61]. The lifetime of the $4^2P_{1/2}$ state is

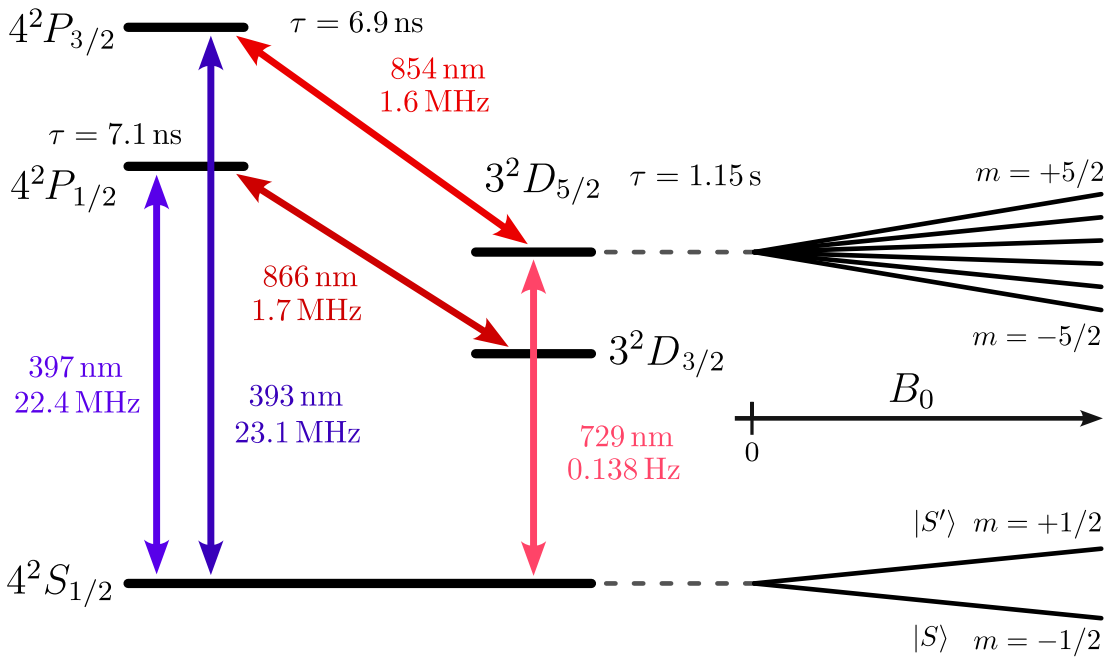

Figure 2.3.: Energy level diagram of $^{40}Ca^+$. Relevant transitions for experiments presented in this thesis are indicated and labelled with their wavelengths and linewidths. Lifetimes of excited states are indicated. By applying an external magnetic field with strength B_0, the fine structure levels split up due to the Zeeman effect which produces a linear shift in energy for small fields (see main text for the meaning of *small* in this context). Zeeman splittings are only shown for the excited $3^2D_{5/2}$ manifold and the $4^2S_{1/2}$ ground-state manifold, for which the individual Zeeman states are also labelled as $|S\rangle$ and $|S'\rangle$. Transition line data is taken from [60, 61, 62].

7.1 ns, giving a linewidth of $\Gamma = 2\pi \cdot 22.4\,\mathrm{MHz}$ [60]. The broad linewidth of the 4^2S to 4^2P transitions makes them favourable for Doppler cooling and fluorescence detection [54]. The narrower linewidths of the quadrupole transitions from 4^2S to 3^2D on the other hand are well suited for precision spectroscopy or encoding a qubit in the participating states. A cooling cycle that is disconnected from the qubit's excited D-state can be implemented by encoding the qubit in one Zeeman sublevel each in $4^2S_{1/2}$ and $3^2D_{5/2}$.

In the presence of an external magnetic field, the level structure is further split due to the field's interaction with the electron's spin. The result of this so called *Zeeman-effect* [44] is that fine structure levels split up into $2J + 1$ Zeeman-levels. Each Zeeman-level is characterised by its magnetic quantum number m_J. For small magnetic fields, meaning that the interaction between the electron spin and the magnetic field is much weaker than spin-orbit interaction, the energy shift is proportional to the magnetic field strength B_0. The energy difference from the Zeeman shift is given by

$$\Delta E = -\mu_\mathrm{B} g_J m_J B_0 \tag{2.34}$$

where μ_B is the Bohr magneton and g_J is the Landé g-factor, which depends the fine structure level [63]. The Zeeman-splitting of the $4^2S_{1/2}$ and $3^2D_{5/2}$ states is shown in the

right part of Figure 2.3. In the case of the ground-state $4^2S_{1/2}$, g_J becomes the Landé g-factor of a single electron g_e. The literature value of g_e is known up to 15 significant digits [63] but for all calculations in this thesis the rounded value of $g_e = -2.002$ was used. For a magnetic field strength B_0, the frequency splitting of the ground-state's two Zeeman states $|S\rangle$ and $|S'\rangle$ is then given by

$$\omega_0 = 2\pi\nu_0 = (\Delta E_{m=1/2} - \Delta E_{m=-1/2})/\hbar = 2\pi \cdot 2.802\,\mathrm{MHz\,G^{-1}} \cdot B_0 \tag{2.35}$$

where $\hbar$ is the reduced Planck constant [64]. For a magnetic field of $B_0 = 4.148\,\mathrm{G}$, the value used in the experiments presented in this thesis, the splitting is $\omega_0 = 2\pi \cdot 11.62\,\mathrm{MHz}$.

2.3.2. Trapped two-level atom interacting with electromagnetic radiation

In an atom, internal energy levels with a spacing of ΔE can be coupled by electromagnetic radiation at a frequency $\omega_0 = \Delta E/\hbar$ where $\hbar$ is the reduced Planck constant [64]. A two-level atom with energy difference $\hbar\omega_0$ between a ground-state $|g\rangle$ and excited state $|e\rangle$ can be modelled by the Hamiltonian [65]

$$\hat{H}_\mathrm{A} = \frac{\hbar\omega_0}{2}\hat{\sigma}_\mathrm{Z}. \tag{2.36}$$

The motion of an atom in a harmonic trap potential with secular frequency ω_T in one dimension is described quantum mechanically with a Hamiltonian

$$\hat{H}_\mathrm{M} = \hbar\omega_\mathrm{T}\left(\frac{1}{2} + \hat{a}^\dagger\hat{a}\right) \tag{2.37}$$

using the creation and annihilation operators $\hat{a}^\dagger$ and $\hat{a}$, respectively, which further define the expectation value of the number of motional quanta via $n = \langle\hat{a}^\dagger\hat{a}\rangle$ [66]. The interaction of a two-level atom with classical monochromatic electromagnetic radiation of frequency ω and phase ϕ is described by the Hamiltonian [54]

$$\hat{H}_\mathrm{I} = \frac{\hbar\Omega_0}{2}(\hat{\sigma}_+ + \hat{\sigma}_-)\left(e^{i(k\hat{x}-\omega t+\phi)} + e^{-i(k\hat{x}-\omega t+\phi)}\right) \tag{2.38}$$

where k is the radiation's wave vector [67], $\hat{\sigma}_\pm = (\hat{\sigma}_\mathrm{X} \pm i\hat{\sigma}_\mathrm{Y})/2$ and Ω_0 is called the Rabi frequency. Using the definition of $\hat{a}^\dagger$ and $\hat{a}$ [66], one can rewrite $k\hat{x} = \eta(\hat{a} + \hat{a}^\dagger)$ where the Lamb-Dicke factor is defined by

$$\eta = k\sqrt{\frac{\hbar}{2m\omega_\mathrm{T}}}. \tag{2.39}$$

The Lamb-Dicke factor relates the recoil energy from photon absorption to the harmonic oscillator's energy spacing [68]. In addition to this substitution, the Hamiltonian in Equation 2.38 is transformed to the interaction picture by [66]

$$\hat{\tilde{H}} = \hat{U}^\dagger\hat{H}_\mathrm{I}\hat{U} \qquad \text{with} \qquad \hat{U} = \exp(-i/\hbar(\hat{H}_\mathrm{A} + \hat{H}_\mathrm{M})t). \tag{2.40}$$

The result contains four terms oscillating at sum and difference frequencies of ω_0 and ω. To simplify the Hamiltonian, two approximations are typically made. First, a rotating wave approximation is applied that neglects fast oscillations at the sum frequency $\omega + \omega_0$ while at the same time defining the detuning $\Delta = \omega - \omega_0$ [44]. Second, terms exponential in η are expanded in a Taylor series where orders starting from $\mathcal{O}(\eta^2)$ are neglected, which is a valid approximation in the Lamb-Dicke regime, defined as $\eta^2(2n+1) \ll 1$ [69]. The condition for the Lamb-Dicke regime is fulfilled if the atom's motional wavepacket is much smaller than the wavelength of the radiation. The result is the interaction Hamiltonian

$$\hat{\tilde{H}} = \frac{\hbar\Omega_0}{2} e^{-i(\Delta t - \phi)} \left(1 + i\eta \left(\hat{a}^\dagger e^{i\omega_T t} + \hat{a} e^{-i\omega_T t}\right)\right) \hat{\sigma}_+ + h.c. \tag{2.41}$$

that couples excitation in the atom's internal levels with its motional quanta in the harmonic trap. Under the approximation $\Omega_0 \ll \omega_T$, three special cases arise for different settings of the detuning Δ in Equation 2.41:

- **Carrier transition** ($\Delta = 0$).
  The motional excitation is not changed by the absorption of a photon, coupling the levels $|g, n\rangle$ and $|e, n\rangle$ with a Rabi frequency Ω_0.

- **Red sideband transition** ($\Delta = -\omega_T$).
  A quanta of motional excitation is removed from the system when absorbing a photon. The levels $|g, n\rangle$ and $|e, n-1\rangle$ are coupled with a Rabi frequency $\Omega_{RSB} = \eta\sqrt{n}\Omega_0$.

- **Blue sideband transition** ($\Delta = +\omega_T$).
  A quanta of motional excitation is added to the system when absorbing a photon. The levels $|g, n\rangle$ and $|e, n+1\rangle$ are coupled with a Rabi frequency $\Omega_{BSB} = \eta\sqrt{n+1}\Omega_0$.

These three cases are visualised in Figure 2.4.

For transition frequencies in the radio frequency regime, the Lamb-Dicke factor (Equation 2.39) becomes very small[2], meaning that sideband transitions can be safely ignored and the atom-field interaction Hamiltonian of Equation 2.41 reduces to

$$\hat{\tilde{H}} = \frac{\hbar\Omega_0}{2}(e^{-i(\Delta t - \phi)}\hat{\sigma}_+ + e^{i(\Delta t - \phi)}\hat{\sigma}_-). \tag{2.42}$$

[2]For a $^{40}Ca^+$ ion in a trap with $\omega_T = 2\pi \cdot 2.0\,\text{MHz}$, interacting with radiation at $\nu = 11.62\,\text{MHz}$, the Lamb-Dicke factor is $\eta = 1.9 \times 10^{-9}$.

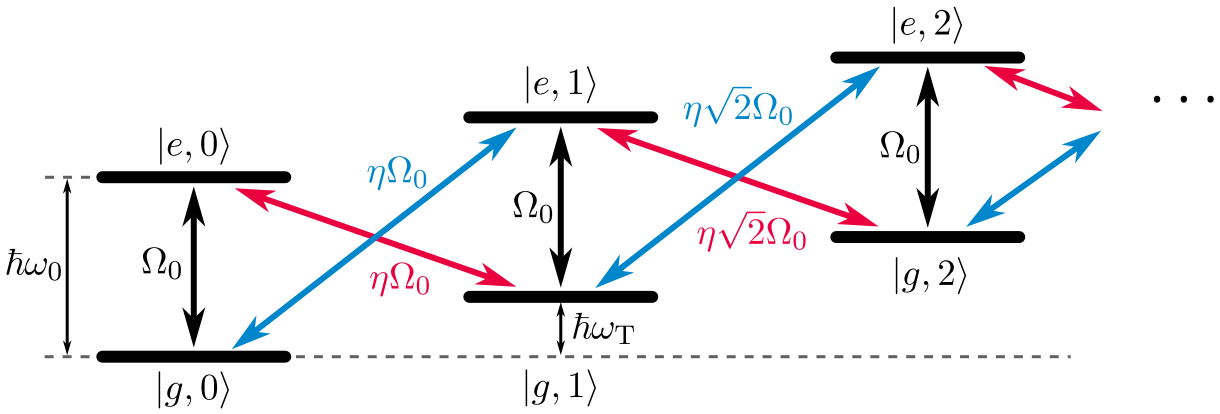

Figure 2.4.: Schematic of internal and external energy levels for a two-level atom, trapped in a one-dimensional harmonic potential. The two-level atom has an energy spacing of $\hbar\omega_0$ between the ground-state $|g\rangle$ and excited state $|e\rangle$. One motional quanta in the harmonic potential has an energy of $\hbar\omega_T$ with the secular frequency ω_T. The combined state of the atom's internal degrees of freedom $|\psi\rangle$ and its quantised motion at n motional quanta is written as a combined ket-vector $|\psi, n\rangle$. The arrows indicating transitions are labelled with their Rabi frequencies and colours indicate transition types and their frequencies: carrier (black), blue sideband (blue) and red sideband (red).

2.3.3. Magnetic dipole transitions

Up to here, the Rabi frequency Ω_0, as a measure for the coupling strength between the drive field and the atomic transition, was introduced without further explanation of the underlying physics, which will be covered now. There are a multitude of electric transitions at optical frequencies used in the experiments of this thesis. Electric dipole transitions are caused by the coupling between the atom's electric dipole moment and an oscillating electric field. For electric quadrupole transitions, the coupling is caused by the atom's electric quadrupole moment being susceptible to the gradient of an oscillating electric field. For more information on electric dipole and quadrupole transitions see [69]. The core of Chapter 5 presents experiments in which a magnetic dipole transition is driven. In the following, the physics of magnetic dipole transitions are discussed.

Magnetic dipole transitions are caused by the interaction of the atom's magnetic dipole moment $\hat{\vec{\mu}}$ with an oscillating magnetic field $\vec{B}(t)$. The magnetic dipole interaction Hamiltonian reads [44]

$$\hat{H}_I = -\hat{\vec{\mu}} \cdot \vec{B}. \tag{2.43}$$

An atom's magnetic dipole moment depends on the atom's internal state, more specifically on its angular momentum, which can have contributions from electron spin, orbital angular momentum and nuclear spin. The magnetic dipole moment is defined as [70]

$$\hat{\vec{\mu}} = g_J \mu_B \hat{\vec{\sigma}} \tag{2.44}$$

where $\hat{\vec{\sigma}} = (\hat{\sigma}_X, \hat{\sigma}_Y, \hat{\sigma}_Z)$ is the Pauli matrix vector, g_J is the Landé g-factor and the Bohr

magneton is $\mu_\mathrm{B} = e\hbar/(2m_\mathrm{e})$ with the elementary charge e, the electron mass m_e and the reduced Planck constant $\hbar$. For a single electron spin, like in the $4^2S_{1/2}$ ground-state of $^{40}Ca^+$, g_J becomes the Landé g-factor of a single electron g_e. Inserting a constant magnetic field of B_0 in the z-direction into the interaction Hamiltonian from Equation 2.43 produces the Zeeman shift in Equation 2.34, yielding a two-level system with basis states $|0\rangle = |4^2S_{1/2,m_J=-1/2}\rangle$ and $|1\rangle = |4^2S_{1/2,m_J=+1/2}\rangle$.

Transitions between two spin states can be driven by an oscillating magnetic field in a direction perpendicular to the quantisation field B_0. With a drive field

$$\vec{B}(t) = B_\mathrm{RF}\cos(\omega t - \phi)\vec{e}_\mathrm{X} \tag{2.45}$$

of strength B_RF in x-direction, oscillating with frequency ω at a phase ϕ, the interaction Hamiltonian 2.43 becomes

$$\hat{H}_\mathrm{I} = -g_J\mu_\mathrm{B}B_\mathrm{RF}\cos(\omega t - \phi)\hat{\sigma}_\mathrm{X}. \tag{2.46}$$

Expressing $\hat{\sigma}_\mathrm{X}$ by the spin raising and lowering operators $\hat{\sigma}_\pm$ and writing the cosine term as a sum of complex exponentials leads to

$$\hat{H}_\mathrm{I} = -\frac{g_J\mu_\mathrm{B}B_\mathrm{RF}}{2}(\hat{\sigma}_+ + \hat{\sigma}_-)\left(e^{i(\omega t-\phi)} + e^{-i(\omega t-\phi)}\right). \tag{2.47}$$

By comparing with Equation 2.38 one finds the expression for the Rabi frequency

$$\Omega_0 = -\frac{g_J\mu_\mathrm{B}B_\mathrm{RF}}{\hbar} = \gamma B_\mathrm{RF} \tag{2.48}$$

with the gyromagnetic ratio γ. The gyromagnetic ratio of a single electron spin is $\gamma_e = 2\pi \cdot 2.802\,\mathrm{MHz\,G^{-1}}$ [71].

2.3.4. Dynamics of a driven two-level atom

The time evolution of a two-level atom's state $|\widetilde{\psi}(t)\rangle$ is given by the Schrödinger equation [44]

$$i\hbar\frac{\mathrm{d}}{\mathrm{d}t}|\widetilde{\psi}(t)\rangle = \hat{\widetilde{H}}|\widetilde{\psi}(t)\rangle \tag{2.49}$$

where the transformed Hamiltonian $\hat{\widetilde{H}}$ from Equation 2.42 contains the interaction between the two-level atom and a drive field in the case of negligible coupling to the atom's motion, e.g. for radio frequency driving. To solve for the time evolution, one splits up the state vector into the basis states $|0\rangle$ and $|1\rangle$ with complex coefficients $c_{0,1}(t)$ as

$$|\widetilde{\psi}(t)\rangle = c_0(t)|0\rangle + c_1(t)|1\rangle. \tag{2.50}$$

The resulting system of differential equations is solved by performing a Laplace transformation [54] with the initial conditions $c_0(0) = \alpha$ and $c_1(0) = \beta$, representing the arbitrary qubit

state from Equation 2.1. Time evolution of the state can be expressed by $|\widetilde{\psi}(t)\rangle = \hat{U}(t)|\widetilde{\psi}_0\rangle$ and the time evolution operator $\hat{U}(t)$ can be written explicitly as [54]

$$\hat{U}(t,\Omega_0,\Delta,\phi) = \begin{pmatrix} e^{-i\frac{\Delta t}{2}}(\cos(\frac{\Omega t}{2}) + i\frac{\Delta}{\Omega}\sin(\frac{\Omega t}{2})) & -\frac{\Omega_0}{\Omega}e^{-i(\frac{\Delta t}{2}+\phi)}\sin(\frac{\Omega t}{2}) \\ \frac{\Omega_0}{\Omega}e^{i(\frac{\Delta t}{2}+\phi)}\sin(\frac{\Omega t}{2}) & e^{i\frac{\Delta t}{2}}(\cos(\frac{\Omega t}{2}) - i\frac{\Delta}{\Omega}\sin(\frac{\Omega t}{2})) \end{pmatrix} \tag{2.51}$$

where $\Omega = \sqrt{\Omega_0^2 + \Delta^2}$ is the effective Rabi frequency. In the case of the initial state being $|0\rangle$, the time evolution of the coefficients $c_{0,1}(t)$ becomes [70]

$$c_0(t) = \cos\left(\frac{\Omega t}{2}\right) - i\frac{\Delta}{\Omega}\sin\left(\frac{\Omega t}{2}\right), \qquad c_1(t) = -i\frac{\Omega_0}{\Omega}\sin\left(\frac{\Omega t}{2}\right). \tag{2.52}$$

The probability to obtain the state $|1\rangle$ as a measurement outcome, henceforth referred to as the *excitation probability*, is then given by

$$p_1(t) = |c_1(t)|^2 = \left(\frac{\Omega_0}{\Omega}\right)^2 \sin^2\left(\frac{\Omega t}{2}\right) \tag{2.53}$$

which is plotted in Figure 2.5 for different settings of the detuning Δ. The excitation probability shows oscillations, also called *Rabi flops*, at the effective Rabi frequency Ω. These Rabi flops fully reach the excited state when the drive field is on resonance ($\Delta = 0$). When increasing the detuning Δ, the amplitude reduces and oscillations become faster.

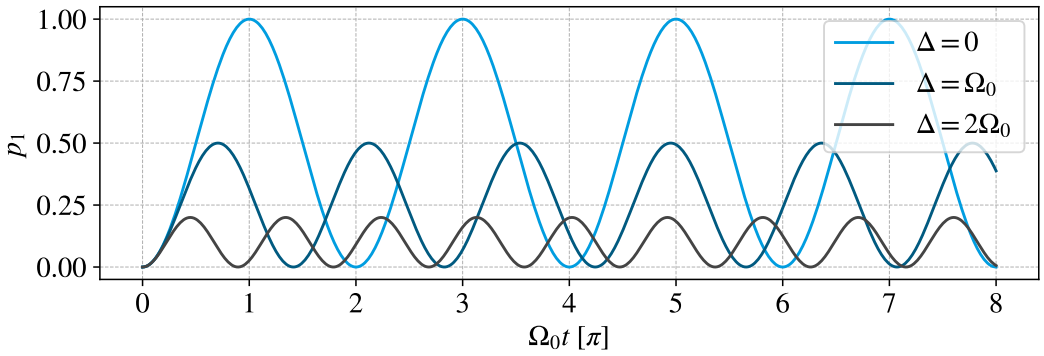

Figure 2.5.: Oscillations of the excitation probability (Equation 2.53) in a driven two-level atom, also called Rabi flops, for three different values of detuning Δ. Detuning is given in units of the Rabi frequency Ω_0 and the horizontal axis represents the duration of driving normalised by the Rabi frequency $\Omega_0 \cdot t$.

On resonance ($\Delta = 0$), Equation 2.51 reduces to a term with the form of the unitary qubit rotation in Equation 2.8. For a qubit encoded in a single electron spin, rotations of the form given by Equation 2.8 can be performed by pulses of an oscillating magnetic field.

2.4. AC electronics

The experimental setups presented in Chapters 4 and 5 rely on electronics that operate with alternating currents (AC). This section introduces the basic concepts necessary for understanding these setups.

2.4.1. RLC circuits

The simplest model of an electronic circuit is based on three classes of passive components: resistors, capacitors and inductors. Those components are characterised by the following equations that relate the voltage U and current I

$$I(t) = R \cdot U(t), \qquad I(t) = C \cdot \frac{\mathrm{d}}{\mathrm{d}t} U(t), \qquad U(t) = L \cdot \frac{\mathrm{d}}{\mathrm{d}t} I(t) \tag{2.54}$$

where R is the ohmic resistance, C the capacitance and L the inductance [72]. Time-varying voltages and currents can be decomposed into individual frequency components by a Fourier transformation [73], allowing the dynamics in a circuit to be studied in frequency space. The following analysis of RLC circuits can therefore be simplified to considering sinusoidal voltages and currents at a single frequency. A sinusoidal voltage with amplitude U_0 at a frequency ω and with phase ϕ is expressed by $U(t) = U_0 \cdot \cos(\omega t + \phi)$. Such a sinusoidal voltage can be rewritten as the real part of a complex number. This complex number is the product of the complex amplitude $\hat{U}(\phi) = U_0 \cdot \exp(i\phi)$ and the oscillating term $\exp(i\omega t)$. The complex amplitude $\hat{U}(\phi)$ contains the amplitude and phase information of the sinusoidal voltage, which is now expressed by [74]

$$U(t) = \mathrm{Re}(\hat{U}(\phi) \cdot e^{i\omega t}). \tag{2.55}$$

The described formalism of treating a sinusoidal signal by the real part of a complex number is applied to both currents and voltages, giving their respective complex amplitudes $\hat{I}$ and $\hat{U}$. In the case of passive components[3], the oscillating terms $e^{i\omega t}$ can be dropped, leaving only the complex amplitudes [75]. When applying the Fourier transformation to Equation 2.54, the derivatives transform to multiplications with $i\omega$. Further, when replacing the time varying voltages and currents in Equation 2.54 by their complex amplitudes, in all three cases, a generalised form of Ohm's law is found: The complex amplitudes of current and voltage, $\hat{I}$ and $\hat{U}$, are related by

$$\hat{U} = Z \cdot \hat{I} \tag{2.56}$$

where Z is called the *impedance*. For the three classes of passive electronic components — resistance R, capacitance C and inductance L — the respective impedances are [74]

$$Z_\mathrm{R} = R, \qquad Z_\mathrm{C}(\omega) = \frac{1}{i\omega C} \qquad \text{and} \qquad Z_\mathrm{L}(\omega) = i\omega L. \tag{2.57}$$

[3]The components need to be described by linear differential equations.

The frequency response of an arbitrary circuit with passive components can be calculated using the Kirchhoff circuit laws [76]. By defining an input voltage $\hat{U}_{\text{in}}$ and output voltage $\hat{U}_{\text{out}}$ in a circuit, the transfer function $G(\omega) = \hat{U}_{\text{out}}/\hat{U}_{\text{in}}$ can be used to characterise the circuit's frequency response. The transfer function can be split up into a real-valued amplitude and a complex exponential phase term [77]

$$G(\omega) = A(\omega) \cdot e^{i\phi(\omega)}. \tag{2.58}$$

Typically, amplitude and phase are plotted together in a Bode diagram, as exemplified in Figure 2.6b.

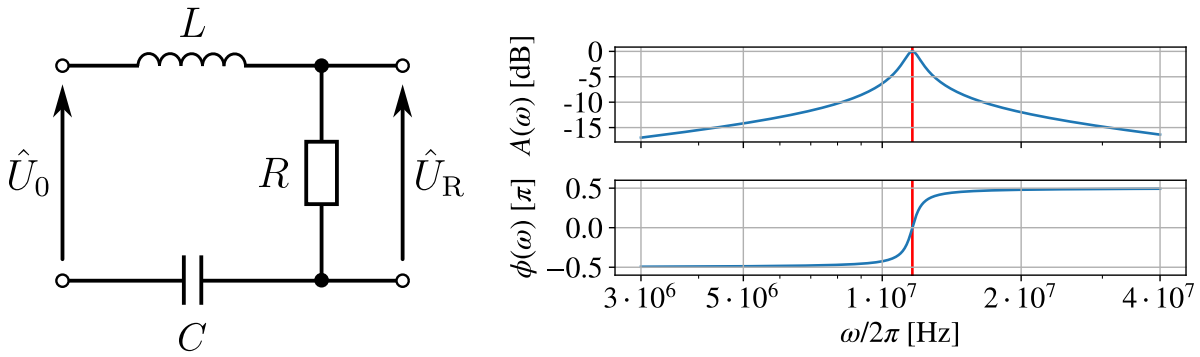

(a) **(b)**

Figure 2.6.: a) Series resonance circuit with resistance R, inductance L and capacitance C. Only a fraction of the input voltage $\hat{U}_0$ is transferred to the output voltage across the resistor $\hat{U}_R$. **b)** Amplitude and phase of the transmission function (Equation 2.59) are plotted in a Bode diagram for $R = 11.1\,\Omega$, $L = 2.1\,\mu\text{H}$, and $C = 89.3\,\text{pF}$ (an RLC circuit with roughly these values is used in the implementation presented in Section 5.1.2). Full amplitude transmission (0 dB) is reached at the resonance frequency (red line) which is $2\pi \cdot 11.62\,\text{MHz}$ for the values of R, L and C in this example.

Using a combination of resistors, inductors and capacitors, particular frequency components in a voltage input signal can be attenuated. As an example, consider the series RLC resonance circuit in Figure 2.6a. The transmission function for that circuit is given by

$$\begin{aligned} G(\omega) = \frac{\hat{U}_R}{\hat{U}_0} &= \frac{R}{R + i(\omega L - \frac{1}{\omega C})} = A(\omega) \cdot e^{i\phi(\omega)} \\ &= \frac{1}{\sqrt{1 + \frac{1}{R^2}(\omega L - \frac{1}{\omega C})^2}} \cdot \exp\left(i \cdot \arctan\left(\frac{\omega L}{R} - \frac{1}{\omega RC}\right)\right). \end{aligned} \tag{2.59}$$

The amplitude $A(\omega)$ maximises for a frequency

$$\omega_0 = \frac{1}{\sqrt{LC}}, \tag{2.60}$$

forming a resonance. On resonance, the impedances from the capacitor and the inductor cancel each other and the current in the series circuit is given by $\hat{I} = \hat{U}_0/R$. The width of the resonance σ is commonly defined as the frequency band where the power is higher than half its maximum, giving $\sigma = R/L$ [78]. For such a resonance, the quality factor is defined by

$$Q = \frac{\omega_0}{\sigma} = \frac{1}{R}\sqrt{\frac{L}{C}} \tag{2.61}$$

as a measure for the ratio between stored and dissipated energy during one oscillation period [74].

When taking the output voltage at the inductor or capacitor, the transmission function's amplitude at resonance frequency is $|G(\omega_0)| = Q$. Therefore, voltages at the capacitor and inductor are amplified by the quality factor Q. Energy is still conserved because at the capacitor and inductor, current and voltage are out of phase by $\pi/2$.

2.4.2. Transmission lines

Heaviside-model

Transmission lines, consisting of a ground and signal wire are used to transmit electronic signals, generated from a voltage *source*, to an electronic circuit, typically called a *load*. The voltage signal is generally represented by an electromagnetic wave and the wavelength λ is related to the frequency ν by the propagation velocity in the wire medium c as

$$\lambda = \frac{c}{\nu}. \tag{2.62}$$

When guiding an electrical signal through a wire, the characteristic physical effects of waves start to become relevant if the wavelength is comparable to the wire length [79]. To account for these effects, the transmission line can be modelled using passive electric components. In the Heaviside-model of a transmission line [80], the line is decomposed into an infinite amount of infinitesimally short two-port segments. These segments can be modelled by two resistors, a capacitor and an inductor, all treated per unit length as shown in Figure 2.7a. The resistance R' represents the ohmic resistance of the wires in the transmission line and the inductance L' accounts for the magnetic field generated around them. Between the two wires of the line, a capacitor C' and a resistor with conductance G' model the dielectric behaviour of the material separating the wires. The values of R', L', C' and G' depend on the exact wire geometry in the transmission line. For the complete transmission line, modelled as an infinitely long chain of the described segments, the *characteristic impedance* Z_0 at a frequency ω is derived by solving the Telegrapher's equations [81], giving [82]

$$Z_0(\omega) = \sqrt{\frac{R' + i\omega L'}{G' + i\omega C'}}. \tag{2.63}$$

The nominator and denominator inside the square root have the units $\Omega\,\mathrm{m}^{-1}$ and $\Omega^{-1}\,\mathrm{m}^{-1}$, respectively. The characteristic impedance Z_0 does therefore not depend on the length of the transmission line.

A chain of transmission lines

When connecting two transmission lines, the voltage signals at their interface have to fulfil the boundary conditions, that the voltages of incoming, transmitted, and reflected waves need to be continuous. Solving the resulting system of equations leads to the expression for the reflection coefficient [83]

$$\Gamma = \frac{Z_2 - Z_1}{Z_2 + Z_1} \tag{2.64}$$

where Z_1 and Z_2 are the characteristic impedances of the incoming and outgoing transmission lines, respectively. The absolute square $|\Gamma|^2$ gives the ratio between reflected signal power and incoming signal power at the interface between two transmission lines. For $Z_1 \neq Z_2$, not all of a wave's energy is transmitted to the subsequent transmission line, but a part of the wave is reflected [84]. A reflected wave will interfere with the incoming wave, producing artefacts like standing waves with up to twice the input voltage amplitude [74]. Reflection is zero for equal characteristic impedances $Z_1 = Z_2$ in both transmission lines. To avoid standing waves causing damage to electric components, and to maximise the power transmitted through a chain of transmission lines, most commercially available AC electronic components have their impedance set to a standardised value of $50\,\Omega$ [85].

Impedance matching

Custom-made parts usually have an impedance deviating from the standardised $50\,\Omega$. In that scenario, impedance matching to the standard impedance in the remaining circuit has to be performed. Impedance matching for a single frequency can be achieved by adding capacitances and inductances around the non-standardised complex load impedance Z_L. For single frequency impedance matching there are different configurations available, forming L-, pi- or T-shaped matching circuits [86]. Impedance matching for a finite bandwidth requires more complex circuits [87]. In the following, single frequency impedance matching for the load being a series RLC resonance circuit (Figure 2.6a) using an L-type matching circuit is discussed. The L-type matching circuit has a capacitance C_IM in series with the load and an inductance L_IM in parallel to both load and C_IM, as shown in Figure 2.7b.

Both C_IM and L_IM can be optimised such that the total impedance of the circuit Z has a real part of $50\,\Omega$ and a vanishing imaginary part. An analytical solution for values of C_IM and L_IM that achieves matching of the total impedance to $Z = Z_0 = 50\,\Omega$ at the RLC circuit's resonance frequency ω_0 was derived in the following steps: First, the network's impedance Z is calculated with the methods of complex RLC circuit analysis (introduced in Section 2.4.1). Then, the conditions $\mathrm{Re}(Z) = \mathrm{Re}(Z_0) = 50\,\Omega$ and $\mathrm{Im}(Z) = \mathrm{Im}(Z_0) = 0$ lead to a system of two equations for the variables C_IM and L_IM. Finally, this system of equations is solved by

$$C_\mathrm{IM} = \left(\omega_0 \cdot Z_\mathrm{L}(\omega_0)\sqrt{\frac{Z_0}{Z_\mathrm{L}(\omega_0)} - 1}\right)^{-1} \quad \text{and} \quad L_\mathrm{IM} = \frac{1}{\omega_0^2 \cdot C_\mathrm{IM}} + C_\mathrm{IM} \cdot Z_\mathrm{L}(\omega_0)^2. \tag{2.65}$$

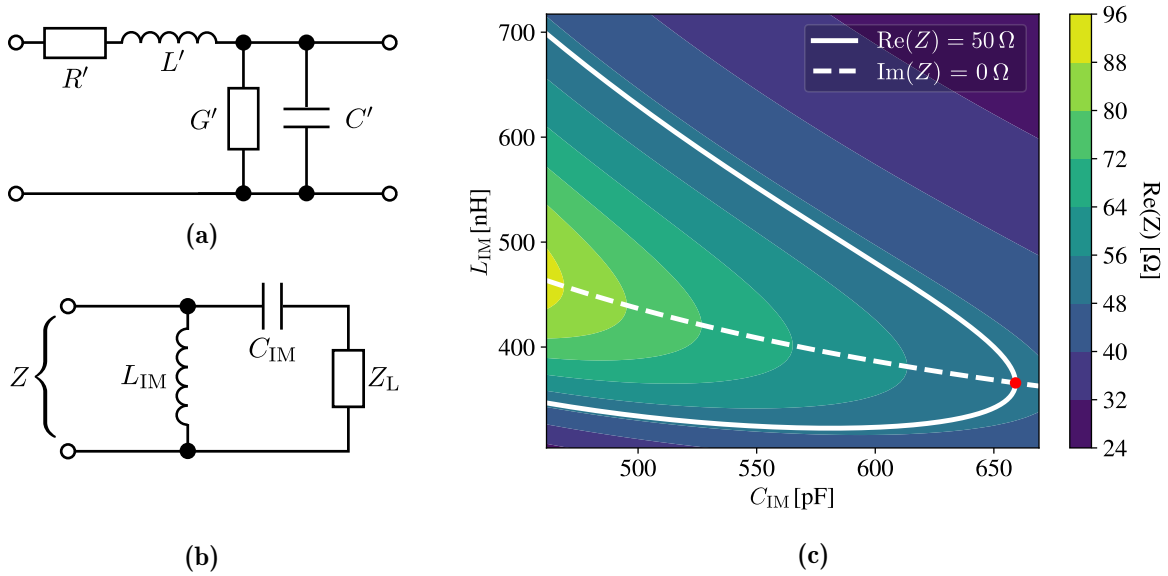

Figure 2.7.: a) Heaviside model of an infinitesimally short transmission line segment. The segment is modelled by passive electric components which are all treated per unit length (indicated by the symbol $'$): wire resistance R', wire inductance L', as well as conductance G' and capacitance C' of the dielectric material which separates the two wires. **b)** Passive L-type impedance matching circuit for a complex load impedance Z_L. The circuit will have a total impedance of Z for specific values of C_IM and L_IM. **c)** Contour plot of the real part of the total impedance Z from the circuit in (b) in dependence of C_IM and L_IM. The load Z_L is represented by a series RLC resonance circuit with $R = 11.1\,\Omega$, $L = 2.1\,\mu\mathrm{H}$ and $C = 89.3\,\mathrm{pF}$, driven at its resonance frequency of $\omega_0 = 2\pi \cdot 11.62\,\mathrm{MHz}$. The total impedance Z is calculated using the methods of complex RLC circuit analysis in Section 2.4.1. The solid white line indicates points where $\mathrm{Re}(Z) = 50\,\Omega$ and the dashed white line indicates points where $\mathrm{Im}(Z) = 0$. Their intersection point (red) marks the capacitance and inductance values that achieve minimum RF reflection at $C_\mathrm{IM} = 659.1\,\mathrm{pF}$ and $L_\mathrm{IM} = 365.8\,\mathrm{nH}$.

Figure 2.7c shows the real part of Z for different values of C_IM and L_IM when preforming impedance matching of a series RLC resonance circuit with $R = 11.1\,\Omega$, $L = 2.1\,\mu\mathrm{H}$ and $C = 89.3\,\mathrm{pF}$[4]. The conditions $\mathrm{Re}(Z) = 50\,\Omega$ and $\mathrm{Im}(Z) = 0$ can be fulfilled individually with multiple combinations of C_IM and L_IM, represented in Figure 2.7c by the white curves. There only exists a single configuration of C_IM and L_IM where both conditions are fulfilled simultaneously. In the given example, impedance matching at the series RLC resonance circuit's resonance frequency of $2\pi \cdot 11.62\,\mathrm{MHz}$ is achieved at $C_\mathrm{IM} = 659.1\,\mathrm{pF}$ and $L_\mathrm{IM} = 365.8\,\mathrm{nH}$.

[4]An RLC circuit with roughly these values is used in the implementation presented in Section 5.1.2

2.4.3. Electromagnetic properties of a current carrying coil

Magnetic field

Electric current passing through a wire produces a magnetic field as described by Ampère's law [88]. For a time independent current, the integral form of Ampère's law reduces to the Biot-Savart law [89]: At a position in space $\vec{r}$, the magnetic field $\vec{B}(\vec{r})$, produced by a current I flowing along the path S, is given by

$$\vec{B}(\vec{r}) = \frac{\mu_0 I}{4\pi} \int_S \mathrm{d}\vec{l}(\vec{r}\,') \times \frac{\vec{r} - \vec{r}\,'}{|\vec{r} - \vec{r}\,'|^3} \tag{2.66}$$

where the path S is parametrised by the vector $\vec{r}\,'$, $\mathrm{d}\vec{l}(\vec{r}\,')$ is an infinitesimally short vector in direction of the current at the position $\vec{r}\,'$ and μ_0 is the vacuum magnetic permeability[5] [90]. A circular wire loop in the xy-plane with radius R, as shown in Figure 2.8, is parametrised in cylindrical coordinates by

$$\vec{r}\,' = \begin{pmatrix} R \cdot \cos(\varphi) \\ R \cdot \sin(\varphi) \\ 0 \end{pmatrix} \quad \text{with} \quad 0 \leq \varphi < 2\pi, \quad \text{giving} \quad \mathrm{d}\vec{l}(\vec{r}\,') = \begin{pmatrix} -R \cdot \sin(\varphi) \\ R \cdot \cos(\varphi) \\ 0 \end{pmatrix} \mathrm{d}\varphi. \tag{2.67}$$

For a coil consisting of N such loops, the integral over each loop is the same and the field contributions from all loops sum up. It is convenient to also express the position $\vec{r}$ in cylindrical coordinates where the angular dependence can be neglected due to the rotational symmetry of the coil, giving $\vec{r} = (r, 0, z)$.

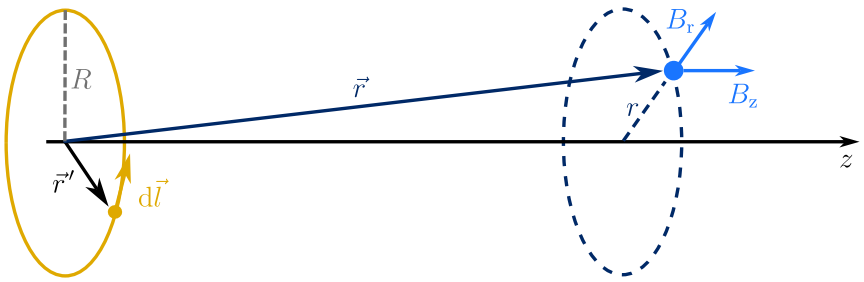

Figure 2.8.: Magnetic field from a circular current loop. The axial and radial magnetic field components at the position $\vec{r}$, $B_z(\vec{r})$ and $B_r(\vec{r})$, respectively, are parametrised by the axial distance z and the radial distance r. The current loop is placed with its centre at the origin ($z = 0$, $r = 0$) and spans the plane perpendicular to the z-axis with a radius R. The loop carries a current I through the infinitesimally short wire segment $\mathrm{d}\vec{l}$, located at $\vec{r}\,'$.

The magnetic field can then be split up into its radial and axial components, B_r and B_z, respectively as

$$\vec{B}(r, z) = B_z \vec{e}_z + B_r \vec{e}_r. \tag{2.68}$$

[5] It is assumed that the current carrying wire is surrounded by a non-magnetic material.

By inserting the parametrisations of $\vec{r}'$, $\mathrm{d}\vec{l}(\vec{r}')$ and $\vec{r}$ into Equation 2.66, one obtains

$$B_{\mathrm{z}}(r,z) = \frac{\mu_0 INR}{4\pi} \int_0^{2\pi} \frac{R - r\cdot\cos(\varphi)}{(r^2+R^2-2rR\cdot\cos(\varphi)+z^2)^{3/2}}\mathrm{d}\varphi \tag{2.69}$$

and

$$B_{\mathrm{r}}(r,z) = \frac{\mu_0 INR}{4\pi} \int_0^{2\pi} \frac{z\cdot\cos(\varphi)}{(r^2+R^2-2rR\cdot\cos(\varphi)+z^2)^{3/2}}\mathrm{d}\varphi. \tag{2.70}$$

The setup in Chapter 5 uses a circular coil as an RF antenna to drive a magnetic dipole transition in a single $^{40}\mathrm{Ca}^+$ ion. The coil is ideally aligned such that the ion is in an on-axis position ($r = 0$). For $r = 0$, analytic solutions exist to Equation 2.69 and 2.70: The magnetic field strength in radial direction becomes $B_{\mathrm{r}}(r = 0) = 0$ and the magnetic field strength in axial direction reduces to [91]

$$B_{\mathrm{z}}(r=0,z) = \frac{\mu_0 INR^2}{2(R^2+z^2)^{3/2}}. \tag{2.71}$$

At the centre position of the coil at $z = 0$, $r = 0$, a field strength of

$$B_0 = |\vec{B}(r=0,z=0)| = \frac{\mu_0 IN}{2R} \tag{2.72}$$

is found. A plot of the field strength in dependence of the axial distance from the coil centre is shown in the upper plot in Figure 2.9a by the black curve. In the axial direction, the axial field strength B_{z} drops off on a length scale comparable to the coil radius R. At distances much larger than the coil radius R, B_{z} scales with the axial distance as z^{-3}.

To estimate how, for the setup in Chapter 5, imperfect alignment of the coil affects the field strength experienced by the ion, the case of an off-axis position ($r \neq 0$) is discussed in the following. For $r \neq 0$, the integrals in Equations 2.69 and 2.70 do not have an analytical solution. Numeric integration gives the result plotted in the Figures 2.9a and 2.9b. The following four qualitative observations are made: First, when reducing the distance to the wire ($z \to 0$, $r \to 0$), the radial field strength B_{r} increases, but jumps to zero at the exact wire position ($z = 0$, $r = R$). Second, the radial field component B_{r} has a maximum at a radial distance r_{max}. For $z \simeq R$, the maximum is at $r_{\mathrm{max}} \approx R$ and with increasing z, the maximum position r_{max} increases. Third, for axial distances $z \gg R$, a radial displacement of $r \ll R$ results in a perturbation to the field strengths B_{r} and B_{z} which is small compared to B_{z}. Fourth, at every point in space, the field strength is proportional to the current I in the wire and the number of coil windings N.

Inductance

For a time-varying current $I(t)$, the magnetic field produced by the coil acts back on the current in the wire due to Lenz's law [88]. The coil then has to be treated as an inductive component when being placed in an electronic circuit. The inductance of a circular wire

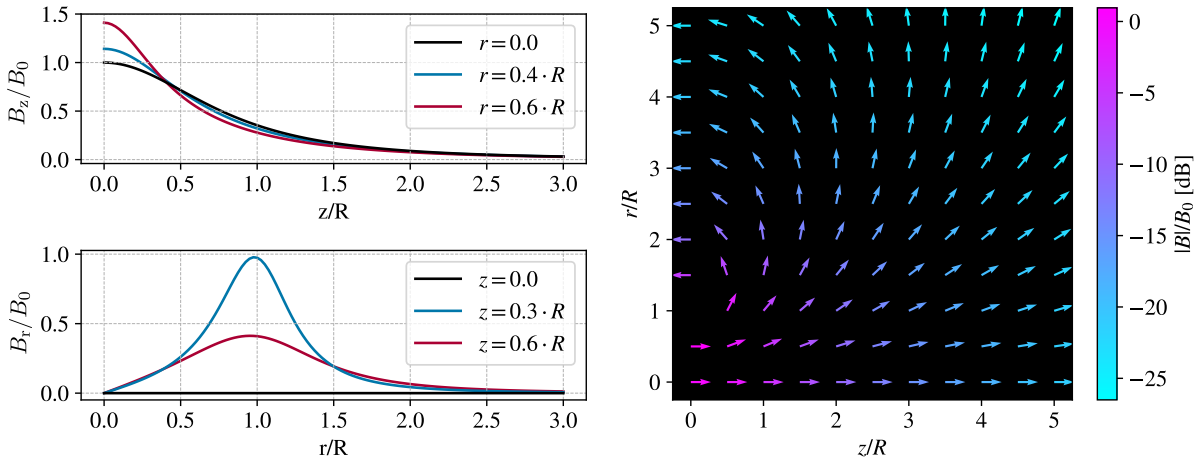

Figure 2.9.: Magnetic field produced by the coil in Figure 2.8. **a)** Field strength in axial and radial direction in dependence of axial distance z and radial distance r. Distances are normalised by the coil radius R. The magnetic field is given in units of the field strength at the centre of the coil B_0. **b)** Vector plot of the magnetic field in the zr-plane. Magnetic field strength is indicated by colors based on a logarithmic scale.

loop can be derived using a curved integral [92] and for constructing a coil out of N such loops, the inductance scales with N^2 [93] as

$$L = \mu_0 N^2 R \cdot \ln\left(\frac{8R}{R_\mathrm{W}} - 2\right) \tag{2.73}$$

where R_W is the wire radius.

2.5. Qubit coherence

Coherence is the property of a wave that allows interference with other waves. For a qubit, coherence describes the qubit's ability to interfere with a resonant drive field. Coherence is required in order to observe a qubit's quantum mechanical properties and is therefore desired for quantum information processing. This section first introduces a method for measuring the coherence of a qubit. Then, an example cause of the loss of coherence (decoherence) is presented. Finally, a method to suppress decoherence is introduced.

2.5.1. The Ramsey experiment

The underlying approach to measure coherence boils down to interferometric techniques [94]. For investigating the interference between an electromagnetic wave and a two-level quantum system, a method has been developed by Norman Ramsey [95], commonly called the *Ramsey experiment*. The electromagnetic wave, called "drive field" in the following, has

a frequency detuned by Δ with respect to the energy splitting of the two-level quantum system, called qubit in the following.

The procedure of the Ramsey experiment is described now, making use of the terminology and mathematics of single qubit rotations that were introduced in Section 2.1. The starting point is the initial state $|0\rangle$. First, a $\pi/2$-pulse, represented by the rotation $\hat{U}_{\mathrm{X,Y}}(\theta = \pi/2, \phi = 0)$ (using Equation 2.8), puts the qubit into the superposition state $|+\rangle$ at the equator of the Bloch-sphere. The phase $\phi = 0$ of this first pulse sets the phase reference for subsequent pulses. During the following free evolution period with duration τ, which is referred to as the *wait time*, qubit and drive field evolve with their individual frequencies[6]. In a frame rotating at the drive field's frequency, the qubit state vector rotates around the z-axis on the Bloch sphere, accumulating a total rotation angle in time τ of $\varphi = \Delta \cdot \tau$. Finally, a $\pi/2$-pulse with phase ϕ, represented by the rotation $\hat{U}_{\mathrm{X,Y}}(\theta = \pi/2, \phi)$, is applied. For no detuning ($\Delta = 0$), the state has not rotated during the wait time and a $\pi/2$-pulse with phase $\phi = \pi$ will rotate the qubit back to the initial state $|0\rangle$. However, for a state that has rotated during the wait time due to detuning, a $\pi/2$-pulse with $\phi = \pi$ in general only partially transfers the qubit back to $|0\rangle$, leaving a non zero probability for the qubit to be in the excited state $|1\rangle$. At the end of the pulse sequence, a projective measurement in the logical basis is carried out. Repeating the experiment many times allows the probability of finding the qubit in the state $|1\rangle$ to be estimated, giving information on the acquired detuning between qubit and drive field. The sequence and state evolution of a Ramsey experiment is shown in Figure 2.10a.

Using the matrix representation of the evolution operator in Equation 2.51, the total evolution is described by

$$|\psi(\tau, \phi)\rangle = \hat{U}\left(\tau_{\mathrm{P}}, \Omega_0, \Delta, \phi\right) \hat{U}(\tau, 0, \Delta, 0) \hat{U}\left(\tau_{\mathrm{P}}, \Omega_0, \Delta, 0\right) |0\rangle \tag{2.74}$$

where Ω_0 is the Rabi frequency, Δ is the detuning between qubit and drive field, τ is the wait time and the $\pi/2$-pulses can have an imperfectly set duration of τ_{P}. In the ideal case of $\pi/2$-pulses, $\tau_{\mathrm{P}} = \pi/(2\Omega)$. The phase of the second pulse ϕ is also called the *analysis phase*. The probability for the final state $|\psi(\tau, \phi)\rangle$ to be the state $|1\rangle$ is given by [69]

$$\begin{aligned} p_1(\tau, \phi) = &\left(\frac{2\Omega_0}{\Omega}\right)^2 \sin^2\left(\frac{\Omega\tau_{\mathrm{P}}}{2}\right) \\ &\cdot \left[\cos\left(\frac{\Omega\tau_{\mathrm{P}}}{2}\right) \cos\left(\frac{\Delta \cdot \tau}{2} + \phi\right) - \frac{\Delta}{\Omega} \sin\left(\frac{\Omega\tau_{\mathrm{P}}}{2}\right) \sin\left(\frac{\Delta \cdot \tau}{2} + \phi\right)\right] \end{aligned} \tag{2.75}$$

where $\Omega = \sqrt{\Omega_0^2 + \Delta^2}$ is the effective Rabi frequency. Typically one deals with small detunings $\Delta \ll \Omega_0$ and perfect $\pi/2$-pulses with durations $\tau_{\mathrm{P}} = \pi/(2\Omega_0)$ which are short in comparison to the wait time $\tau_{\mathrm{P}} \ll \tau$. With these approximations, the excitation probability

[6] The separate evolution of the qubit's phase and the drive field's phase is conceptually similar to separated phase evolution in the two arms of a Mach-Zehnder interferometer.

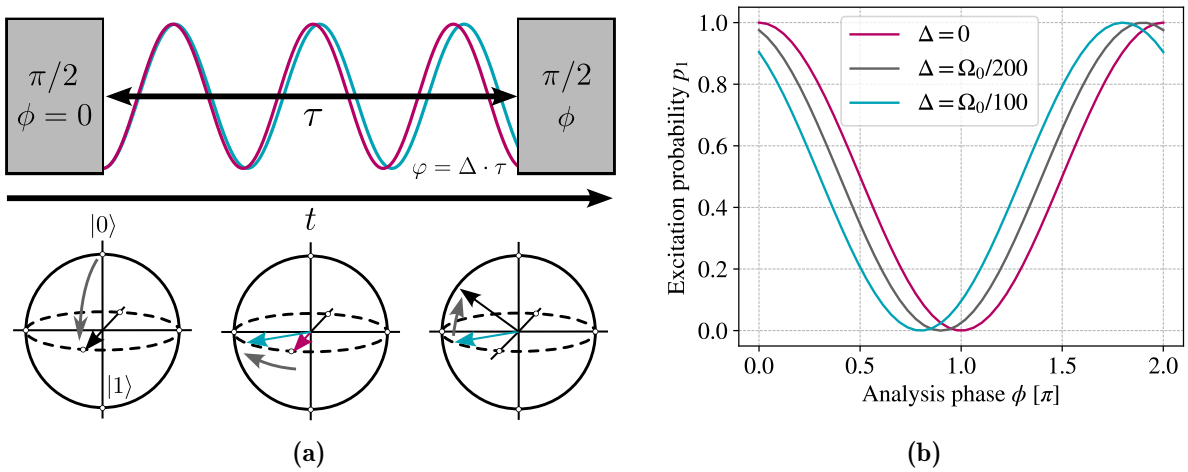

Figure 2.10.: a) Conceptual schematic of a Ramsey experiment with a single qubit initialised in the state $|0\rangle$. The Bloch spheres show the state evolution in a frame rotating at the drive field's frequency. The red oscillating line corresponds to the oscillation of the drive field and the blue oscillating line to the detuned oscillation of the qubit. Any detuning between the two oscillators Δ results in an accumulated phase difference $\varphi = \Delta \cdot \tau$, which presents itself as a rotated state (blue vector) compared to the case with no detuning (red vector). **b)** Plot of the excitation probability of the qubit to be in the state $|1\rangle$ after the Ramsey experiment in dependence of the second $\pi/2$-pulse's phase ϕ (analysis phase). The excitation probability is given by Equation 2.76 with $\Omega_0 = 2\pi \cdot 5\,\mathrm{kHz}$, $\tau_\mathrm{P} = 50\,\mu\mathrm{s}$ and $\tau = 2\,\mathrm{ms}$. Any detuning Δ accumulated during the wait time τ will shift these fringes along the horizontal axis.

in Equation 2.75 reduces to

$$p_1(\tau, \phi) = \cos^2\left(\frac{\Delta \cdot \tau + \phi}{2}\right), \tag{2.76}$$

producing fringes as a function of both the detuning Δ and the analysis phase ϕ, which are exemplified in Figure 2.10b. For no detuning ($\Delta = 0$), an analysis phase of $\phi = 0$ gives full excitation as the second $\pi/2$-pulse completes the other half rotation to the pole opposite to the initial state on the Bloch sphere. Positive detuning shifts the fringes in the negative direction on the horizontal axis. For small detuning $\Delta \ll \phi/\tau$, phases of $\phi = \pi/2$ and $\phi = 3\pi/2$ correspond to an excitation probability of $p_1 \approx 0.5$ and the steepest slope of the fringes is reached, giving the maximum sensitivity to detuning. Ramsey experiments are useful for a precise measurement of frequency differences between a qubit and its drive field. Extending Ramsey experiments by an active feedback loop that keeps the drive field on resonance with the qubit is the foundation for many atomic clocks [96].

The more interesting parameter for the experiments in this thesis is the amplitude of the Ramsey fringes which is a measure for the coherence remaining in the combined system of qubit and drive field after the wait time τ. More information on why the amplitude of Ramsey fringes becomes less than unity in an experimental scenario when increasing τ is given in Section 2.5.2. Coherence is represented by the contrast C of the Ramsey fringes

defined by [94]

$$C = \frac{\max(p_1) - \min(p_1)}{\max(p_1) + \min(p_1)} \tag{2.77}$$

with values between $C = 0$ (no coherence) and $C = 1$ (full coherence). Including the contrast into the fringe function from Equation 2.76 gives

$$p_1(\phi, \varphi) = \frac{1}{2}(1 + C \cdot \cos(\phi + \varphi)) \tag{2.78}$$

where $\varphi = \Delta \cdot \tau$ is the phase shift from detuning.

2.5.2. Noise influence

The contrast of a Ramsey experiment was introduced as a measure for coherence without motivating why it might not have full amplitude. In a real experiment, detuning is not constant and a trapped-ion qubit additionally couples to surrounding electromagnetic fields including the vacuum modes [97]. Such uncontrolled interaction of a qubit with its environment reduces the contrast for increasing wait times τ. All such effects are usually grouped under the term *decoherence*. For the mathematical treatment of a qubit experiencing environmental noise and a differentiation between the different types of decoherence, I refer to [40]. In the following, the influence of fluctuating detuning during Ramsey experiments is considered.

Fluctuating detuning Δ is modelled by a distribution of detunings based on a probability density function $P(\Delta)$. In a Ramsey experiment with wait time τ, fluctuating detuning according to $P(\Delta)$ translates to fluctuating qubit phases $\varphi = \Delta \cdot \tau$. The contrast of Ramsey fringes after the wait time τ is defined as the expectation value of the complex exponential of the randomly distributed qubit phases[7]. This expectation value is calculated by integrating over the product of the complex exponential phase of the qubit $\exp(i\varphi) = \exp(i\Delta\tau)$ and the probability distribution of the fluctuating detuning $P(\Delta)$ [99]

$$C(\tau) = |\langle e^{i\phi} \rangle| = \left| \int_{-\infty}^{\infty} P(\Delta) e^{i\Delta\tau} \mathrm{d}\Delta \right|. \tag{2.79}$$

For a Gaussian distribution [100]

$$P(\Delta) = \frac{1}{\sigma\sqrt{2\pi}} e^{-\frac{\Delta^2}{2\sigma^2}} \tag{2.80}$$

with standard deviation σ, Equation 2.79 reduces to

$$C(\tau) = e^{-\sigma^2\tau^2/2}, \tag{2.81}$$

[7] The expectation value can be understood as calculating the average from multiple repetitions of Ramsey experiments, as done when carrying out Ramsey experiments in the laboratory [98].

showing Gaussian-shaped decay of the contrast with increasing wait time τ. For such a Gaussian-shaped decay, the decay time is typically defined by the time for reaching the $1/e$ fraction of the initial contrast as $\tau_{1/e} = \sqrt{2}/\sigma$. For a Lorentzian distribution [101]

$$P(\Delta) = \frac{1}{\pi\gamma(1 + (\frac{\Delta}{\gamma})^2)} \tag{2.82}$$

with half-width-half-maximum γ, the contrast decays exponentially as

$$C(\tau) = e^{-\gamma\tau}. \tag{2.83}$$

Here, the decay time is again typically defined as the time for reaching a $1/e$ reduction of the contrast as $\tau_{1/e} = 1/\gamma$.

A reduction of contrast can be conceptually understood as averaging over multiple repetitions of the same Ramsey experiment, but each with a different outcome of the qubit's phase. Averaging over multiple pure states of the qubit with different phases results in a mixed state [98] which, on the Bloch sphere, has a vector with less than unit length. For any analysis phase of the Ramsey experiment, the mixed state's projection onto the corresponding axis in the equatorial plane is less than unity, reducing the amplitude of Ramsey fringes and therefore the contrast.

2.5.3. Dynamical decoupling

A loss of qubit coherence constitutes a big problem for quantum information processing. For completely decayed coherence, the qubit is represented by a fully mixed state. On the Bloch sphere, the state vector then has a length of zero, showing the complete loss of the information that was stored in the quantum state. It is desirable to perform quantum information processing significantly faster than the timescale over which relevant decoherence occurs [32]. As the speed of quantum gates is typically limited by the achievable interaction strengths, a goal is to extend the qubit's coherence time. A common way to suppress fluctuations in experimental parameters, like the detuning, is to control them by active feedback loops. The achievable stability with feedback loops that are implemented by electronic circuits is limited by fundamental noise sources [102, 103].

An alternative way to fight decoherence is a method called *dynamical decoupling* [45]. Coming back to the Ramsey experiment, consider the effect of a π-pulse with phase $\phi_{\mathrm{SE}} = 0$ inserted into the middle of the wait time, which is also called a *spin echo*. The qubit starts its free evolution in the state $|+\rangle$, produced by the Ramsey experiment's first $\pi/2$-pulse. At non zero detuning Δ, the qubit's state vector rotates around the Bloch sphere equator by an angle $\varphi = \Delta \cdot \tau/2$ during the first half of the wait time $\tau/2$. The spin echo inverts the qubit's phase evolution [104], leaving the qubit on the Bloch sphere equator at an angle $-\varphi$. In the remaining second half of the wait time, the qubit state again rotates due to detuning. If the detuning stays constant through the total wait time τ, the rotation angle is again φ. In that case, the qubit rotates perfectly back to the initial superposition state

$|+\rangle$. Like in Section 2.5.1, the Ramsey experiment is completed by a second $\pi/2$-pulse with phase ϕ followed by a projective measurement and fringes in excitation probability are obtained when scanning the phase ϕ. The sequence of a Ramsey experiment with a spin echo and the corresponding state evolution is illustrated in Figure 2.11.

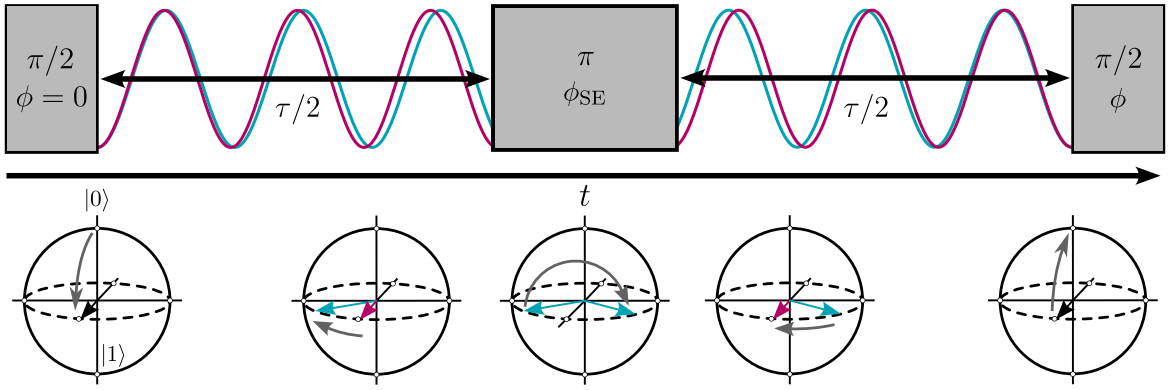

Figure 2.11.: Pulse sequence of a spin echo experiment, which extends the Ramsey experiment sequence from Figure 2.10a by a π-pulse in the middle of the wait time τ. The red line corresponds to the oscillation of the drive field and the blue line to the detuned oscillation of the qubit. In a rotating frame with respect to the drive field, detuning acquired through the first half of the wait time rotates the qubit state on the Bloch sphere equator (blue vector). The spin echo pulse performs a phase flip around an axis that is specified by its phase ϕ_{SE}. By performing the phase flip around an axis parallel to the originally prepared superposition state, the state vector is moved to a point where, with respect to the initial superposition, it is rotated by the same amount but in the opposite direction. If the detuning is the same during the second half of the wait time, the state rotates back to its initial position (red vector) and the final analysis $\pi/2$-pulse perfectly maps the qubit back to the initial state for $\phi = \pi$.

As the spin echo compensates qubit rotations from detuning during the wait time, Ramsey fringes ideally do not show a phase shift. For detuning fluctuations which occur over timescales longer than the wait time, no loss of coherence occurs. With multiple spin echos, decoherence from detuning fluctuations on timescales longer than the time gap between spin echos can be cancelled. When increasing the number of spin echos while keeping the wait time constant, the time gap in between individual spin echos reduces and detuning fluctuations on timescales shorter than the wait time do not lead to a loss of coherence. By reducing the time gap in between spin echos, the influence of detuning fluctuations is reduced in a wider frequency band, consequently reducing decoherence effects further.

Spin echo pulses which have imperfect rotation angles and frequencies cause unwanted rotations of the qubit. The influence of such pulse errors can be minimised by adjusting the phases ϕ_{SE} of the spin echo pulses such that the spin echos correct themselves. The work in this thesis uses the most simple form for compensating errors in rotation angle and detuning, which is the XY-4 sequence [105]. In the XY-4 sequence, spin echos are

performed in an alternating way around the x- and y-axis of the Bloch sphere by setting the phase of the i-th spin echo pulse by

$$\phi_{\mathrm{SE},i} = \begin{cases} 0, & i \text{ even} \\ \pi/2, & i \text{ odd} \end{cases} . \tag{2.84}$$

For constant pulse imperfections in rotation angle and frequency (e.g. due to a miscalibration), the combined rotation from four XY-4 spin echos in a row has a close to unity fidelity with the identity operation. If pulse errors are not constant during one cycle of four XY-4 spin echos, further rotations are introduced, leading to a deviating from the identity operation. More advanced decoupling schemes that increase the robustness to dynamic pulse imperfections use composite pulses [106]. The method used in more recent publications involving quantum memories [107, 108, 109] is Knill dynamical decoupling [110]. There is still ongoing development for universally-robust sequences with respect to pulse shape and improved scaling in the pulse number for higher orders of pulse error compensation [111]. A deeper discussion on different pulse sequences for dynamical decoupling and a comparison of their performance from both simulation and experiments can be found in [112].

3. Pre-existing quantum network node based on $^{40}Ca^{+}$

The work presented in this thesis extends functionalities of a quantum network node which was developed in the *Distributed Quantum Systems* group [113]. For information on the original quantum network node, that existed before I began my master's thesis and that was used to obtain the measurement results in Chapters 4 and 5 of this thesis, I refer the reader to the theses of Josef Schupp [114], Martin Meraner [115] and Vojtěch Krčmarský [116]. This chapter introduces key parts of the pre-existing quantum network node setup and summarises established techniques for trapped-ion quantum information experiments that are routinely implemented in our laboratory.

3.1. Experimental setup

Our quantum network node consists of a string of $^{40}Ca^{+}$ ions that are held in a linear Paul trap and positioned at the focus of an optical cavity. Trap and cavity are enclosed into a vacuum chamber with optical viewports and electronic feedthroughs. A photograph of the vacuum chamber with surrounding parts is shown in Figure 3.1. The setup was previously located at the Institute for Quantum Optics and Quantum Information (IQOQI) but got moved over to the University (UIBK) building in fall 2021 [117]. At the point of starting my master's project, the experiment had just been set up again and basic functionality had been recovered.

Ion trap

The experiment uses a 3D *blade* linear Paul trap, designed by Stefan Haslwanter at the IQOQI mechanical workshop and based on previous trap devices in the *Quantum Optics & Spectroscopy* group at the University of Innsbruck. The trap is mounted to a flange at the top of the vacuum chamber which also includes electronic feedthroughs for the trap's drive signals. Trap electrodes made of gold-coated titanium are mounted on sapphire holders, which offer near room temperature operation [118]. Two opposing *endcap* DC trap electrodes, aligned in the axial direction that ideally aligns with the ion-string axis, are designed to be spaced by 5.0 mm [116]. Their voltages are set individually by a high voltage

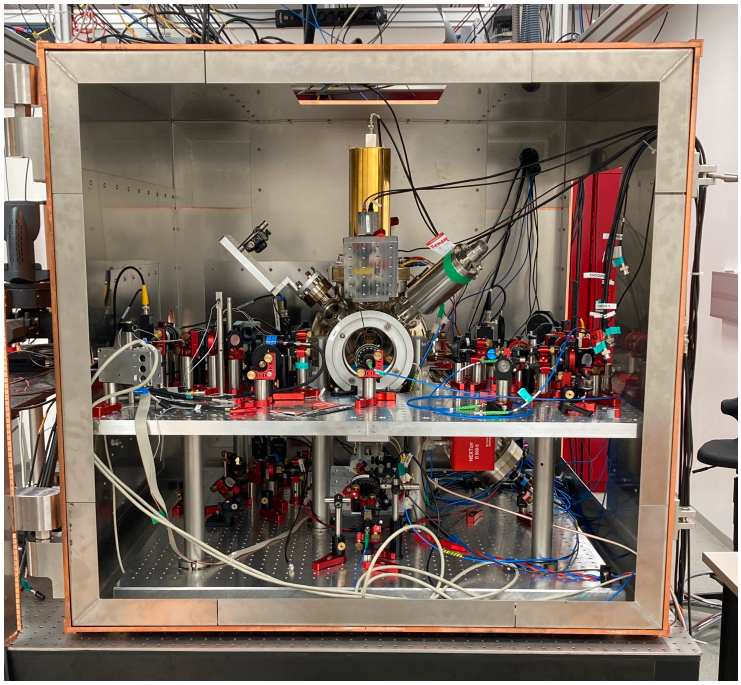

Figure 3.1.: Photograph of the main part of the experimental setup which is a vacuum chamber inside a magnetic shielding. The door and other openings of the shielding are usually closed during experiments. The photograph was taken on 01.09.2022 in the UIBK laboratory (Viktor-Franz Hess building, 1st floor, room 1/33).

power supply[1]. For all experiments in this thesis that use a single ion, the endcap's voltages were set to 1100 V and 1115 V. Trap electrodes in the radial plane, called *blades*, are divided into two pairs of cross-diagonal electrodes and the ion-blade separation is designed to be 0.8 mm [116]. The first blade pair's potential is kept close to electrical ground at a DC voltage of 1.5 V, the other pair has an AC voltage applied, oscillating at a radio frequency. More details on the blade's drive circuit are given in Section 4.1. Additional electrodes (two rods each in two perpendicular planes) are used to compensate stray electric fields. The voltages of the additional electrodes are significantly lower compared to voltages at the endcaps and blades. With the correct compensation voltages applied, ions in the trap will sit at the centre of the RF quadrupole potential where micromotion vanishes [65]. A photograph of the trap is shown in Figure 3.2a.

Vacuum chamber and geometry

The stainless steel vacuum chamber is made for ultra-high vacuum pressures on the order of 10^{-9} mbar and lower. Such pressures are reached by a combination of an ion- and getter pump[2]. Full details on the assembly process can be found in the upcoming PhD thesis of Vojtěch Krčmarský [116]. The geometry of the chamber is shown in Figure 3.2b.

[1] ISEG box EHS 82 20x-F
[2] NexTORR D500 and CapaciTORR Z400

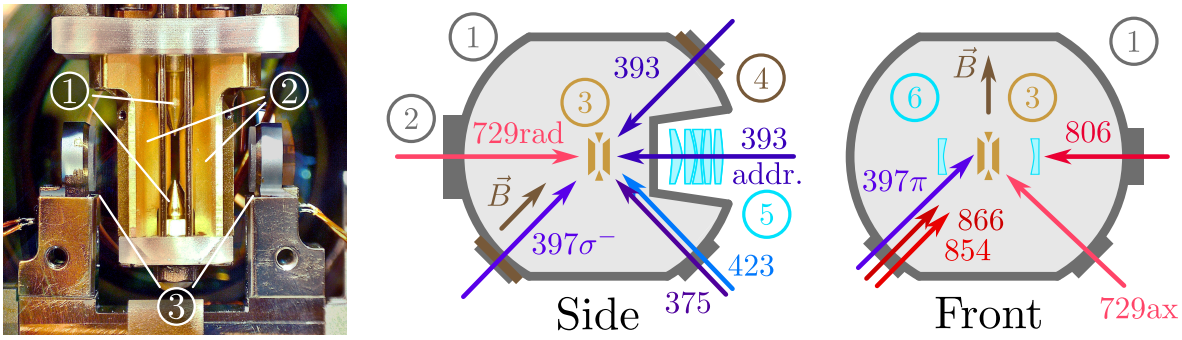

(a) (b)

Figure 3.2.: a) Photograph of the ion trap and Fabry-Pérot cavity inside the vacuum chamber taken from the PhD thesis of Josef Schupp [114]: endcap electrodes (1), two of the in total four blade electrodes (2) and cavity mirrors (3). **b)** Geometry schematic of the vacuum chamber (1), shown both from the front and the side. The chamber features a CF100 viewport at the front (2). The ion trap (3) is mounted in the middle of the chamber and optical access for laser fields is given from several sides, indicated by the red, blue and violet arrows. Wavelengths are indicated by numbers, given in nanometers. Greek letters indicate polarisation and suffixes label beam directions with respect to the trap axes as well as addressed beams. A static magnetic field $\vec{B}$ (brown arrow) is generated by rings of permanent magnets (4). Ion fluorescence at 397 nm is collected through an objective (5), inserted into an inverted viewport at the back of the chamber. A Fabry-Pérot cavity (6) surrounds the ion trap close to perpendicular to the trap's axial direction. The cavity can couple out photons at 854 nm and is length stabilised using laser light at 806 nm.

Optical access to the centre region of the trap is provided by glass viewports. Apart from one smaller viewport, they are all anti-reflection coated for all wavelengths present in the experiment. The back of the vacuum chamber features an inverted viewport reaching close to the ion trap. An objective is inserted there for collecting fluorescence of ions at 397 nm. More details on the objective and the fluorescence detection path are presented below.

Rings of permanent magnets[3] are attached around two opposite viewports at the lower front and upper back of the chamber (shown by brown segments in the side view of Figure 3.2b). The permanent magnets produce a magnetic field with a strength of 4.148(2) G at the centre of the trap. At this field strength, the Zeeman levels in $^{40}Ca^+$ split up by $2\pi \cdot 11.62\,\text{MHz}$ in the $4^2S_{1/2}$ ground-state and by $2\pi \cdot 6.97\,\text{MHz}$ in the $3^2D_{5/2}$ excited state. To suppress fluctuations in the frequencies of the Zeeman splittings, ambient magnetic fields are attenuated by a mu-metal shield[4] that surrounds the vacuum chamber. The shield features a door and other openings that give access to the surrounding parts of the vacuum chamber. During experiments all openings of the shield are usually kept closed. A comparison of measured magnetic field fluctuations with opened and closed shield door can be found in Appendix B.3.

[3] Samarium cobalt with low temperature coefficient: LTC(YXG-22)
[4] Magnetic Shields UK, custom design

Laser light at 729 nm reaches the ion trap by beams coming from two different directions, labelled as 729ax and 729rad in Figure 3.2b. The 729rad beam enters through a CF100 viewport at the front of the chamber and enables coupling to the ion's motion in the radial trap plane. The 729ax beam comes from the bottom right side of the chamber such that the k-vector of its light has a component in the axial trap direction, allowing coupling to the ion's axial motion. Two beams at 397 nm supply light with π- and σ^--polarisation. The π-beam has projections onto all three trap axes and is used for Doppler cooling. The σ^--beam is aligned parallel to the magnetic field and is used for optical pumping. Light at 393 nm comes from two different beams, one parallel to the magnetic field, the other one enters through the objective at the back of the vacuum chamber and can be steered by an acousto-optical deflector (AOD) to address individual ions [119]. Light at 375 nm, 423 nm, 866 nm, 854 nm and 806 nm comes by single beams from the directions indicated in Figure 3.2b.

Ion-photon interface

Although not used in the work of this thesis, the ion-photon interface is a crucial part of the quantum network node. The interface is implemented by a macroscopic Fabry-Pérot cavity, mounted to the bottom-flange of the vacuum chamber via translation stages. The cavity axis is titled by an angle of 85.3(1)° with respect to an ion string in the axial trap direction [120]. The mirror separation is 20 mm and the cavity is operated in the near-concentric regime, yielding a microscopic waist in the cavity centre. Mirrors are glued onto piezo stages which allow active stabilisation of the cavity length. The length stabilisation is performed using laser light at 806 nm, which in turn is frequency stabilised to an external reference cavity. The finesse of the in-vacuum cavity at 854 nm was measured to be $F = 54(1) \cdot 10^4$ during the cavity assembly process [114]. In October 2022 a lower value of $29.8(6) \cdot 10^4$ was found after an incident in which too much current was put through the in-vacuum atomic oven. To either side of the cavity, lenses are placed, serving the purpose of mode matching the locking laser light and collimating the cavity's output mode.

The 393 nm laser is used to drive a cavity-mediated Raman transition (CMRT) [121], causing an ion to emit a single photon into the cavity mode at 854 nm. By driving the CMRT, a photon exiting the cavity has been obtained with a success probability of 72(3)% [114]. The photon's polarisation state can be entangled with the electronic state of an ion. Photons coming out of the cavity are guided through a single-mode optical fibre. Further, these photons can be converted to the Telecom C-band while preserving their polarisation state with high fidelity [115]. The converted photon's absorption probability is then minimised when sending the photon through a subsequent optical fibre. The subsequent fibre can therefore be significantly longer than laboratory length scales. Photons coming out of the fibre are detected by superconducting nanowire single photon detectors[5] (SNSPD). Alternatively, the fibre output can be sent to a Hong-Ou-Mandel interferometer

[5] Scontel FCOPRS-CCR-2TW75+2SW85

connecting to the second node in the Innsbruck quantum network [36] by a beam splitter. Both outputs of the beam splitter are then connected to the SNSPDs.

Imaging system

Fluorescence photons from the ions at 397 nm are collected through a five-lens objective at a distance of $d = 58$ mm to the centre of the ion trap. All numbers in this paragraph are taken from the master's thesis of Marco Canteri [119]. At the distance d, the numerical aperture is 0.289 which results in a maximum photon collection efficiency of 2.5% out of the solid angle 4π. The objective has its focus at a distance of 1.5 m where an electron multiplying CCD camera (EMCCD), as well as a photomultiplier tube (PMT) are placed at the outputs of a 50:50 beam splitter. Stray light is reduced by a band-pass filter and a slit aperture.

Laser systems

Laser light for manipulating the electronic state of trapped ions is generated by commercially available laser systems based on Titanium-Sapphire- and external-cavity diode lasers. Additional lasers are used for ionisation of neutral calcium atoms and length-stabilisation of the in-vacuum cavity. Table 3.1 lists the laser wavelengths, models and their use in the experiment.

Table 3.1.: List of the experiment's laser systems.

Wavelength [nm]	**Model**	**Use**
397	Toptica TA-SHG Pro	Imaging, Doppler cooling, optical pumping.
729	M^2 SolsTiS SA PSX-R	Qubit manipulation, sideband cooling.
866	Toptica DL-Pro	Repumping from $3^2D_{3/2}$.
854	Toptica DL-Pro	Repumping from $3^2D_{5/2}$.
393	M^2 SolsTiS 1600 PSX-R with ECD-X doubling stage	Single photon generation.
423	Toptica DL-Pro	First stage ionisation.
375	Toptica iBeam smart	Second stage ionisation.
806	Toptica DL-Pro	Length stabilisation of the in-vacuum cavity.

All lasers operate in continuous wave (CW) mode and individual pulses are generated by acousto-optical modulators (AOM). The AOMs also allow for imprinting a frequency shift or phase change on the laser light based on the AOM's input RF signal [122]. Laser beams for photoionisation are blocked and unblocked by motorised mechanical shutters. More

information on the beam paths and light preparation can be found in the PhD thesis of Josef Schupp [114]. The 729 nm laser shares an optical table with the vacuum chamber and an external reference cavity. All other laser systems are mounted on a separate optical table. The external reference cavity is used to frequency stabilise the lasers at 393 nm, 806 nm and 729 nm. For the 729 nm laser, a linewidth on the single-Hertz level was achieved, as reported in the master's thesis of Armin Winkler [117]. The reference cavity's mirror spacer is made out of ultra-low expansion glass (ULE) [123] and mounted inside a small vacuum chamber which in turn is placed inside a wooden box for acoustic isolation. Details on the reference cavity can be found in the master's thesis of Helene Hainzer [124]. Laser wavelengths are monitored using a wavemeter[6]. By optical fibres the light is guided to the viewports of the vacuum chamber, but also to other experiments in neighbouring laboratories.

Experiment control

The whole experimental system is controlled from three computers, connected via Ethernet, as shown in Figure 3.3. The first one, called the *laser PC*, is used for communicating with digital controllers of the diode lasers and the wavemeter. Second, the *camera PC*, is used for communicating with the EMCCD camera and for controlling the high voltage power supply of the trap's DC signals. The third PC is the central part for controlling experiments using trapped ions and is called the *control PC*.

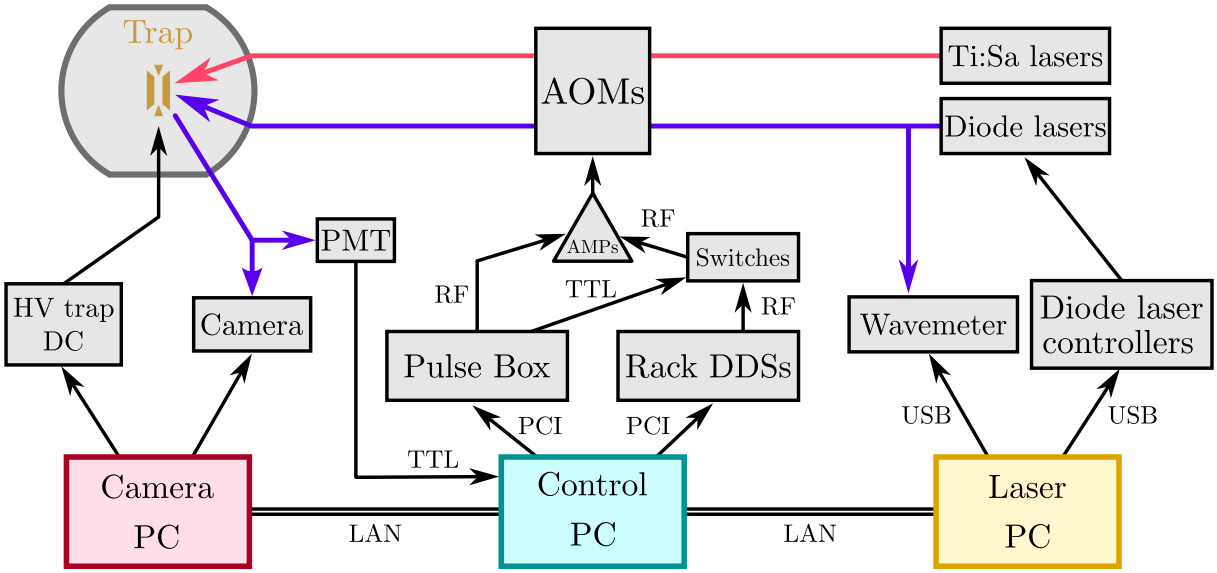

Figure 3.3.: Schematic of the experimental control system that is divided into three PCs for diode laser, camera + trap, and experimental sequence control. Laser pulses going to ions in the trap are generated through acousto-optical modulators (AOMs), driven by amplified RF signals. These signals are generated from two electronic control devices: an FPGA-based pulse sequencer (Pulse Box, see main text) and a rack with free running DDS devices.

[6] HighFinesse WSU-10

The control PC runs an in-house developed software, called *TrICS*, that allows laser pulse sequences to be generated and measurement data from the PMT or the single photon detectors to be saved. On the hardware side, the control PC is connected with two electronic control units via PCI interfaces. The first of these two control units is a bus system, featuring free running direct digital synthesis (DDS) [74] units. These DDSs are mounted inside a rack next to RF amplifiers[7] and their signal amplitudes and frequencies are set by TrICS. The second electronic control unit is a field-programmable gate array (FPGA) based pulse sequencer, also called the *Pulse Box*[8]. The Pulse Box features TTL outputs as well as phase-stable DDS units.

Radio frequency signals from DDS sources are amplified and used to drive AOMs in the paths of laser beams. The amplitude of an AOM's RF signal controls the laser light's intensity. The frequency of an AOM's RF signal controls the laser light's frequency where tuning is possible in the range of tens of megahertz. Pulses are generated either by internal switches at the DDSs in the Pulse Box or by external RF switches, controlled by a TTL signal from the Pulse Box.

Experimental sequences are written in Python, where pulses are defined as objects. Pulse parameters are represented as variables that are accessible from TrICS. For experiments, a sequence compiled from the Python file is executed multiple times after being uploaded to the memory of the Pulse Box. It is possible to change pulse variables over several repetitions of a sequence, producing *scans*. If no variable from the sequence is scanned, the same sequence is repeated, which for the remaining part of this thesis is referred to as a *dummy scan*.

The execution of experimental sequences can be phase-synchronised with the 50 Hz power line cycle by a system called the *line-trigger*. By line-triggering, the dynamic magnetic field produced by power lines is the same for each repetition of a sequence. It follows that the qubit's state at the end of the sequence is not a statistical mixture out of different phases of the power line cycle. The influence of 50 Hz and its higher harmonic noise components on the ion qubit's coherence is therefore reduced. As line-triggering slows down the execution of experimental sequences, it is usually turned off for measurements.

The PMT communicates with the control PC via TTL signals. After state readout of ions, PMT count numbers are written to a CSV file together with time stamps and the values of the scanned pulse variable. Further, for every experimental run, a file containing all parameter settings is saved.

Another PC is used for logging data of laser light intensities, laboratory temperature and humidity, as well as RF power at the AC trap drive. The logging data is saved in a database powered by InfluxDB and can be accessed by a Grafana user interface, offering plots of time traces and data export options. More details on the used communication protocols and the exact devices can be found in in the PhD thesis of Josef Schupp [114].

[7] Designed by Gerhard Hendl at IQOQI Innsbruck.
[8] Developed by Paul Pham and Philipp Schindler [125].

3.2. Established techniques

During the last three decades of ion trapping experiments, several methods have been developed which are now used extensively in basically every trapped-ion quantum information experiment. Here I give a brief overview of the basic techniques that were applied in the experiments presented in Chapters 4 and 5. These techniques include those for performing laser cooling, optical pumping, and state detection.

3.2.1. Initialisation and readout

Loading ions into the trap

Before running experimental sequences, ions have to be loaded into the trap. Neutral calcium atoms are emitted from a resistively-heated metal tube that is mounted below the trap, also called the atomic *oven*. A metal shield around the oven, with an aperture pointing towards the trap, reduces heat radiation and deposition of atoms onto surrounding vacuum parts, especially onto the cavity [116]. Calcium atoms entering the central region of the trap can undergo a photoionisation process driven by laser light. Ionisation is performed in two steps using laser wavelengths of 423 nm and 375 nm to select the desired isotope. An ionised calcium atom reacts to the electric potential of the trap and stays confined. In our system, ions typically remain trapped for several hours or even more than a full day. All experiments reported in Chapters 4 and 5 use only a single ion.

Doppler cooling

Trapped ions originating from the oven have a broad velocity distribution which prevents resolving motional sideband transitions. Quantum information experiments require an ion to be in the Lamb-Dicke regime (introduced in Section 2.3.2), which can be reached by Doppler cooling [54] with laser light. Three-dimensional confinement of an ion in the trap with different oscillation frequencies in all directions of trap axes allows for Doppler cooling using a single laser beam that has a projection onto all three axes of the trap.

To implement Doppler cooling in our system, we use the 397 nm transition from $4^2S_{1/2}$ to $4^2P_{1/2}$ which, given its scattering rate of $\Gamma = 2\pi \cdot 22.4\,\mathrm{MHz}$, has a Doppler limit of $T_\mathrm{D} = \Gamma/(2k_\mathrm{B}) = 0.5\,\mathrm{mK}$ [65] where k_B is the Boltzmann-constant. In the experiment, only the π-polarised 397 nm beam indicated in Figure 3.2b is used for Doppler cooling. While in 93.6% of the cases an ion in the excited state $4^2P_{1/2}$ will decay down to the $4^2S_{1/2}$ ground-state, there is also a 6.4% chance that decay to $3^2D_{3/2}$ happens [126]. An ion being in one of the long-lived D-states cannot absorb photons from the 397 nm cooling laser. To keep the ion in the cooling cycle, repumping on the $3^2D_{3/2}$ to $4^2P_{1/2}$ transition at 866 nm is performed. There is also a repumping laser running at 854 nm to account for unwanted populations in $3^2D_{5/2}$ from previous experimental runs. In our setup, phonon number expectation values of 11(2) in the axial motional mode and 8(2) in the radial motional

modes of a single ion are typically achieved after a few milliseconds of Doppler cooling [114] for mode frequencies of $2\pi \cdot 0.9\,\mathrm{MHz}$ and $2\pi \cdot 2.4\,\mathrm{MHz}$, respectively.

Optical pumping

After Doppler cooling, the ion's electronic state is prepared in $4^2S_{1/2,m=-1/2}$ by optical pumping using the σ^--polarised 397 nm beam. Light with such polarisation can transfer population only from the $4^2S_{1/2,m=+1/2}$ ground-state towards the $4^2P_{1/2}$ manifold while the $4^2S_{1/2,m=-1/2}$ state remains ideally untouched. Decay from $4^2P_{1/2}$ to both ground-state Zeeman levels is possible, causing electron population to accumulate in $4^2S_{1/2,m=-1/2}$. During optical pumping, repumping is performed using the 866 nm and 854 nm lasers. In our setup, performing optical pumping for tens of microseconds results in the ion being in $4^2S_{1/2,m=-1/2}$ with over 99% probability [116].

Sideband cooling

For experiments that involve driving motional sideband transitions, the ion is also prepared into the ground-state of the relevant motional mode using resolved sideband cooling [54]. Our sideband cooling process operates on the $4^2S_{1/2}$ to $3^2D_{5/2}$ electric quadrupole transition at 729 nm. When driving the transition's red motional sideband, the ion gets excited to the $3^2D_{5/2}$ manifold while at the same time removing a quanta of its motion in the harmonic trap potential. The $3^2D_{5/2}$ state is subsequently pumped out via the $4^2P_{1/2}$ state using lasers at 854 nm and 866 nm. During this process, decay from $4^2P_{3/2}$ and $4^2P_{1/2}$ to $4^2S_{1/2}$ happens mainly on the carrier transition when being in the Lamb-Dicke regime [54]. After sideband cooling, the $4^2S_{1/2,m=+1/2}$ state can be populated again. Such population is transferred to $4^2S_{1/2,m=-1/2}$ by repeating optical pumping with the 397 nm σ^--beam.

Imaging and state detection

Ions are imaged by detecting their fluorescence, generated from driving the $4^2S_{1/2}$ to $4^2P_{1/2}$ transition with the 397 nm laser. The $4^2P_{1/2}$ state has a lifetime of 7.1 ns [60] and decays back to the $4^2S_{1/2}$ ground-state in 93.6% of the cases [126], emitting a photon at 397 nm into a random direction. In all other cases, decay leads to the metastable $3^2D_{3/2}$ state which puts the ion in an unwanted dark state. To include the $3^2D_{3/2}$ state into the imaging cycle, repumping at 866 nm is applied at the same time as the 397 nm beam. In contrast to the $4^2S_{1/2}$ state, an ion in the $3^2D_{5/2}$ state will not generate fluorescence at 397 nm, making the states $4^2S_{1/2}$ and $3^2D_{5/2}$ distinguishable by the amount of detected fluorescence. This method of state detection is called *electron shelving* [54] and is illustrated in Figure 3.4a.

Over many excitation and decay cycles, some of the fluorescence photons from electron shelving exit through the objective into the imaging path towards the EMCCD camera and the PMT. With the camera, an image is produced that allows the position and fluorescence state of individual ions to be resolved. For a single ion, measuring the amount of fluorescence

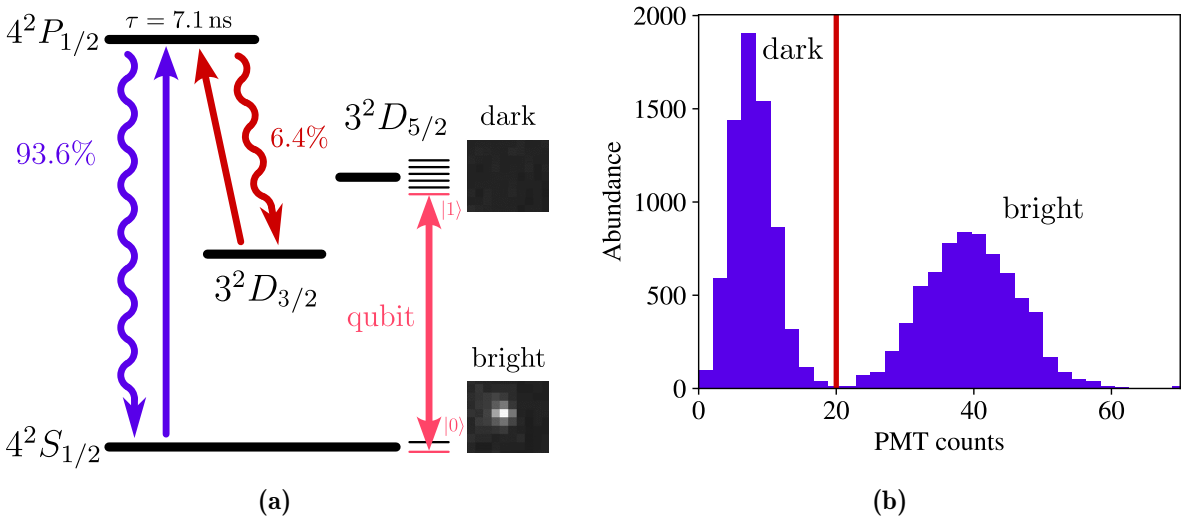

Figure 3.4.: a) Level structure for electron shelving. By driving the $4^2S_{1/2}$ to $4^2P_{1/2}$ transition, fluorescence photons at 397 nm are emitted if the ion was initially in the electronic ground-state $4^2S_{1/2}$ (*bright*). An ion initially in the $3^2D_{5/2}$ excited state cannot get excited to the $4^2P_{1/2}$ state and no 397 nm fluorescence is detected (*dark*). Leakage from the imaging cycle due to spontaneous decay from $4^2P_{1/2}$ to $3^2D_{3/2}$ with a branching ratio of 6.4% is avoided by repumping on the corresponding transition. Insets show camera images of the collected fluorescence from a single ion which, prior to electron shelving, was in the corresponding state. Logical basis states of a qubit encoded into Zeeman levels, one each in $4^2S_{1/2}$ and $3^2D_{5/2}$, are associated with a *bright* and *dark* fluorescence signal, respectively. **b)** The histogram of PMT counts from an ion in a superposition state between $4^2S_{1/2}$ and $3^2D_{5/2}$ shows two peaks corresponding to *bright* and *dark* PMT signal, respectively. The peaks are separated by setting a threshold (red line), such that a measured number of counts is assigned to be either bright or dark.

with the PMT is sufficient in order to distinguish the states $4^2S_{1/2}$ and $3^2D_{5/2}$ by associating them with a *bright* and *dark* PMT signal, respectively. In experiments where a qubit is encoded into Zeeman levels, one each in $4^2S_{1/2}$ and $3^2D_{5/2}$, a *dark* PMT signal is associated with the qubit being found in the chosen Zeeman level in the $3^2D_{5/2}$ manifold, representing the logical state $|1\rangle$. *Bright* PMT signal is then associated with the qubit's logical state $|0\rangle$, represented by the chosen Zeeman level of the $4^2S_{1/2}$ manifold.

Photons collected by the PMT are counted during the time of electron shelving. The duration of electron shelving is typically set to a few milliseconds such that in total a few tens of counts are found for a single ion in the $4^2S_{1/2}$ manifold. Decay from $3^2D_{5/2}$ to $4^2S_{1/2}$ is negligible during that time. Repeated experiments (initialisation and imaging) with an ion in a superposition state between the $4^2S_{1/2}$ and $3^2D_{5/2}$ manifolds result a PMT count histogram showing two peaks, as exemplified in Figure 3.4b. The first peak, closer to no counts, corresponds to no fluorescence in cases where the ion was projected to the dark $3^2D_{5/2}$ state. Nonzero count numbers in this region come from background counts of 397 nm laser light that is scattered inside the vacuum chamber. The second peak at a

higher number of PMT counts corresponds to cases where the ion was projected into the bright $4^2S_{1/2}$ ground-state. By setting a PMT count threshold n_{th}, a measured number of counts n is then assigned to either be a bright or dark PMT signal. In the case of a qubit encoded in Zeeman levels, one each in $4^2S_{1/2}$ and $3^2D_{5/2}$, the measured number of PMT counts n is then associated with one of the qubit's logical basis states:

$$|\psi\rangle = \begin{cases} |0\rangle \sim \text{bright}, & n \geq n_{\mathrm{th}} \\ |1\rangle \sim \text{dark}, & n < n_{\mathrm{th}} \end{cases} \tag{3.1}$$

Detecting the ion in one of these two states implements a projective measurement in the logical basis. A negligible overlap of both peaks in the histogram like in Figure 3.4b allows for state detection with high fidelity [127]. In the laboratory we refer to the excitation probability, which is the probability of finding the ion in the $3^2D_{5/2}$ manifold. Over N repetitions (*cycles*) of the whole experimental sequence, including state preparation, qubit manipulation and projective measurement, the ion is found N_{bright} times in the $4^2S_{1/2}$ manifold and $N_{\mathrm{dark}} = N - N_{\mathrm{bright}}$ times in the $3^2D_{5/2}$ manifold. The excitation probability is then estimated by

$$p = \frac{N_{\mathrm{dark}}}{N}. \tag{3.2}$$

An uncertainty in the excitation probability p comes from the underlying binomial statistics and presents itself as *quantum projection noise* [128] with the standard deviation

$$\Delta p = \sqrt{\frac{p(1-p)}{N}}. \tag{3.3}$$

For probability values of $p = 0$ and $p = 1$ the projection noise vanishes, although these probability values are only estimates based on a limited number of samples N. The approach that we use to define a nonzero error of the excitation probability is to set the error by the maximum out of projection noise and Laplace's rule of succession[9] as [129, 130]

$$\Delta p_{\mathrm{exp}} = \max\left(\Delta p, 1 - \frac{N+1}{N+2}\right). \tag{3.4}$$

One cycle, consisting of initialisation, qubit manipulation and subsequent readout, usually takes on the order of 10 to 20 ms. A typical number of cycles used in our experiments is $N = 50$. Recording a single data point of an excitation probability therefore takes on the order of a second.

[9] The rule of succession gives the probability for finding a dark (bright) PMT signal in the $N + 1^{\mathrm{st}}$ cycle after all previous N cycles showed a bright (dark) PMT signal as measurement outcome.

3.2.2. Spectroscopy and Rabi oscillations

The experiments presented in Chapters 4 and 5 make use of two basic methods which will be introduced briefly in this section. Both methods rely on driving one of the ion's transitions with a single pulse before measuring the excitation probability with the electron shelving method from the previous section. A more detailed description of both methods can be found in [131]. With the experiment's control system, introduced in Section 3.1, parameters of the driving pulse can be varied. The results are scans that show variations in the excitation probability in dependence of the varied pulse parameter.

For *spectroscopy* the frequency of the driving pulse is scanned. The pulse's length is fixed at a duration where, on resonance with the transition, the excitation probability has damped to a value of $p = 0.5$. For far off-resonant frequencies, the excitation probability approaches $p = 0$. The frequency scan therefore maps out the spectrum of the driven transition.

To make coherent dynamics of an ion qubit visible, the duration of the pulse is scanned while keeping its frequency fixed, typically on resonance with the driven transition. The resulting excitation probability shows Rabi oscillations (*flops*) as presented in Figure 2.5.

By fitting the excitation probability data from scans, useful quantities can be extracted. In the case of spectroscopy, centre frequencies and widths of resonance peaks can be determined. For Rabi flops, the Rabi frequency or π-time, amplitude and timescale of damping can be extracted.

3.2.3. Clock operation

Measurements in the following two chapters typically consist of several scans, each taking several seconds or even longer. Usually, the full data taking process spans several hours. During these times, the frequency of the $4^2S_{1/2}$ to $3^2D_{5/2}$ transition (with a chosen pair of Zeeman levels) and the driving 729 nm laser frequency can easily drift apart such that their interaction becomes off resonant. A frequency shift of the laser is typically caused by a drift of the reference cavity's mirror separation. A shift of the atomic transition frequency can have several origins. The model used in the context of this thesis only takes the linear Zeeman shift into account, translating drifts of the ambient magnetic field to the transition frequency. There is no active stabilisation of magnetic fields implemented and locking the 729 nm laser to the reference cavity only provides stability on short timescales comparable to individual scans [117]. Long time laser frequency drifts are reduced by referencing the laser frequency directly to a narrow linewidth atomic transition as done for atomic clocks [96]. In the experiment, we directly reference the 729 nm laser frequency to the $4^2S_{1/2}$ to $3^2D_{5/2}$ electric quadrupole transition.

Frequency drifts of the laser and the atomic transition are determined individually with in total four Ramsey experiments. In the following, the terminology for Ramsey experiments as introduced in Section 2.5.1 is used. First, two Ramsey experiments with analysis phases

$\phi_1 = \pi/2$ and $\phi_2 = 3\pi/2$ are carried out, giving the maximum slope of the Ramsey fringes for $\Delta = 0$ according to Equation 2.78. The excitation probabilities resulting out of these Ramsey experiments p_{ϕ_1} and p_{ϕ_2} are used to calculate the detuning Δ between the probed transition and the laser by [69]

$$\Delta = \left(\tau + \frac{4\tau_\mathrm{P}}{\pi}\right)^{-1} \arcsin\left(\frac{p_{\phi_2} - p_{\phi_1}}{p_{\phi_1} + p_{\phi_2}}\right) \tag{3.5}$$

where τ is the Ramsey experiment's wait time and τ_P is the length of the Ramsey experiment's $\pi/2$-pulses. In order to distinguish the two origins of detuning (laser and linear Zeeman shift), the two Ramsey experiments with analysis phases ϕ_1 and ϕ_2 are repeated using two $4^2S_{1/2}$ to $3^2D_{5/2}$ transitions with different Zeeman levels [132], referred to as the transitions T1 and T2 in the following. Only the laser's contribution to the total detuning will stay the same for both transitions. In our experiment, transition T1 is between the Zeeman levels $m_{S,\mathrm{T1}} = -1/2$ and $m_{D,\mathrm{T1}} = -5/2$, transition T2 is between the Zeeman levels $m_{S,\mathrm{T2}} = -1/2$ and $m_{D,\mathrm{T2}} = -3/2$, and the indices S and D denote the corresponding state manifolds ($4^2S_{1/2}$ and $3^2D_{5/2}$, respectively). For these two transitions, detunings Δ_T1 and Δ_T2 are calculated by Equation 3.5. During the four Ramsey experiments, it is expected that there is no uncontrolled drift in the laser frequency happening, meaning that all changes in frequency for driving the transitions T1 and T2 are well controlled by the frequency offset coming from an AOM. In the following, it is therefore sufficient to represent laser frequencies only by these AOM frequencies $\nu_{\mathrm{T1,\ drive}}$ and $\nu_{\mathrm{T2,\ drive}}$, which are known experimental parameters. With the four Ramsey-experiments, the AOM frequencies $\nu_{\mathrm{T1,\ drive}}$ and $\nu_{\mathrm{T2,\ drive}}$ are found to be detuned by Δ_T1 and Δ_T2, respectively, in comparison to the AOM frequencies for driving the corresponding Zeeman transitions resonantly. The AOM frequencies on resonance with the probed Zeeman transitions ν_T1 and ν_T2 are then calculated by

$$\nu_{\mathrm{T}i} = \nu_{\mathrm{T}i,\mathrm{drive}} - \Delta_{\mathrm{T}i}. \tag{3.6}$$

From the difference between both laser frequencies on resonance with the transitions, equal to the difference of the AOM frequencies $\nu_\mathrm{T1} - \nu_\mathrm{T2}$, the magnetic field B is calculated via

$$B = \frac{\nu_\mathrm{T1} - \nu_\mathrm{T2}}{\mu_\mathrm{B}/h \cdot (g_S(m_{S,,T1} - m_{S,\mathrm{T2}}) - g_D(m_{D,\mathrm{T1}} - m_{D,\mathrm{T2}}))} \tag{3.7}$$

where μ_B is the Bohr magneton, h is the Planck constant and $g_{S,D}$ are the Landé g-factors for the $4^2S_{1/2}$ and $3^2D_{5/2}$ state, respectively[10]. The AOM frequency for a hypothetical transition at vanishing Zeeman shift is given by

$$\nu_0 = \nu_\mathrm{T1} - \mu_\mathrm{B}/h \cdot (g_S m_{S,\mathrm{T1}} - g_D m_{D,\mathrm{T1}}) \cdot B. \tag{3.8}$$

The AOM frequency ν_0 represents the laser's contribution to the detuning, which is the same for both Δ_T1 and Δ_T2.

[10] $g_{S1/2} = -2.002$ and $g_{D5/2} = -1.200$

Running the sequence of four Ramsey experiments and performing the calculations of B (Equation 3.7) and ν_0 (Equation 3.8) is automated by a Python script and from here on referred to as *clock operation*. The script produces logged output with time stamps, the excitation probabilities measured in the Ramsey experiments, the calculated detunings as well as the calculated magnetic field B and AOM frequency ν_0. Further, the script performs linear fits on data of the magnetic field B and the AOM frequency ν_0 from the last 20 min[11]. The fits are used to extract a best guess of the magnetic field B and the AOM frequency ν_0 at the current time stamp. The extracted values of B and ν_0 are sent back to the control software (TrICS) where they are used to calculate the correct AOM frequencies for driving an $4^2S_{1/2}$ to $3^2D_{5/2}$ transition between arbitrary Zeeman levels resonantly. The laser is therefore kept on resonance with the chosen qubit transition during long sessions of data taking. Clock operation spanning several hours showed laser frequency drifts on the order of a few 100 Hz h^{-1}. The magnetic field showed drifts of 1.04(2) µG min^{-1} with the door of the mu-metal shield closed. Plotted data of the magnetic field for both cases of the shield door being open and closed can be found in Appendix B.3.

[11]Weights in the fit decrease exponentially with a time constant of 20 min.

4. Stabilisation of the ion trap's radial mode frequencies

In Section 2.3.2, the coupling between laser light and the motional modes of a trapped atomic ion was introduced. In a trapped-ion quantum processor this coupling is the foundation for entangling gates [30]. The ion's motion in both the axial trap direction and the radial trap plane can be used but it is convenient to start by using the axial modes since their frequencies are typically more stable. When increasing the number of ions, the axial confinement is typically lowered to maintain a linear ion string configuration. Lower axial motional frequencies translate to slower entangling gates and further reduce the gate fidelity due to increased heating rates. The radial modes can remain at high frequencies and are therefore suitable for fast high-fidelity entangling gates. The radial mode frequencies are not intrinsically stable at the same level as the axial mode frequencies and in order to enable coherent motional driving, the radial mode frequencies need to be stabilised.

As a starting point for stabilising the radial motional mode frequencies, consider the relevant parameters in Equation 2.33 which are the blade-ion distance r_0, the frequency of the RF drive signal Ω and the peak voltage at the blades V_{RF}. When comparing fluctuations of these three parameters in a typical experimental setup, it turns out that the dominant contribution to instability comes from the blade-voltage [133]. The blade voltage is directly related to the drive signal power, which is easily affected by temperature changes in the electronics. In this chapter, the process of stabilising the radial motional modes in our ion trap by feeding back to the drive signal power is presented.

This chapter is structured as follows: Section 4.1 introduces the technical framework, consisting of the trap's RF drive circuit and the stabilisation unit. Section 4.2 then presents experiments that assess the performance of the stabilisation system. These experiments are a calibration of the radial motional frequencies (Section 4.2.1), a measurement of deviations in those frequencies during one hour (Section 4.2.2), determining the coherence time of a motional superposition state on the radial blue sideband (Section 4.2.3) and an investigation into the stabilisation system's limitations (Section 4.2.4).

4.1. Drive circuit for the radial trap electrodes

The main parts of the ion trap's radio frequency drive circuit are shown in Figure 4.1. The radial trap electrodes (*blades*) together with connecting wires have a capacitance of

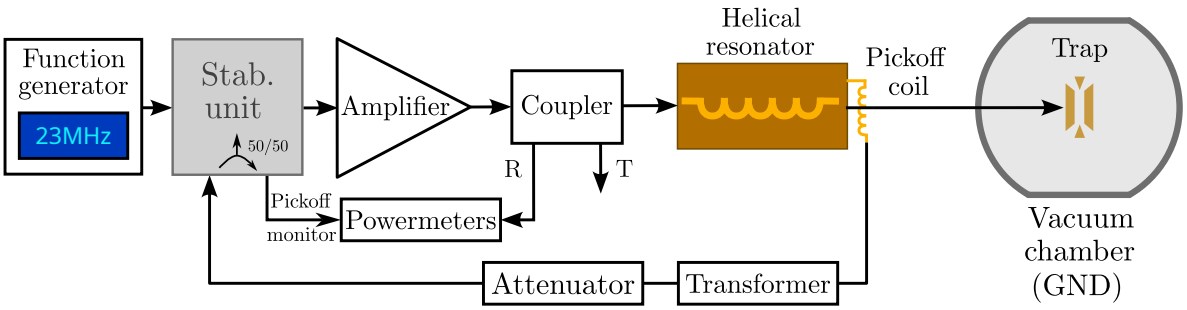

Figure 4.1.: Schematic of the radio frequency drive circuit for the ion trap. The make and model numbers of various components are presented in the main text. The drive signal at around 23 MHz is produced by a function generator, then controlled by a power-stabilisation unit (see Section 4.1.2 for more information) before being amplified. A bi-directional coupler ensures that reflected signals from the trap will not enter the amplifier and provides *pickoff* signals in transmission (T) and reflection (R). The reflection pickoff power is logged by a powermeter. The final part of the drive circuit is a radio frequency resonator, formed by the trap electrodes and a helical resonator (more details in Section 4.1.1). The helical resonator provides a pickoff signal that is used for feedback to the stabilisation unit. The pickoff signal is sent through a 1:1 transformer, to avoid a ground-loop, and an attenuator to match the required pickoff input power of the stabilisation unit. Only half of the pickoff signal is used by the stabilisation unit, the other half is sent to a powermeter for logging.

approximately 12 pF [116]. To match the trap's impedance to standardised 50 Ω components in the preceding parts of drive circuit, an inductive component in the form of a helical resonator is used. Trap and helical resonator together form a resonance circuit with a centre frequency of approximately 23 MHz. A sinusoidal signal at the resonator's centre frequency is produced by a function generator[1], which has its frequency referenced to a GPS-locked 10 MHz source. Radial mode frequencies on the order of a few megahertz require blade voltages of around 1 kV at our trap. For reaching such high voltages, an amplifier with a gain of 43 dB is used[2]. Between this amplifier and the resonance circuit, a bi-directional coupler[3] is placed. The bi-directional coupler fulfils two purposes: First, it prevents reflected signals from the resonance circuit to enter the amplifier in reverse direction which would otherwise damage the amplifier. Second, the bi-directional coupler features pickoff outputs that take off 1% in power from both signal directions. The pickoff signal from the reverse direction is fed to a powermeter[4] for monitoring.

In order to stabilise the signal power, and as a consequence the radial mode frequencies, a feedback loop is implemented. The core part is a stabilisation unit, placed in between the function generator and the amplifier. The stabilisation unit requires an input signal proportional to the blade voltage amplitude. That signal is picked off at the helical resonator.

[1] Rohde & Schwarz SMC100A
[2] Mini-Circuits LZY-22+
[3] Mini-Circuits ZFBDC20-61HP-S+
[4] Mini-Circuits PWR-SEN-4GHS

Only half of the pickoff signal is used by the stabilisation unit. The rest is used as a pickoff monitor output which is sent to another powermeter. Both powermeters are connected to the camera PC (introduced in Section 3.1) by USB and allow logging of the signal powers of reflection- and resonator pickoff. The resolution of the powermeters is specified to be at least 0.01 dB according to the manufacturer [134]. We interpret this resolution as an error bar of ± 0.002 times the measured power value when comparing two power values. More details on the stabilisation unit are given in Section 4.1.2. The next section discusses the details of the helical resonator and pickoff signal generation.

4.1.1. Helical resonator

To ensure impedance matching of the trap and to further amplify the blade voltages, a helical resonator is placed in the drive circuit between the bi-directional coupler and the trap. Structure and geometry of the helical resonator are shown in Figure 4.2.

The helical resonator mainly consists of a coil with an inductance of $L = 1.9\,\mu\text{H}$, calculated with the formula given in [135] and the geometry measures from Figure 4.2. The geometry of the coil and its housing introduce capacitances which influence the transfer function of the resonance circuit consisting of the trap and the helical resonator. A full discussion of a helical resonator's circuit model can be found in [135]. Our helical resonator was designed by Vojtěch Krčmarský [116]. The coil is mounted inside a cylindrical shield and both are made of copper and are coated with gold. The whole configuration is mounted onto an aluminum baseplate which in turn sits on top of a feedthrough to the vacuum chamber. The vacuum chamber is held at electrical ground. The RF input signal is applied from the top, coming from a BNC cable who's ground wire mesh and core cable are split up. The BNC cable's ground wire mesh is connected to the resonator's shield. The BNC cable's core is connected to a rotational slider which has a contact point to the coil. The lower end of the coil is connected to a vacuum feedthrough, leading to one pair of the trap's RF blades. Another

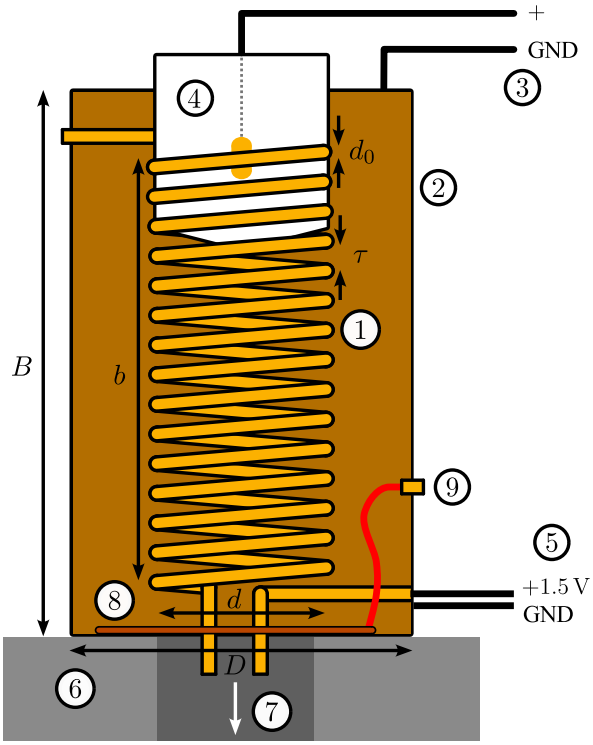

Figure 4.2.: Schematic drawing of the helical resonator: 1 - resonator coil with $d = 40.4\,\text{mm}$, $b = 155\,\text{mm}$, $d_0 = 5\,\text{mm}$ and $\tau = 10\,\text{mm}$, 2 - shield with $D = 84\,\text{mm}$ and $B = 255\,\text{mm}$, 3 - RF input, 4 - slider with contact point, 5 - battery, 6 - base plate, 7 - connection to vacuum feedthrough, 8 - pickoff coil, 9 - pickoff output SMA port. The numbers are taken from [116].

feedthrough pin connects the second pair of the trap's RF blades to a DC voltage of +1.5 V, supplied from a battery. By the battery's voltage offset, the trap potential in the radial plane becomes asymmetric, lifting the degeneracy of the radial modes[5].

Figure 4.3.: Image of the pickoff coil, screwed onto the baseplate, before mounting it together with the resonator on top of the vacuum chamber. While the pickoff coil was newly built, the baseplate is part of the existing helical resonator design from [116]. On the top left, one can see the pin connector which, when mounted, is plugged to the SMA connector on the inside of the resonator's shield (see (9) in Figure 4.2).

In the context of this thesis, the part for generating a pickoff signal was added to the helical resonator. For generating the pickoff signal, inductive coupling is used. The advantages in contrast to a capacitive divider, as presented in [133, 136], are circumventing stray capacitances and galvanic isolation of the pickoff from the main RF trap drive. The inductive pickoff is implemented using an array of four coils that is mounted onto the baseplate, which is henceforth referenced as the *pickoff coil*. A picture of the pickoff coil is shown in Figure 4.3. The idea behind a symmetrical four-coil arrangement was to increase the pickoff signal level compared to a single coil. Further, when testing the helical resonator in a loose assembly stage, the symmetric pickoff coil arrangement was found to make the pickoff signal more stable against any unintended movement of the resonator's main coil, compared to a single pickoff coil. While one end of the pickoff coil is connected to electrical ground on the baseplate, the other end, providing the pickoff-signal, is routed to a pin on the inside of the helical resonator's shield. The pin reaches through the shield without electrical contact and on the outside an SMA cable can be connected.

Besides the structure shown in Figure 4.2, the resonator shield is also closed from the top by a copper plate with the slider's BNC connector sticking through. The top plate is tightened by three metal rods and nuts on the side, screwing it to the baseplate. When mounting the helical resonator, it is advisable to have a helping hand[6] to hold the shield while connecting all pins of the vacuum feedthrough by screws.

Using a network analyser, the amplitude transfer function (spectrum) of the resonance circuit formed by the trap and the helical resonator was measured. The network analyser scans the frequency of a sinusoidal input signal for the helical resonator. For each frequency value, the network analyser measures the amplitude of the signal that is reflected from the resonator. Additionally, the amplitude of the pickoff signal that is sent to the network analyser via an additional input channel was measured. The spectra of both the resonator

[5]Lifting the radial modes' degeneracy is required for performing Doppler cooling with only a single laser beam.

[6]Mounting of the helical resonator was carried out together with postdoc Viktor Krutianskii.

reflection and the pickoff are displayed by the network analyser. Real-time analysis methods allowed monitoring the key parameters of the observable resonances, namely the centre frequency ω_0, the bandwidth σ and the quality factor Q, the latter being calculated by Equation 2.61. The quality factor was optimised by rotation of the slider, changing the connection point to the helical resonator's main coil. We aimed for a value of $Q \approx 200$, based on previous experience[7]. Recorded spectra are shown in Figure 4.4.

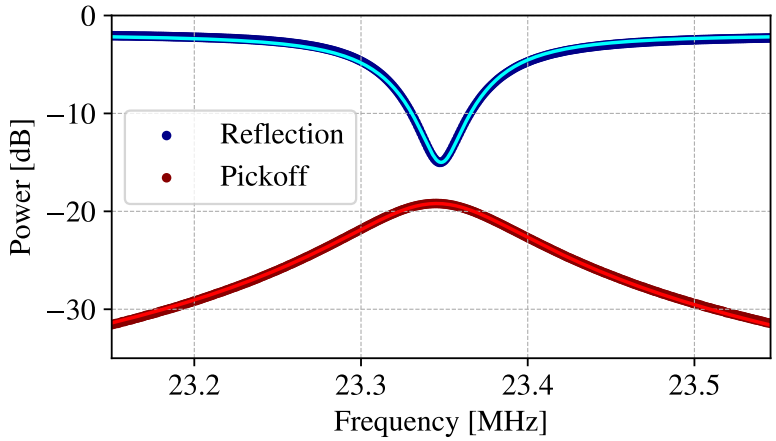

Figure 4.4.: Spectra of the pickoff signal (red) and resonator reflection (blue) measured using a network analyser. Both data sets (darker colours) were obtained with the helical resonator connected to the trap and are fitted (bright color) with a Lorentzian function on a logarithmic scale (least squares minimisation). Fit results are presented in the main text.

A Lorentzian least squares fit on the logarithmic scale gives $\omega_{0,\mathrm{ref}} = 23.348\,06(7)\,\mathrm{MHz}$ and $\omega_{0,\mathrm{pickoff}} = 23.345\,42(4)\,\mathrm{MHz}$. These resonance frequencies of reflection and pickoff signal differ by $2.64(8)\,\mathrm{kHz}$ but the origin of this difference is unknown. For all subsequent operation, we always chose the drive signal's frequency to minimise the reflection power as this maximises the voltages at the trap electrodes. Bandwidths (full-width-half-maximum) of $\sigma_{\mathrm{ref}} = 98.8(5)\,\mathrm{kHz}$ and $\sigma_{\mathrm{pickoff}} = 98.8(1)\,\mathrm{kHz}$ then lead to quality factors $Q_{\mathrm{ref}} = 236(1)$ and $Q_{\mathrm{pickoff}} = 236.3(2)$, calculated with Equation 2.61. A pickoff ratio is defined by $r_{\mathrm{p}} = P_{\mathrm{pickoff}}(\omega_0)/P_0$ with the input power P_0 (represented by $0\,\mathrm{dB}$ in Figure 4.4). The pickoff maximises to $-19.201(5)\,\mathrm{dB}$ which gives $r_{\mathrm{p}} = 1 : 83.2(1)$.

After these tests, the non-stabilised trap drive was connected to the trap and reflection and pickoff monitor output power were monitored by powermeters. Over the first few hours after turning the trap's RF drive signal on, the frequency for minimised reflection power showed drifts in the range of around $\pm 100\,\mathrm{kHz}$, presumably due to heating effects (more details are given in Section 4.1.3). After the drift had settled while adjusting the drive frequency to ensure minimum reflection power, ions were trapped successfully.

[7] V. Krutianskii, private communication, 01.09.2022

4.1.2. Stabilisation unit

For applying feedback to the power of the trap's RF drive signal, a stabilising unit is used. The stabilisation unit is an in-house design made by Gerhard Hendl at IQOQI Innsbruck. Similar versions of the stabilisation unit were previously used in other trapped-ion experiments in Innsbruck[8] [137]. The stabilisation unit performs proportional-integral control and requires two inputs additionally to the main RF input signal coming from the function generator. The additional inputs are a pickoff signal, proportional to the RF signal at the helical resonator, and a set-point that effectively represents the desired stable value of blade voltages. The set-point is internally represented as a voltage. A schematic, deconstructing the stabilisation unit into the individual parts that are relevant for stabilisation, is shown in Figure 4.5. More detailed circuit drawings with information on the exact components can be found in Appendix A.1. A photograph of the stabilisation unit with indicated connectors is shown in Figure 4.6.

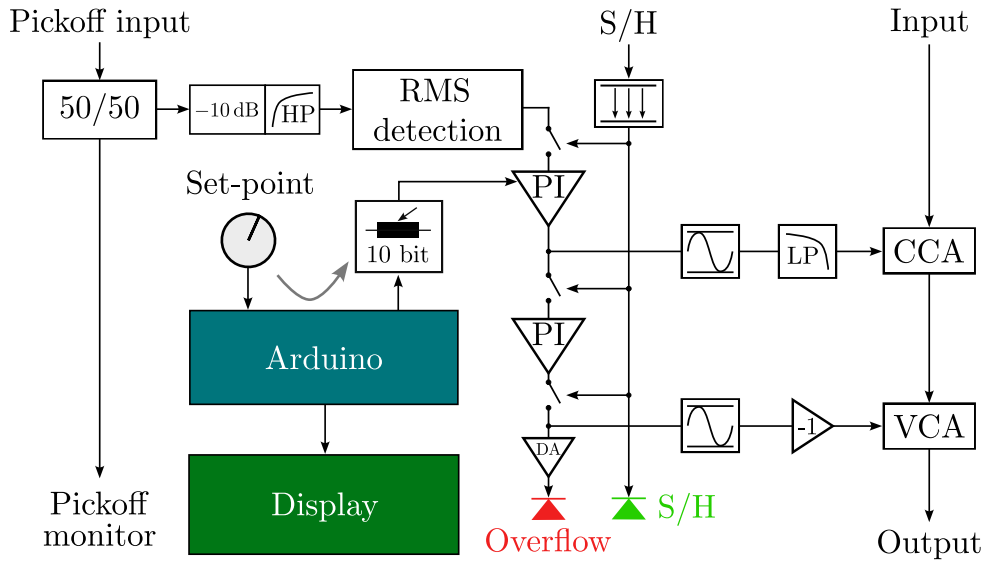

Figure 4.5.: Schematic of the internal components of the stabilisation unit that are relevant for the ion trap's RF power stabilisation. The meanings of all acronyms are given in the main text. Arrows indicate the signal flow.

Level changes to the incoming RF signal are applied in two steps by a current- and voltage-controlled attenuator (CCA & VCA). Larger changes in attenuation are performed by the VCA, setting the operation point for the CCA. Around the operation point, the CCA only changes its attenuation by small amounts such that the CCA's attenuation curve can be linearised. Both attenuators are controlled by outputs from differential amplifiers (DA) with proportional-integral (PI) gain. The DA output signals are current-limited by diodes. In the case of the CCA attenuation stage, a low-pass filter is applied to the control signal. For the VCA attenuation stage, the DA output is inverted, counteracting the inverting

[8] I. Pogorelov at AQTION, private communication, 29.08.2022

property of the slow DA unit. The DA controlling the VCA is designed for slow feedback while the other, controlling the CCA, applies fast feedback. The low-pass cut-off frequency of the CCA control part is at $(2\pi RC)^{-1} = 1.6\,\text{MHz}$. However, the actual bandwidth in the feedback loop is smaller as it is limited by the response time of the attenuators and the helical resonator's bandwidth of roughly 100 kHz. Output from the second PI unit that surpasses the operation range of the VCA is handled by an additional DA and signals an *overflow* through a red LED. In that case, the attenuation stays at its limit and the signal power is not stabilised. The fast PI unit takes its input signals from a pickoff- and set-point-voltage.

The pickoff voltage is proportional to the blade voltage, implemented by a root-mean-square (RMS) detector with a slope of 7.5 V/Vrms. A high-pass filter with a cut-off frequency of 257 kHz is applied before RMS detection. The pickoff input signal is split up with 50/50 ratio for monitoring and attenuated by 10 dB before entering the high-pass filter. Externally, the pickoff signal is already attenuated by 9 dB to match the expected signal level at the pickoff input which is around 7.7 dBm when applying 0 dBm at the main RF signal input. The value of the external attenuator was optimised in several trials. To prevent ground loops from the feedback channel, a 1:1 transformer is placed between pickoff coil and stabilisation unit. Without the transformer, several different sideband peaks were found in the spectrum of the pickoff monitor output signal. These peaks were completely removed by the transformer, resulting in a clean spectrum.

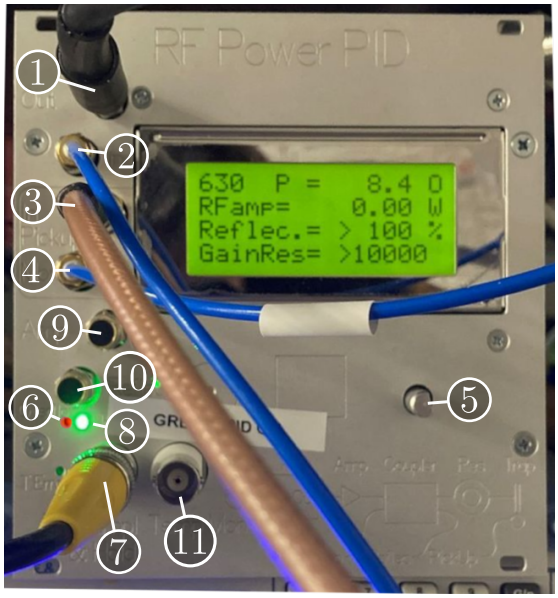

Figure 4.6.: Front plate of the stabilisation unit: 1 - RF input, 2 - RF output, 3 - pickoff input, 4 - pickoff monitor output, 5 - knob for set-point, 6 - overflow LED, 7 - S/H TTL input, 8 - S/H LED, 9 - amplifier pickoff input, 10 - reflection input, 11 - temperature monitor.

Active stabilisation can be stopped by opening electronic switches in front of both PI units, therefore implementing a so called *sample-and-hold* function (S/H). Sample-and-hold is triggered by an external TTL signal which is fed into the stabilisation unit by an optocoupler for galvanic isolation. The TTL signal further connects to a green LED, signalling active stabilisation when being bright at low TTL. The TTL signal is generated from the Pulse Box and is therefore controlled by the experiment control software TrICS (introduced in Section 3.1). The S/H function is only intended to be used for short periods of not more than a few seconds. Sample-and-hold relies on the capacitors in the PI units to hold the attenuator's control voltages and currents constant. On the timescale of a few minutes there still is charge leakage out of the capacitors in the PI units.

The set-point voltage is produced by a 10 bit digital potentiometer which receives its digital input from an Arduino microcontroller. The microcontroller produces the digital representation from an analogue potentiometer signal that is controlled manually by a knob (labelled as (5) in Figure 4.6). This set-point knob needs to be pressed in order to unlock changes of the set-point. Besides controlling the set-point, the microcontroller runs a routine that updates an LCD display with the value of the set-point and the power values at optional RF inputs. These optional RF inputs are designed to be the reflection and transmission pickoff signals from the bi-directional coupler. Further, the stabilisation unit is capable of displaying the expected RF signal power in the resonator and the gain of the amplifier. To calculate these values in a meaningful way, the internal functions in the microcontroller script need to be calibrated with the present pickoff ratio, and other power splitting ratios in the drive circuit, which was not done at the time of writing this thesis.

The stabilisation unit also features an independent circuit for temperature stabilisation of its internal electronics. The temperature stabilisation circuit includes a BNC output for monitoring and an LED that signals potential errors. In the experiments presented in this chapter, temperature stabilisation was active without signalling errors through the LED but stability of the monitoring signal has not been checked.

At the time of installing the stabilisation unit in our system, postdoc Matthias Bock from the 2D crystals team was working on an improved version of the stabilisation unit. The main improvements are tunable PI-parameters, set-point control via an external signal (LAN connection) and fixing noise issues at the RMS detection unit.

4.1.3. Advice for setting up the stabilisation unit

Driving the helical resonator at a power of several watts, as needed for ion trapping, heats it up by several degree Celsius because of the internal resistance. These temperature changes have an effect on the resonance circuit's transfer function, leading to drifts of the RF power that is present in the helical resonator, and consequently also to drifts of the helical resonator's pickoff signal power. For observing these changes, the RF power of the stabilisation unit's pickoff monitor output and the bi-directional coupler's reflection pickoff are logged. It was previously found that, subsequently to remounting a helical resonator, one can observe large jumps in the RF power[9], also termed as *spikes* in the following. Spikes usually disappear after approximately a day, which presumably is the time it takes the helical resonator to reach an equilibrium temperature. However, when having active stabilisation running, the stabilisation unit reacts to the spikes by applying heavy changes in the signal attenuation. With continuously changing input power, the resonator can hardly reach a stable equilibrium temperature. A solution that worked in our setup was to first drive the circuit in sample-and-hold (S/H) mode without active stabilisation until the spikes disappeared. If spikes persist, tightening cable connections and slightly moving the resonator's slider turned out to be helpful. Before then activating

[9] V. Krutianskii, private communication, 30.11.2022

the RF power stabilisation by turning off S/H, one should choose a set-point that closely matches the current RF power such that big initial changes of the RF power and overflow at the attenuators are avoided.

4.2. Experiments and results

At the point where ions could be trapped reliably, we[10] started measuring radial motional mode frequencies on a single trapped ion to assess the performance of the stabilisation system. This section presents the performed experiments and their results. Additionally, tests using only electronic signals from the drive circuit for investigating limitations of the radial frequency stabilisation system are described.

4.2.1. Radial mode frequency calibration

It is useful to run a calibration for the radial mode frequencies in dependence of the RF power, controlled by the stabilisation unit's set-point. Such a measurement gives a rough guide for power values at the stabilisation unit's pickoff monitor output when aiming at a specific radial mode frequency. Calibration of the radial mode frequencies was carried out multiple times during the process of optimising the pickoff signal power (resolving ground loops and changing the pickoff signal's attenuation). In the calibration measurement with the final version of the drive circuit (schematic drawing shown in Figure 4.1), the power at the stabilisation unit's pickoff monitor output was not logged and the radial mode frequencies were only measured in dependence of the stabilisation unit's set-point. These final calibration measurements are presented in Appendix B.1. In this section, a previous calibration measurement is presented which, although being outdated, provides a complete example of how such a calibration measurement should be carried out. For the subsequently presented calibration, the drive circuit deviates from the final version by a missing transformer in the pickoff signal, different signal attenuation, and power supply connections were not sharing the same multi-socket. The version of the drive circuit used here is the same as the one used for the long time radial mode frequency stability measurements in Section 4.2.2.

Measurements of the radial mode frequencies were done using a single ion, prepared with the methods introduced in Section 3.2.1. The initialisation procedure consisted of Doppler-cooling for 5 ms, 80 µs of optical pumping to $4^2S_{1/2,m=-1/2}$, and finally 6 ms of resolved sideband cooling to the motional ground-state of the radial modes[11]. Sideband cooling was performed on the $4^2S_{1/2,m=-1/2}$ to $3^2D_{5/2,m=-5/2}$ optical qubit transition at 729 nm. After sideband cooling, optical pumping was repeated with a duration of 80 µs.

[10] For all the experiments presented in this section, I was assisted by PhD students James Bate and Marco Canteri.

[11] Axial modes were not used in the experiments of this chapter. Ground state cooling of them is therefore not required.

Next, a fixed frequency 729 nm laser pulse on the $4^2S_{1/2}$ to $3^2D_{5/2}$ transition was carried out, followed by electron shelving. The 729 nm laser pulse was performed with the radial beam, which is aligned perpendicular to the ion string (see Figure 3.2b). These sequences, consisting of initialisation, the 729 nm laser pulse and electron shelving, were repeated for different frequencies of the 729 nm pulse by adjusting the frequency of an AOM in the 729 nm beam path, and thus, recording spectra of the $4^2S_{1/2}$ to $3^2D_{5/2}$ transition. First, a spectrum of only the carrier transition was recorded once with a 15 ms long 729 nm pulse in a frequency range of 400 kHz. Then, spectra containing only the blue sideband transitions of both radial modes were recorded with a 5 ms long 729 nm pulse in a frequency range of 80 kHz. The 729 nm light's intensity was adjusted to reduce power broadening [44] in order to resolve the frequency splitting between both radial modes. An example scan, containing the radial blue sideband, is shown in Figure 4.7a. Besides the excitation peaks of both radial modes, smaller resonances were found, but their origin remains unclear. A double-Lorentzian least squares fit is used to determine the centre frequencies of the radial mode peaks. To reduce the influence from the additional smaller peaks on the fit, the fit routine is executed in two iterations. The first iteration is used to detect outlier points, e.g. from the smaller peaks, which deviate more than three standard deviations from the fit line. These points are then excluded in the second fit iteration.

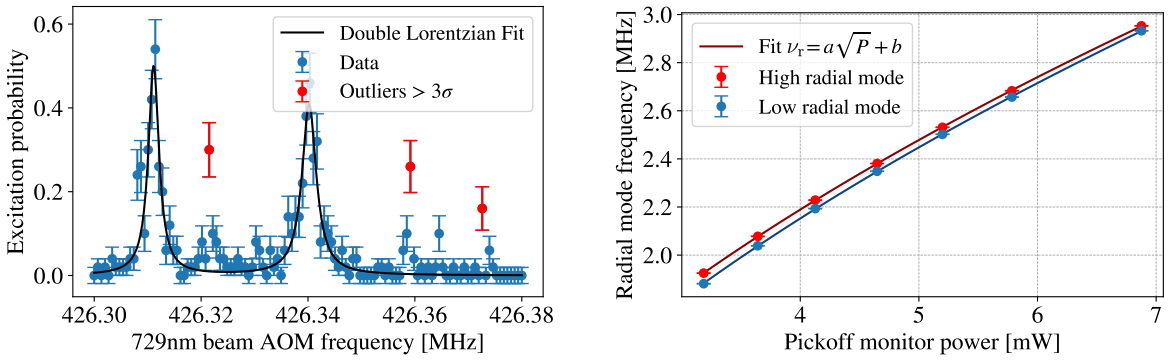

(a) **(b)**

Figure 4.7.: a) Radial blue sideband spectrum data (blue dots) measured on a single ion. The fit line (black) is a double-peak Lorentzian function. The fit is the second iteration, excluding data points with more than three standard deviations (red) from the first fit iteration. **b)** Calibration curve of the radial mode frequencies, labelled as *high* (red) and *low* (blue), in dependence of the stabilisation unit's pickoff monitor output power. Radial mode frequencies were obtained from fitting spectra of the blue radial sideband and error bars correspond to the fit errors in the centre frequencies of the excitation peaks. A least squares fit of the form $\nu_r = a \cdot \sqrt{P} + b$ is applied to the data sets from both modes (solid lines). Fit parameter results are given in the main text.

Spectroscopy scans containing the radial mode's blue sidebands were repeated for different settings of the stabilisation unit's set-point. The upper limit for the set-point was defined by the highest setting before the stabilisation unit signals overflow. For each of the chosen

set-points, the power at the stabilisation unit's pickoff monitor output was measured and the frequencies of both radial modes were calculated as the differences between the carrier frequency and the respective radial mode's centre frequency. The resulting curves, mapping the stabilisation unit's pickoff monitor power to the radial mode frequencies, is shown in Figure 4.7b. Error bars represent the uncertainties of the centre frequency parameters in the spectroscopy scan fits. Radial mode frequencies of up to 2.9530(7) MHz were measured.

The theory model for how the radial mode frequency varies with the blade voltage is given by Equations 2.32 and 2.33. The RF power is proportional to the square root of the blade voltage, motivating a fit of the form $\nu_\mathrm{r}(P) = a\sqrt{P}$. It turned out that for better representation of the data (based on χ^2/d.o.f.), a different model $\nu_\mathrm{r}(P) = a\sqrt{P} + b$ was needed. Using a least squares fitting algorithm, the determined fit parameters are $a = 1.225(2)\,\mathrm{MHz}/\sqrt{\mathrm{mW}}$ and $b = -260(5)\,\mathrm{kHz}$ for the higher frequency radial mode and $a = 1.252(3)\,\mathrm{MHz}/\sqrt{\mathrm{mW}}$ and $b = -351(6)\,\mathrm{kHz}$ for the lower frequency radial mode. The dependence of the radial mode frequencies and their splitting on the stabilisation unit's set-point can be found in Appendix B.1.

It is not fully clear why the data is better represented by a model differing from the theory by a frequency offset. The obtained fit curves allow for negative mode frequency values at low pickoff monitor power. The same behaviour is also obtained in the calibration measurement carried out with the final version of the drive circuit, presented in Appendix B.1. A possible explanation is an offset between the stabilisation unit's pickoff monitor output power and the power that is distributed to the trap. With such an offset, even if there is power measured at the pickoff monitor output, there is no power distributed to the trap, leading to the shift of the calibration curve along the horizontal axis. Still, the calibration in Appendix B.1 represents the actual relation between the stabilisation unit's set-point and the radial mode frequencies in our setup. When aiming at a particular radial mode frequency, that calibration curve provides a guide for the corresponding set-point at the stabilisation unit.

4.2.2. Stability during one hour

Although it is straightforward to check the stability of the RF power from the logged data, the quantities of interest are the radial mode frequencies of an ion. This section presents an experiment where one of the two radial mode frequencies was measured repeatedly during one hour.

The measurements were carried out on a single ion, initialised by 5 ms Doppler cooling and 80 µs optical pumping. Excitation spectra of the higher frequency radial mode's red sideband were recorded repeatedly with a 5 ms long 729 nm laser pulse, whose frequency is controlled by an AOM. The radial 729 nm laser beam was used and attenuated such that peaks in the excitation spectra had a full-width-half-maximum of 0.2 to 0.3 kHz. Lorentzian functions are fitted to the spectra, yielding uncertainties in the peak's centre frequency on the order of a few hertz. Again, two iterations of a least squares fit are performed. Data

points of additional smaller peaks with a deviation of more than 5σ to the first fit are excluded in the second fit. The deviation threshold was changed to 5σ compared to the previously used deviation of 3σ in order to ensure that only data points from additional peaks get flagged. The radial mode frequency was calculated by the difference between the AOM frequencies which tune the 729 nm beam on resonance with the carrier and red sideband transition. With the carrier AOM frequency drifting at the level of a few tens of Hertz per minute and scans of the radial sideband taking a few minutes, the resulting frequency drifts are comparable to the expected frequency stability of the radial mode which is on the order of 100 Hz. Therefore, care had to be taken to determine the carrier AOM frequency to associate with each measurement of the sideband AOM frequency. Specifically, as shown in Appendix B.2, a carrier AOM frequency was always determined from clock operation (as explained in Section 3.2.3) in between recording two radial sideband spectra. For each radial sideband AOM frequency, the corresponding carrier AOM frequency was calculated by a linear interpolation at the time stamp where the peak in the radial sideband scan was reached. The time order and duration of the clock and sideband measurements, as well as a plot of the carrier AOM frequency drift, is presented in Appendix B.2. In total, $N = 13$ excitation spectra of the higher frequency radial mode were recorded during one hour. At the same time, the stabilisation unit's pickoff monitor output power was logged. The time trace of the higher radial mode's frequency, overlapped with the time trace of the stabilisation unit's pickoff monitor output power is shown in Figure 4.8.

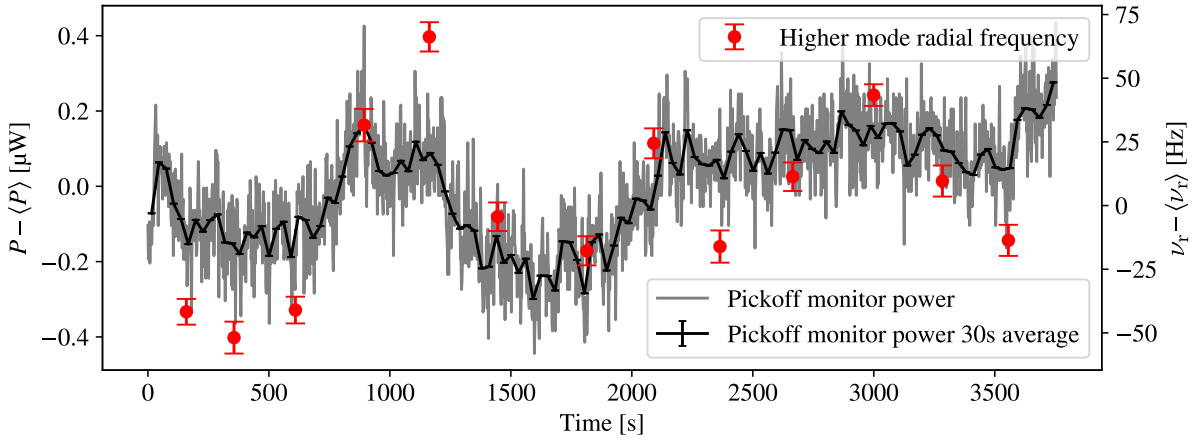

Figure 4.8.: Time traces of both the stabilisation unit's pickoff monitor output power P (grey) and the frequency of the higher frequency radial mode ν_r of a single trapped ion (red) over a duration of close to one hour. The black connected data points are averages of the pickoff monitor output power (grey) during 30 s. The pickoff monitor output power and the radial mode frequency are displayed relative to their mean values $\langle P \rangle$ and $\langle \nu_r \rangle$ which are given in the main text.

The recorded radial mode frequency data has a mean value of $\langle \nu_r \rangle = 2.682\,342(10)$ MHz and a standard deviation of $\sigma_\nu = 35(3)$ Hz, resulting in a fractional instability of $\sigma_\nu / \langle \nu_r \rangle = 1.3(1) \cdot 10^{-5}$ during one hour. Peak-to-peak fluctuations of the radial mode frequency are

118(9) Hz. The power at the stabilisation unit's pickoff monitor output has a mean value of $\langle P \rangle = 5.766\,574(4)$ mW and a standard deviation of $\sigma_P = 153.43(8)$ nW, resulting in a fractional instability of $\sigma_P/\langle P \rangle = 2.661(1) \cdot 10^{-5}$ during one hour.

Visually, the plotted time traces in Figure 4.8 only show a slight sign of correlation. For a quantitative analysis the correlation coefficient was calculated, defined as [100]

$$r = \frac{\sigma_{\nu,P}}{\sqrt{\sigma_\nu \cdot \sigma_P}} \tag{4.1}$$

where σ_ν and σ_P are the standard deviations of the radial mode frequency and of the pickoff monitor output power, respectively, and $\sigma_{\nu,P}$ is the covariance of the radial mode frequency and the pickoff monitor output power. Significant correlation among N data points is given if [100]

$$|r| \geq \frac{2}{\sqrt{N}}. \tag{4.2}$$

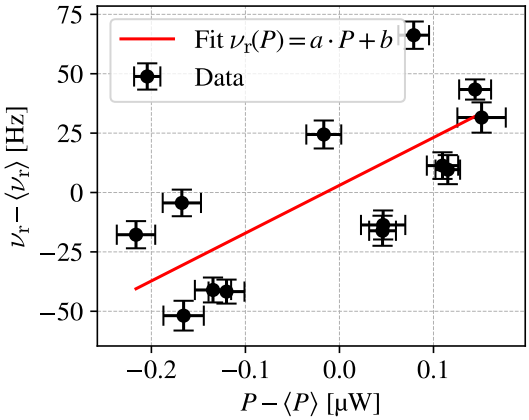

Figure 4.9.: Correlation plot of radial mode frequency vs. pickoff monitor output power using the data in Figure 4.8. Power and frequency data is plotted relative to the respective mean values.

For the pickoff monitor output power, averages during 30 s were calculated. To match the number of radial mode frequency samples, interpolated power values were calculated for the time stamps of the measured radial mode frequencies. Figure 4.9 shows a correlation plot of the $N = 13$ interpolated power values and their corresponding measured radial mode frequencies. A linear least squares fit $\nu_r(P) = a \cdot P + b$ gives $a = 201(12)\,\mathrm{kHz\,mW^{-1}}$ and $b = 1.52(7)$ MHz. The correlation coefficient is $r = 0.7(1)$. The condition for significant correlation in Equation 4.2 is fulfilled as $2/\sqrt{N} = 0.55$ for $N = 13$, but the observed correlation is not perfect ($|r| < 1$).

The powermeter that was used for measuring the stabilisation unit's pickoff monitor output power has a specified minimum resolution of 0.01 dB $= 2.3 \cdot 10^{-3}$ [134]. We interpret this as an error bar which is a 0.002 fraction of any measured power value when comparing two different power values. The measured power fluctuations at the pickoff monitor output are well below the specified minimum resolution of the powermeter. It is therefore not clear if the measured power fluctuations are really present in the stabilisation unit's pickoff monitor output power or if they are introduced by the powermeter itself. Using the calibration from Section 4.2.1, the measured fractional instability of the stabilisation unit's pickoff monitor output power $\sigma_P/\langle P \rangle$ translates to a fractional instability in the radial mode frequency of $\sigma_\nu/\langle \nu_r \rangle = 1.456(3) \cdot 10^{-5}$. The difference between the measured and the predicted fractional stability of the radial mode frequency is $1.4(10) \cdot 10^{-6}$ which is not considered to be significant. Any fluctuations in the pickoff power data that are purely caused by the limited resolution of the powermeter should not have an effect on the radial mode frequency. The measured fluctuations in the radial mode frequency are then well

explained by the fluctuations in the pickoff monitor output power, suggesting that the powermeter is indeed capable of resolving fluctuations on the 10^{-5} level, two orders of magnitude better than its minimum specification.

4.2.3. Motional coherence

The measurement in the previous section provides a stability measure for the timescale of one hour. However, we want to perform quantum logic gates using the radial modes which happen on the timescale of tens to hundreds of microseconds. In order to retain coherence, the radial mode frequency has to stay stable on the timescale of those gate operations. In Section 2.5.1, the Ramsey experiment was introduced as a practical way to measure coherence. To apply the concept of the Ramsey experiment to a motional mode, the pulse sequence is slightly extended to the so-called motional Ramsey experiment [138]. For all motional Ramsey experiments in this section, a single ion was initialised to $4^2S_{1/2,m=-1/2}$ by 5 ms Doppler cooling, 80 µs optical pumping and 3 ms sideband cooling of the radial modes. In the following, the used pulse sequence for motional Ramsey experiments is described. The motional Ramsey experiments used the higher frequency radial mode at 2.432(2) MHz.

The starting point of the motional Ramsey experiment is still the creation of a superposition state by a $\pi/2$-pulse on the carrier transition. Setting the phase of this pulse to $\phi = 0$ produces the state $|+\rangle$. For only probing decoherence of the motional mode, the superposition state is then mapped to a qubit in the motional mode. Mapping is done by a π-pulse on the radial motional mode's blue sideband with a phase of $\phi = 0$. During a wait time τ, the phases of the motional superposition state and the laser field evolve individually before mapping back with a blue sideband π-pulse. The second mapping pulse has its phase set to $\phi = \pi$ which reverses the first mapping rotation instead of appending the rotation angle, making the sequence insensitive to constant errors in the sideband pulse duration. The motional Ramsey experiment ends with a second carrier $\pi/2$ pulse which has a phase of ϕ. The pulse sequence of the motional Ramsey experiment is shown in Figure 4.10a. Scanning the phase of the Ramsey experiment's final carrier $\pi/2$ pulse produces fringes of the excitation probability. Fringes from a motional Ramsey experiment on the higher frequency radial motional mode with a wait time of $\tau = 0$ ms are exemplified in Figure 4.10b. The fringes are fitted (least squares) with a sinusoidal function given by Equation 2.78 to extract their contrast and phase.

The motional Ramsey experiment was repeated for a range of wait times τ, showing how the fringe contrast drops off due to decoherence. Three sets of experiments were carried out: First, the motional Ramsey experiment as just described, which will be referred to as the "basic configuration". Second, the motional Ramsey experiment was carried out with activated line-trigger. Third, a spin echo pulse was inserted halfway into the wait time, as shown in Figure 4.10a. Figure 4.11 presents the experimental results, alongside least squares fits to the data sets that are now described.

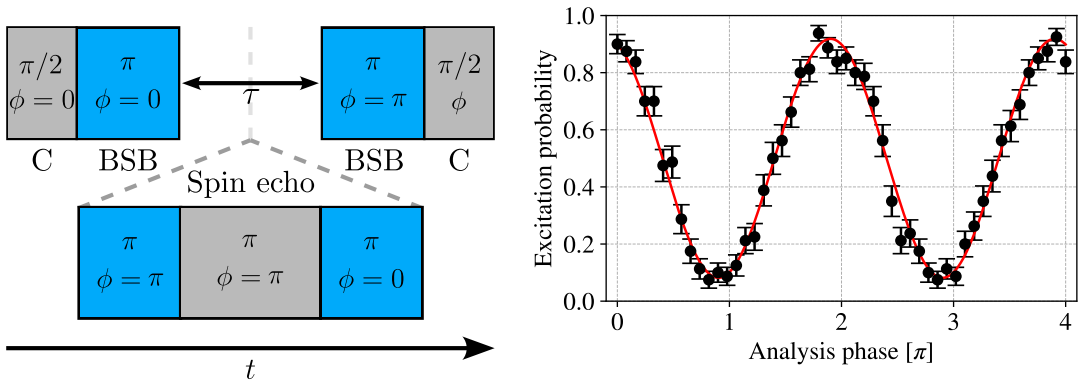

(a) (b)

Figure 4.10.: a) Pulse sequence for a motional Ramsey experiment. The basic Ramsey sequence of two carrier $\pi/2$-pulses (C, grey) spaced by a wait time τ is extended by mapping the superposition state to the motional sideband and back by blue sideband π-pulses (BSB, blue). An optional spin echo π-pulse on the carrier, surrounded by mapping pulses can be used to invert the phase evolution for the second half of the wait time. Blue sideband pulses alternate between a phase of zero and π to cancel out miscalibrations of their rotation angle. The phase of the final carrier $\pi/2$-pulse is scanned to obtain fringes of the excitation probability as exemplified in **b)**. Data is taken from a motional Ramsey experiment on the optical qubit's radial blue sideband for no wait time ($\tau = 0\,\mathrm{ms}$) and without the application of a spin echo.

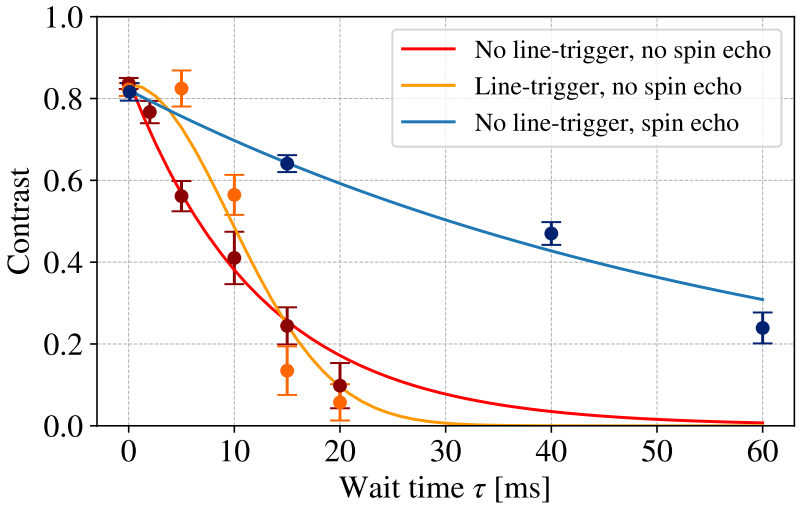

Figure 4.11.: Decay curves from motional Ramsey experiments on the higher frequency radial mode. Data and fits from three sets of Ramsey experiments are shown: a set without line-trigger and without a spin echo (red), a set with active line-trigger and without a spin echo (orange) and a set without line-trigger and with the use of a spin echo (blue). Fit functions are described in the main text.

In the basic configuration, an exponential decay fit of the form $C(\tau) = C_0 \cdot \exp(-\tau/\tau_0)$ gives a $1/e$ time of $\tau_0 = 13(1)\,\mathrm{ms}$ with a contrast of $C_0 = 0.85(1)$ at $\tau = 0\,\mathrm{ms}$. As introduced in Section 2.5.2, an estimate of the motional mode's linewidth can, in the case of exponentially shaped decay, be calculated by the inverse of the $1/e$ decay time, yielding 77(6) Hz which, for the used mode frequency of 2.432(2) MHz, results in a fractional instability of $3.3(3) \cdot 10^{-5}$. For active line-trigger, no significant change in the decay-time was observed. However, the shape of the decay seen in the data is better represented by a Gaussian function of the form $C(\tau) = C_0 \cdot \exp(-(t/\tau_{\mathrm{LT}})^2)$ with $1/e$ decay time $\tau_{\mathrm{LT}} = 14(2)\,\mathrm{ms}$ and initial contrast $C_0 = 0.83(3)$. The change of shape was not expected and its origin is unclear. When applying a spin echo, the decay is again fitted by an exponential function of the form $C(\tau) = C_0 \cdot \exp(-\tau/\tau_{\mathrm{SE}})$ with the initial contrast $C_0 = 0.82(3)$ and a contrast reduction to the $1/e$ fraction after $\tau_{\mathrm{SE}} = 61(9)\,\mathrm{ms}$.

With a spin echo, the contrast improved for all non-zero wait times that were measured, which are all on the order of tens of milliseconds. The inverse of such tens of milliseconds long decay times are frequencies on the order of tens of hertz. The spin echo pulse cancels out noise that is slower than these frequencies. The remaining noise that is limiting the coherence time must therefore be at higher frequencies.

4.2.4. Investigation into limitations

Electronic environment

Coupling between the drive circuits for the radial and the axial trap electrodes was observed. At the time of introducing the trap's new RF drive system, there was ongoing development on the axial drive electronics, involving a filter with a switchable cut-off frequency and a voltage addition circuit for axial ion shuttling operations. It turned out that toggling the filter switch changes the optimal RF frequency for minimum reflection from the trap by around 50 kHz.

Further, the stabilisation unit was found to be sensitive to changes in the electronic environment. For example, relocating the stabilisation unit's power supply to a different socket, while keeping all other parameters the same, resulted in a change of 0.3% in the pickoff monitor output power. Such a change is already significantly larger than peak-to-peak fluctuations under active stabilisation.

Initially, various sideband peaks with frequency spacings in the range of tens of megahertz to the RF drive frequency were observed in the spectrum of the pickoff monitor output signal. Sideband peaks can occur when ground loops are present in the laboratory electronic network. Organising power distribution in a star shaped network and decoupling cross connections galvanically by optocouplers or transformers can help to dissolve ground loops [139]. Including a transformer on the pickoff signal, as indicated in Figure 4.1, and using the same multi-socket for powering all devices in the trap's drive circuit, resulted in a clean spectrum with no visible sidebands.

Timescale of hours - humidity influence

Logged RF power data, both at the stabilisation unit's pickoff monitor output and at the bi-directional coupler's reflection pickoff output[12], shows oscillations with a period of roughly 90 min and a fractional amplitude on the 10^{-4} level[13]. Oscillations with the same period were also found in other logged experimental parameters like laser powers, but are visible with high contrast in the laboratory humidity data with a peak-to-peak difference of 0.8(1) % relative humidity[14]. To check if the electronics in the stabilisation unit are sensitive to the laboratory humidity, a slightly wet sponge was placed inside the back of the stabilisation unit box. With a few minutes of delay after placing the sponge inside the box, the pickoff monitor output power showed a change that was approximately four times bigger than the pickoff monitor output power's initial peak-to-peak fluctuations. The sponge-test was repeated a few times, always showing similar results, which confirms that the stabilisation unit is sensitive to the laboratory humidity.

Logged data from the laboratory humidity and the stabilisation unit's pickoff monitor output power over 50 h was used for a quantitative analysis. During that time interval, the mean power of the pickoff monitor output was $\langle P \rangle = 4.3888(1)\,\mathrm{mW}$ and the mean relative humidity was $\langle H \rangle = 38.55(1)\,\%$, where the uncertainties are the errors of the mean values. Average values of the stabilisation unit's pickoff monitor output power were calculated over intervals of 5 min with the corresponding time stamp also being an average. In total, there are 600 data points each of the humidity and the pickoff monitor output power. Figure 4.12a shows a 10 h extract of the recorded time traces.

For a correlation analysis, a humidity data point was assigned to each power data point where the humidity data point with the time stamp closest to the power data point's time stamp was used. All further analysis was carried out using only the deviations from the mean values $\Delta H = H - \langle H \rangle$ and $\Delta P = P - \langle P \rangle$. The resulting correlation plot is shown in Figure 4.12b and the correlation coefficient is calculated to be $r = 0.83(1)$. For $N = 600$ data points, the threshold for significant correlation, given by Equation 4.2, is very low at 0.08, highlighting that the laboratory humidity strongly affects the pickoff monitor output power, and consequently the RF power that is delivered to the trap. A linear least squares fit $\Delta P = a \cdot \Delta H$ on the correlation data, has a slope of $a = 0.33(1)\,\mu\mathrm{W}\,\%^{-1}$. Using the calibration curves obtained in Section 4.2.1, the amplitude of humidity fluctuations of 0.8(1)% is predicted to move the radial mode frequency of a single ion in our trap by 80(10) Hz.

Since the humidity also affects other devices in the laboratory, getting rid of the humidity oscillations is expected to be beneficial for the whole experimental setup. The humidity control system is shared with two neighbouring laboratories while air conditioning is

[12] Measured using Mini-Circuits PWR-SEN-4GHS powermeters.

[13] As shown in Section 4.2.2, the resolution of the powermeters is at least at the 10^{-5} level.

[14] Recorded with a Thorlabs TSP01 sensor, having an accuracy of 2 % relative humidity and a resolution of 0.1 % relative humidity. In the context of humidity, the unit percent refers to the relative humidity.

controlled individually. Fixing the humidity control system's behaviour is therefore a non-trivial task.

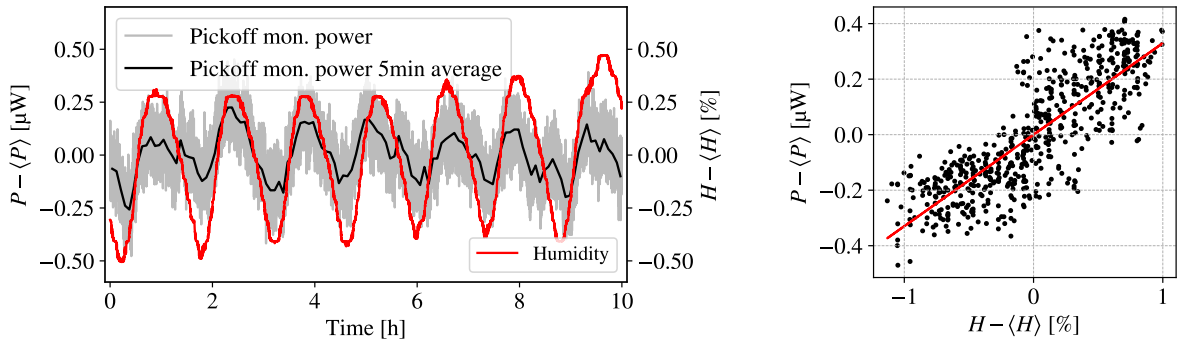

(a) **(b)**

Figure 4.12.: a) Time traces of laboratory humidity (red) and the stabilisation unit's pickoff monitor output power (grey). The pickoff monitor output power is averaged over a period of 5 min (black). For better visibility of the oscillations, only a 10 h extract of the full 50 h data set is plotted. **b)** Correlation plot of the averaged pickoff monitor output power values and the humidity from the full 50 h data set. The linear fit $P - \langle P \rangle = a \cdot (H - \langle H \rangle)$ (red line) has a slope of $a = 0.33(1)\,\mu\mathrm{W}\,\%^{-1}$.

Timescales shorter than minutes - electronic noise

The humidity influence only explains half of the observed total peak-to-peak fluctuations in the stabilisation unit's pickoff monitor output power, shown by the grey data in Figure 4.12a. On timescales much shorter than 20 min, the pickoff monitor output power still shows fluctuations with a standard deviation on the 10^{-5} level.

A possible source of the remaining fluctuations in the stabilisation unit's pickoff monitor output power could be instability in the power that is provided by the function generator (introduced in Figure 4.1). The stability of the function generator's output power was measured by recording a power time trace using an RF powermeter[15] with a sampling rate of 33 Hz. The function generator's output power was set to 1.19 mW. In the first 10 min after switching on the output, the power drifted down by roughly 1 µW. From there on, the function generator's output power was logged for two hours and the resulting time trace is shown in Figure 4.13a. The mean value of the function generator's output power over the two hour measurement is $\langle P \rangle = 1.189\,614\,90(2)\,\mathrm{mW}$. The histogram of the recorded data, plotted in Figure 4.13b, shows a Gaussian distribution where an unweighted least squares Gaussian fit yields a standard deviation of $\sigma = 126(5)\,\mathrm{nW}$. The fractional instability in the stabilisation unit's input power is therefore $\sigma/\langle P \rangle = 1.06(4) \cdot 10^{-4}$. In Section 4.2.2 the fractional instability of the stabilisation unit's pickoff monitor output power was found to

[15]The same model as in previously presented measurements was used: Mini-Circuits PWR-SEN-4GHS.

be $2.661(1) \cdot 10^{-5}$ during one hour. Power fluctuations in the function generator's output signal are therefore reduced by the stabilisation unit.

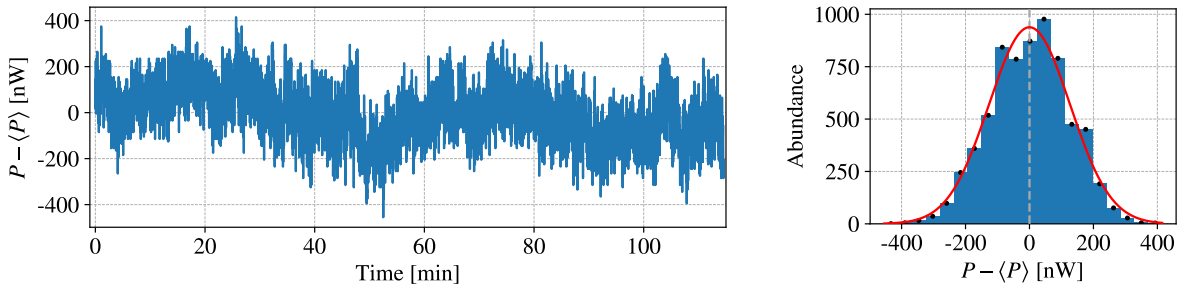

(a) **(b)**

Figure 4.13.: a) Time trace of the function generator's output power, measured over two hours by directly connecting the function generator output to a powermeter. Power data is plotted as the deviation $\Delta P = P - \langle P \rangle$ from the mean value $\langle P \rangle = 1.189\,614\,90(2)\,\mathrm{mW}$. The standard deviation is extracted from the data's histogram **(b)**. A Gaussian fit $N(\Delta P) = A \cdot \exp(-(\Delta P/\sigma)^2/2)$ (red curve) on the bin centres (black dots) gives a standard deviation of $\sigma = 126(5)\,\mathrm{nW}$.

The remaining power fluctuations on the 10^{-5} level are likely introduced by the stabilisation unit itself. In a given frequency band, the stabilisation unit can only detect and consequently react to fluctuations in the pickoff power if these fluctuations are larger than the stabilisation unit's internal noise background in that frequency band. The stabilisation unit's noise spectrum then translates to the trap's drive circuit. In Section 4.2.3 it was shown that the motional coherence is limited by noise faster than tens of hertz, suggesting that the stabilisation unit's noise is at such frequencies. In Section 4.2.3, exponential decay of the radial mode's motional coherence was observed, relating to a Lorentzian distribution of fluctuations in the radial frequency, and consequently in the trap's RF power. It is not clear if the stabilisation unit is responsible for transforming the Gaussian distribution of the function generator's output power to a Lorentzian distribution of the trap's RF power. Tracking down the exact source of the stabilisation unit's noise is a complex task. However, we are aware that some of the stabilisation unit's electric components are comparatively cheap and not specifically designed for low noise operation, which holds true in particular for the RMS detection units. Such primitive components are typically also easily affected by environmental parameters like temperature and humidity, explaining the earlier reported influence of the laboratory humidity on the stabilisation unit's pickoff monitor output power. At the time of writing this thesis, a redesign of the stabilisation unit, where the RMS detectors are replaced by components with favourable noise properties amongst addressing other issues, was already in use in the 2D crystals experiment, showing improved motional coherence times of the radial motional modes[16].

[16]M. Bock, private communication, 18.12.2023

4.3. Conclusion

Drifts of the radial motional mode frequencies of the trap have been actively compensated by stabilising the power of the trap's radio frequency drive signal. Using a single ion, the higher frequency radial mode's frequency was measured repeatedly over the course of one hour, showing peak-to-peak fluctuations of 118(9) Hz around a mean value of 2.682 342(10) MHz and a standard deviation of 35(3) Hz. The observed frequency fluctuations are a significant improvement compared to previously measured drifts of 6 kHz during only 10 min. The radial mode frequencies are tuned by the set-point of a stabilisation unit, reaching a maximum mode frequency of 2.9530(7) MHz. The motional coherence time ($1/e$ contrast decay) of the higher frequency radial mode without line triggering and without the application of a spin echo was measured to be 13(1) ms. Motional coherence is not limited by line-cycle induced noise at harmonics of 50 Hz, but by other noise sources, faster than tens of hertz. The stabilisation system, more precisely, some of its internal electronic components, are sensitive to the laboratory humidity. Humidity oscillations with a peak-to-peak amplitude of 0.8(1) % relative humidity and a period of approximately 90 min were observed in our laboratory. The recorded humidity changes are expected to cause radial mode frequency changes of 80(10) Hz. On timescales shorter than 20 min, fractional fluctuations of the RF power that is delivered to the trap are on the order of 10^{-5} and originate from noise that is introduced by imperfect electric components in the stabilisation unit. These observations are consistent with the short-term radial mode frequency stability of $3.3(3) \cdot 10^{-5}$, obtained from the motional coherence time. Many of the encountered problems are expected to be reduced by a new design of the stabilisation unit which is currently undergoing testing in other trapped-ion experiments in Innsbruck.

5. Direct drive of the $^{40}Ca^{+}$ ground-state qubit

Atomic ground-state transitions with energy splittings in the microwave or radio frequency regime have long relaxation times compared to those at optical frequencies because the spontaneous emission rate scales with the third power of the transition frequency [44]. Ground-state transitions at sub-optical frequencies are therefore favourable for implementing qubits with very long coherence times and atomic ground-state hyperfine levels have been used as quantum memories in both neutral atoms [140] and trapped ions [108]. The $4^2S_{1/2}$ ground-state in $^{40}Ca^{+}$ contains two Zeeman levels: $|S\rangle = 4^2S_{J=1/2,m_J=-1/2}$ and $|S'\rangle = 4^2S_{J=1/2,m_J=+1/2}$ where m_J is the magnetic quantum number. The frequency splitting of these two states at the external magnetic field value used during this thesis of $4.148(2)\,\mathrm{G}$[1] is then, by Equation 2.35, $\omega_0 = 2\pi \cdot 11.623(5)\,\mathrm{MHz}$ which is in the radio frequency (RF) regime. Another advantage of the ground-state qubit in $^{40}Ca^{+}$ is that differential AC Stark shifts due to far detuned laser fields can be negligible [42]. In our experiment, these shifts are caused by single photons in the cavity surrounding the trap or by the 806 nm laser field that is used to stabilise its length. Recently, our group used the $|S\rangle$ - $|S'\rangle$ qubit encoding as a quantum memory for storing entanglement with a photon, in the context of demonstrating a quantum repeater implementation [42]. In that demonstration, dynamical decoupling, as introduced in Section 2.5.3, was used to preserve the coherence of the $|S\rangle$ - $|S'\rangle$ quantum memory and a Ramsey contrast of 0.67(3) after a wait time of 66 ms was reported. The required coupling between $|S\rangle$ and $|S'\rangle$ was achieved using a sequence of three π-pulses on the $4^2S_{1/2}$ to $3^2D_{5/2}$ transition at 729 nm. At optical frequencies, there is significant coupling to an ion's motion, which in the repeater demonstration experiment was identified as the dominant source for a loss of Ramsey contrast. In contrast, at the ground-state qubit's transition frequency of 11.62 MHz, the Lamb-Dicke factor is on the order of 10^{-9} for the experiment's trap frequencies, which lie in the single megahertz regime. Therefore, by using radio frequency direct driving of the ground-state qubit to perform dynamical decoupling, we can hope to extend its coherence time far beyond what has previously been achieved in our system and indeed any other ion-cavity system that we are aware of.

[1] Measured as an average from clock operation between 13.12.2022 and 28.02.2023. The error corresponds to the standard deviation.

This chapter presents the integration of a direct $|S\rangle$ - $|S'\rangle$ RF drive into the existing experimental setup. Section 5.1 introduces the hardware of the implementation. First, the electronic drive circuit is discussed before giving more details on the RF-antenna. Sections 5.2.1, 5.2.2 and 5.2.3 present a series of experiments that characterise the RF drive's performance using a single trapped ion. Experiments for investigating problems and limitations of the RF drive are discussed in Section 5.2.4. Section 5.2.5 presents an application of the direct RF drive in the form of dynamical decoupling experiments, investigating the ground-state qubit's coherence time.

5.1. Setup

5.1.1. Drive circuit

The setup for driving the $^{40}Ca^{+}$ ground-state qubit is based on a previous design made by postdoc Matthias Bock for the 2D-crystals experiment in the group of Christian Roos at the University of Innsbruck. The RF magnetic field is produced by a radio frequency antenna in the form of a coil, mounted in front of our vacuum chamber's CF100 viewport (see Figure 3.2b for the viewport's location at the vacuum chamber). A schematic of the coil's drive circuit is depicted in Figure 5.1.

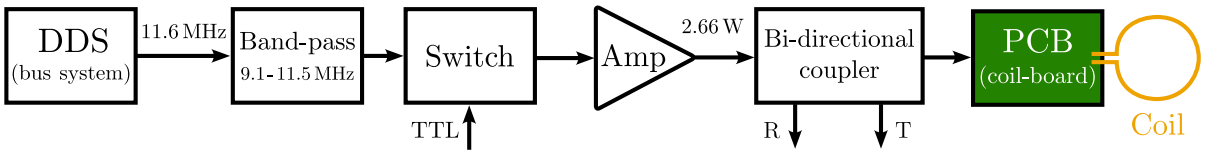

Figure 5.1.: Schematic of the drive circuit for the coil, which produces an RF magnetic field for manipulating the $^{40}Ca^{+}$ ground-state qubit. Component make and model information is provided in the main text and footnotes.

A sinusoidal voltage signal at a frequency around $\nu = 11.6\,\mathrm{MHz}$ is generated by a DDS. The DDS is part of the bus system which is connected to the experiment control software *TrICS* where frequency and amplitude of the DDS output signal can be adjusted. The DDS is free running, meaning that phase control is not possible[2]. The DDS frequency is referenced to a GPS-locked 10 MHz source. At 11.6 MHz, the DDS is operated at the edge of its designed frequency range[3], resulting in its output signal spectrum showing peaks at higher harmonics. Sending the DDS output through a band-pass filter[4] with a pass-band between 9.5 MHz and 11.5 MHz reduced these undesired peaks at higher frequencies by at

[2]For the dynamical decoupling experiments in Section 5.2.5, a different DDS, located at the Pulse Box, was used for which phase control is available.
[3]Normally, DDS devices in the laboratory are used for driving AOMs at a frequency of a few hundred megahertz.
[4]Mini-Circuits BBP-10.7+

least 20 dB. Pulses of the RF signal are generated by a TTL-controlled switch[5]. The rise time of the switch was measured to be 8.5(5) ns. The output power of the DDS is on the order of a few milliwatts. To drive the antenna with a power in the single Watt regime, an amplifier[6] with a measured gain of approximately 32 dB is used. The parameter in TrICS for setting the output power of the DDS relates to the real output power only on an arbitrary scale. A calibration of the output power, both at the band-pass filter output and at the amplifier output, was carried out with a powermeter[7]. The two calibration curves are shown in Figure 5.2a. On a decibel scale, the amplifier's gain is the difference between both calibration curves. The gain was found to decrease rapidly for an amplifier input power higher than 1.9 mW, which is shown in Figure 5.2b. For all experiments that were carried out, the input power was never set higher than 1.9 mW, giving an amplifier output power of 2.66 W.

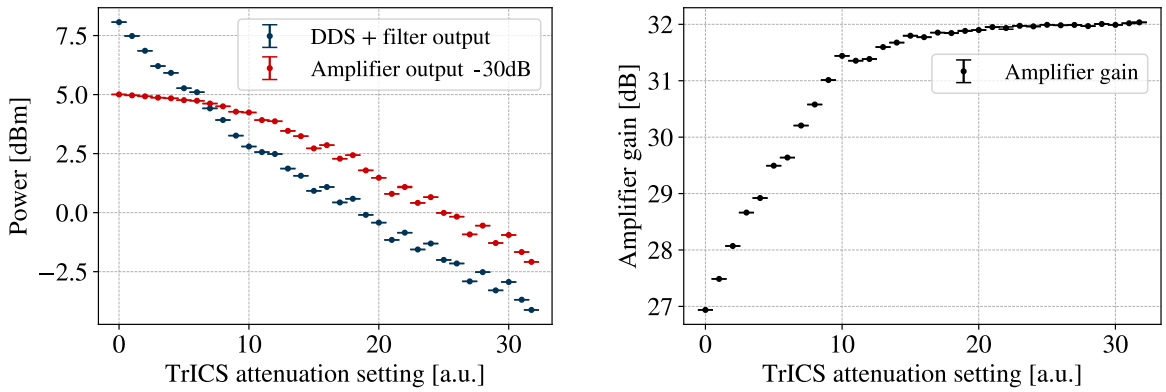

(a) **(b)**

Figure 5.2.: a) Calibration curves of the RF signal power in dependence of the arbitrary scaled attenuation parameter in the experiment control software (TrICS). Curves are recorded for the output of the band-pass filter (blue) and the amplifier output (red). For measuring the amplifier's output power, the signal was attenuated by 30 dB. Fluctuations between neighbouring data points were reproducible. **b)** The amplifier's gain is the ratio between amplifier and filter output power (difference on a decibel scale). The gain decreases for attenuation parameter values below approximately 10 which is equivalent to an amplifier input power higher than 2.8 dBm = 1.9 mW and an amplifier output power higher than 2.66 W.

The homemade antenna is part of a resonance circuit, soldered onto a printed circuit board (PCB) that was produced by MultiCB, which is is referred to as the *coil-board* during this chapter. Possible RF reflection happening at the interface to the coil-board is handled by a bi-directional coupler[8]. The bi-directional coupler provides pickoff signals

[5]Mini-Circuits ZASWA-2-50DRA+
[6]Mini-Circuits ZHL-1-2W-S+
[7]Mini-Circuits PWR-SEN-4GHS
[8]Mini-Circuits ZFBDC20-61HP-S+

in the transmission and reflection direction with a 1% power pickoff ratio. The reflection pickoff can be connected to a spectrum analyser to measure and display the coil-board's amplitude transfer function. Otherwise, both pickoff output ports are terminated by 50 Ω resistors.

5.1.2. RF-antenna

Coil-board

The RF-antenna has the form of a coil such that it generates a magnetic field that can be described using the model of the Biot-Savart law presented in Section 2.4.3. The RLC resonance circuit, formed by the coil's intrinsic capacitance, inductance and resistance, has a resonance frequency that is significantly higher than the envisioned drive frequency of 11.6 MHz. Connecting the coil directly to the amplifier output would therefore drive the coil strongly off-resonant, leading to almost no current flowing through it. Consequently almost no magnetic field would be produced. To maximise the current in the coil, an external capacitance is added in series to the coil which shifts the resonance frequency to the desired drive frequency of around 11.6 MHz. Further, an external ohmic resistance is added in series to the coil's intrinsic resistance to increase the bandwidth of the RLC resonance circuit. The RLC resonance circuit formed by the coil's inductance, the external capacitance and the total ohmic resistance then has a resonance frequency that matches the expected atomic transition frequency and filters out off-resonant signals. At its resonance frequency, the RLC circuit has an impedance deviating from the standardised 50 Ω in the rest of the coil's drive circuit. To avoid RF reflection and therefore maximise the signal power in the resonance circuit, an L-type impedance matching circuit as discussed in Section 2.4.2 is added. Both the resonance- and impedance matching circuit are implemented on the coil-board. The circuit diagram is shown in Figure 5.3a and a photograph of the coil is shown in Figure 5.3b.

The coil-board features multiple solder pads for discrete-valued surface mount components (SMC) in series and parallel arrangements. The arrangements allow for constructing each of the capacitances and inductances indicated in Figure 5.3a out of multiple components, consequently making C_{res}, C_{IM} and L_{IM} tunable by changing components. Parallel capacitances and series inductances add up while series capacitances and parallel inductances add in their inverses. The resistance R_{res} is the sum of the coil resistance R_{coil} and an additional resistor R_0. For the resistor R_0 there only exists a single SMC solder pad but stacking multiple SMC resistors on top of each other (parallel connection) provides fine tuning between otherwise discrete resistance values. A photograph of the coil-board with labels and indicated component values can be found in Appendix A.2. The input signal to the circuit in Figure 5.3a can be applied through two different BNC ports. One of the ports has the option of placing a transformer into the signal chain for galvanic isolation. For the results presented in this thesis, only the other directly-connected port was used.

Further, in the implementation presented in this thesis, the capacitor in the resonance circuit C_{res} is much smaller than the impedance matching capacitor C_{IM}. The voltages at C_{res} are therefore significantly higher than at C_{IM}. The used components for C_{res} are rated to withstand up to 3 kV.

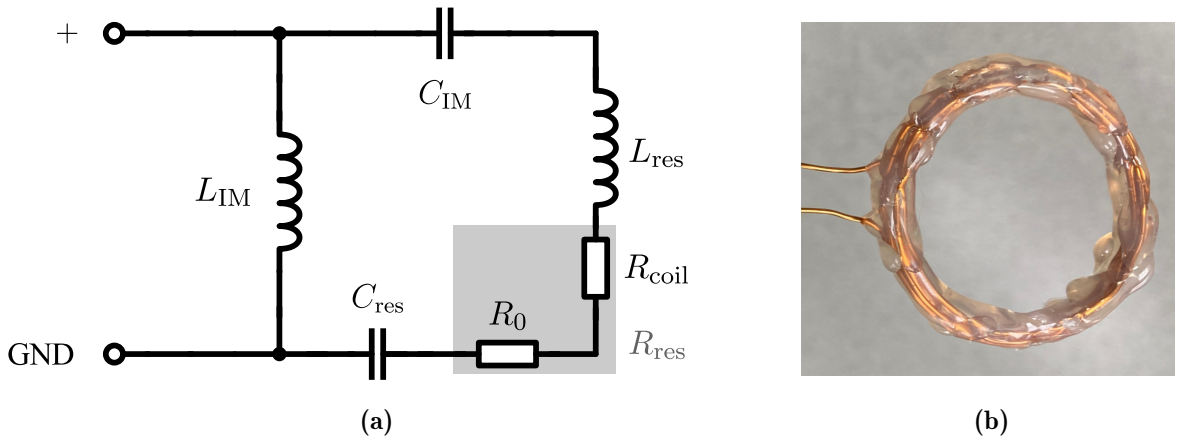

Figure 5.3.: a) Circuit diagram of the coil-board from Figure 5.1. An RLC resonance circuit is formed by the coil inductance L_{res} together with a capacitance C_{res} and a resistance R_{res}. The resistance R_{res} includes both the coil's resistance R_{coil} and the additional resistor R_0. Impedance matching is achieved by an L-shaped junction with a capacitance C_{IM} in series with the RLC part and an inductance L_{IM} parallel to the RLC part. **b)** Photograph of the coil. The coil has $N = 5$ windings which are glued together for keeping the inductance stable against vibrations. The coil's radius is $R = 2.0(3)$ cm.

RF-coil

The coil is made out of copper wire with a diameter of 0.85 mm. Five windings with an overall radius of $R = 2.0(3)$ cm result in an inductance of $L_{\mathrm{IM}} = 2.5(7)$ µH, calculated by Equation 2.73. Measuring the coil inductance with an LCR-meter[9] yielded $L_{\mathrm{res}} = 2.1(1)$ µH. Based on the measured coil inductance, the capacitance for achieving a resonance frequency of 11.623(5) MHz is predicted, using Equation 2.60, to be C_{res}=89(4) pF. Windings of the coil are glued together to avoid vibrations affecting the coil's geometry and therefore its inductance. When mounting the coil-board with the coil attached at its position in front of the vacuum chamber's CF100 viewport, the chosen coil radius of roughly half the viewport's radius provides flexibility to adjust the position of the coil. The coil axis is angled at roughly 45° with respect to the quantisation magnetic field that is provided by a pair of permanent magnet coils.

[9] PeakTech 2155 LCR-/ESR-Multimeter

Optimisation procedure for components on the coil-board

Components on the coil-board for both the resonance circuit and impedance matching were optimised by hand in multiple iterations. In each iteration the spectrum of the coil-board's reflected signal was measured with a network analyser. The spectrum of the coil-board's reflected signal is expected to show a dip in amplitude at the circuit's resonance. From the spectrum, the coil-board circuit's resonance frequency, quality factor and reflection losses are extracted. Optimisation of the reflection spectrum aimed at less than $-20\,\mathrm{dB}$ reflected power at a resonance frequency of $11.595\,\mathrm{MHz}$[10] and a quality factor of $Q \approx 15$. This value of the quality factor was chosen as a compromise between maximising the coil current and achieving a bandwidth that is significantly bigger than typical drifts of the ground-state qubit's transition frequency. Changes of the external magnetic field, experienced by the ion, will shift the transition frequency of the ground-state qubit. The ambient magnetic field showed fluctuations with peak-to-peak differences on the order of a few milligauss during approximately three months. These peak-to-peak differences of the ambient magnetic field translate to changes in the ground-state qubit's transition frequency which are on the order of a few kilohertz. For a quality factor of $Q \approx 15$, the resonance has a full-width-half-maximum on the order of several hundreds of kilohertz and adjusting the drive frequency to the atomic resonance does not significantly reduce the RF power that is delivered to the coil-board. Having said that, when bringing the coil close to metallic surfaces like the vacuum chamber, changes in the coil inductance were observed, causing the resonance frequency of the coil-board circuit to shift significantly. Having the coil a few centimetres away from the CF100 viewport caused a shift of $244(1)\,\mathrm{kHz}$ compared to the case where the coil is at least on the order of ten centimetres away from any surfaces. To account for this shift, the resonance frequency of the circuit was optimised by choice of components to be $244(1)\,\mathrm{kHz}$ below the predicted atomic resonance. Consequently, when mounting the coil in front of the vacuum chamber, the coil-board circuit's resonance then matches the atomic transition frequency.

Optimisation of resonance frequency, quality factor and reflection losses was performed in the following steps. First, the coil was connected to the coil-board, R_0 was shorted and impedance matching was turned off by shorting (keeping open) the capacitance C_{IM} (inductance L_{IM}). Second, the resonance circuit's capacitance C_{res} was optimised to match the desired resonance frequency. In cases where no dip in the reflection spectrum was visible, the resistor R_0 was set to a few tens of Ohms, which lead to a reflection dip of a few decibels. My interpretation of this observation is that with shorted resistor R_0, giving $R_{\mathrm{res}} = R_{\mathrm{coil}}$, the quality factor is very high, making the resonance unstable. In the next step,

[10] This value differs from the previously-reported value of $11.623\,\mathrm{MHz}$ by $28\,\mathrm{kHz}$. The value of $11.595\,\mathrm{MHz}$ was predicted by Equation 2.35 from a separate measurement of the ambient magnetic field strength (clock operation) during a shorter time interval of only a few hours. As the coil-board circuit's bandwidth of several hundreds of kilohertz is much larger than this deviation, no significant reduction of RF power is expected when driving the coil-board's circuit at the correct atomic resonance frequency.

after having matched the desired resonance frequency, the resistance R_{res} was optimised for a quality factor close to $Q = 15$ by tuning the resistor R_0 with discrete SMC resistors, stacked upon each other in parallel connection.

In the final optimisation step, the coil-board's reflection losses were minimised by impedance matching. For that, first the resistance R_{res} was calculated from the previously measured quality factor by rearranging Equation 2.61. The obtained value of R_{res} was then used to calculate C_{IM} and L_{IM} for impedance matching with Equation 2.65 where the target impedance is $Z_0 = 50\,\Omega$ and the load impedance $Z_{\mathrm{L}} = R_{\mathrm{res}}$ is the resonance circuit's impedance at its resonance frequency. Impedance matching to a target impedance Z_0 lower than the load impedance Z_{L} is not possible with the L-type network on the coil-board as the term inside the square root in Equation 2.65 becomes negative. The case $Z_0 < Z_{\mathrm{L}}$ can emerge from a coil with increased size, and therefore increased resistance R_{coil}. For impedance matching to $Z_0 < Z_{\mathrm{L}}$, a matching circuit with different geometry has to be built. In the normal case of $R_{\mathrm{res}} < 50\,\Omega$, the components C_{IM} and L_{IM} were optimised to deepen the reflection dip in the spectrum, starting with the values obtained from Equation 2.65. Changing the inductance L_{IM} showed a big influence on the reflection dip level but also shifted the reflection dip's centre frequency. Changing the capacitance C_{IM} proved to counteract the frequency shift without significant changes in the depth of the reflection dip.

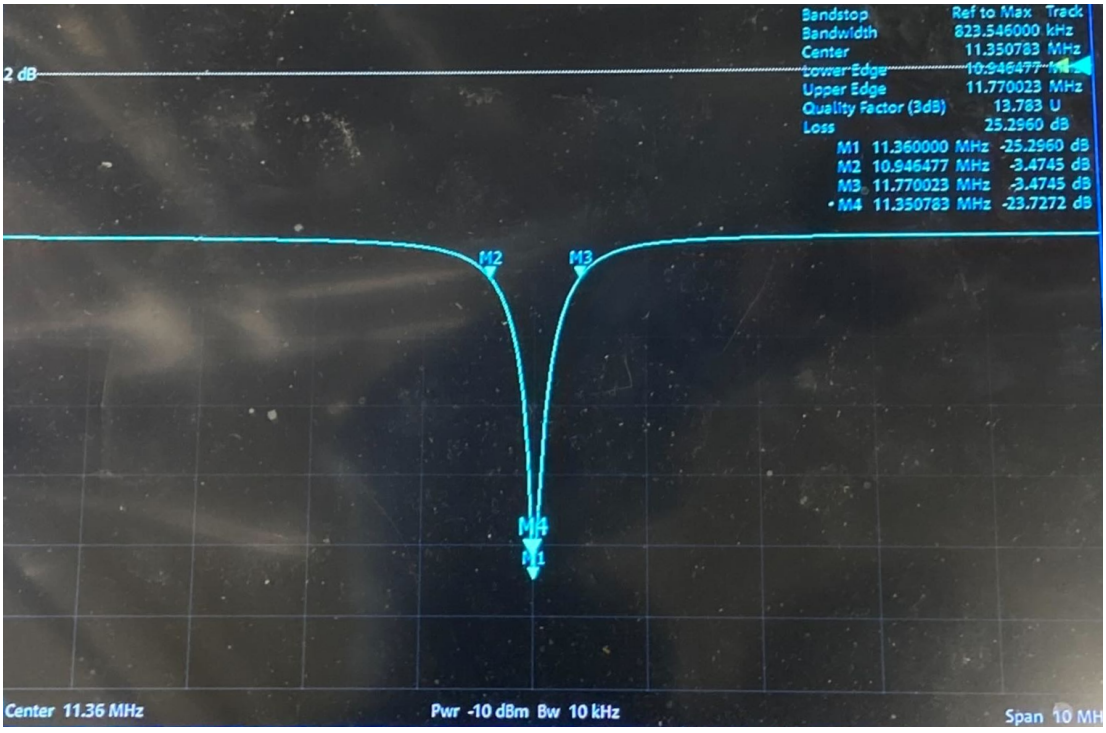

Figure 5.4.: Photograph of the coil-board's reflection spectrum recorded with a network analyser. Components on the coil-board were optimised following the process described in this section. The spectrum was taken with the coil being on the order of ten centimetres away from any surfaces. The values of resonance frequency, bandwidth, quality factor and reflection level are given in the main text.

Through several iterations of changing C_{IM} and L_{IM}, a configuration was found which produced the reflection spectrum in Figure 5.4. With the coil on the order of ten centimetres away from any surfaces, a resonance frequency of 11.351 MHz was reached with a bandwidth (full-width-half-maximum) of 824 kHz, giving $Q = 13.8$. The dip in the reflection spectrum goes down to -25.3 dB, meaning that 0.3% of the signal power gets reflected when entering the coil-board. Bringing the coil into its proposed position a few centimetres away from the vacuum chamber's CF100 viewport shifted the resonance frequency to 11.595 MHz without significant changes of the reflection losses and the quality factor. The mismatch of 28 kHz to the predicted atomic resonance at 11.623 MHz is much smaller than the coil-board circuit's bandwidth. Therefore, the RF power entering the coil-board is not expected to change significantly when driving the coil-board slightly off-resonant, but on resonance with the atomic transition. Still, the coil-board's resonance frequency can be fine-tuned towards the atomic resonance by slight adjustments of the coil position.

5.2. Experiments and results

This section presents experiments in which the RF-antenna (coil) is used to drive the $|S\rangle$ to $|S'\rangle$ transition in $^{40}Ca^{+}$. For some of these experiments, changes are made to the setup that was introduced in Section 5.1 and such changes are indicated in the corresponding sections. During experiments that involved measurements with a single ion, I had assistance from PhD students James Bate and Marco Canteri as well as from postdoc Viktor Krutianskii.

Section 5.2.1 introduces a preparation routine that was carried out before every ion experiment and presents experiments where Rabi flops on the $|S\rangle$ - $|S'\rangle$ ground-state qubit are driven. Section 5.2.2 discusses an attempt to maximise the Rabi frequency of the RF drive. Section 5.2.3 presents experiments where the precision of individual RF pulses is investigated. Limitations that were found in the preceding experiments are discussed in Section 5.2.4. Section 5.2.5 presents experiments which use the RF drive to perform dynamical decoupling on the ground-state qubit.

5.2.1. Preparation and Rabi flops

The coil-board with the coil attached is screwed onto a holder which in turn is clamped onto the optics breadboard that surrounds the vacuum chamber. Parts of the holder are made out of plastic, providing electric isolation to the optics breadboard. The coil is placed in front of the vacuum chamber's CF100 viewport, which has a distance of 10.6 cm to the centre of the ion trap. The coil mount and proximity to the vacuum chamber can be partially seen in Figure 5.6b.

Pulse sequence

For all experiments where the RF drive was used to drive the $|S\rangle$ to $|S'\rangle$ transition, a single ion was loaded into the trap and a pulse sequence of the form shown in Figure 5.5 was used.

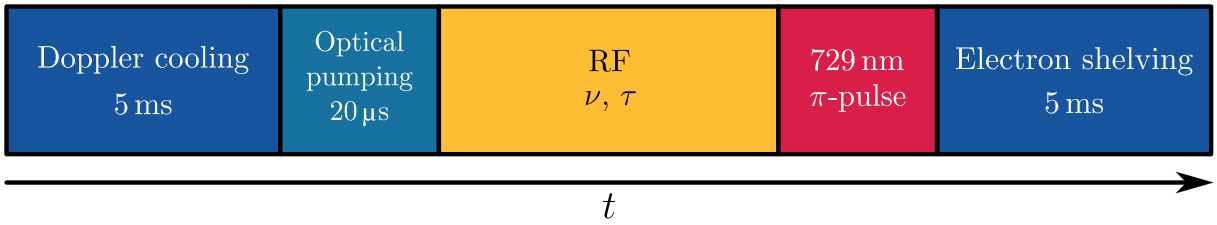

Figure 5.5.: Basic experimental sequence for RF drive experiments involving an ion. The frequency ν and the length τ of an RF pulse can be scanned to obtain spectra or Rabi flops. Durations of Doppler cooling, optical pumping and electron shelving are kept at the indicated values for all experiments in this chapter.

Initialisation consists of 5 ms Doppler cooling, followed by 20 µs of optical pumping such that the ion is prepared in the $4^2S_{1/2,m=-1/2}$ ground-state. The ground-state qubit, encoded into $|S\rangle = 4^2S_{1/2,m=-1/2}$ and $|S'\rangle = 4^2S_{1/2,m=+1/2}$, is then manipulated by RF driving which can consist of a single pulse or multiple pulses. To readout the ground-state qubit by distinguishing the states $|S\rangle$ and $|S'\rangle$, a mapping π-pulse on the optical qubit transition from $|S'\rangle$ to $3^2D_{5/2,m=+3/2}$ is performed. The mapping π-pulse is necessary because the linewidth of the 397 nm $4^2S_{1/2}$ to $4^2P_{1/2}$ transition used for electron shelving is larger than the ground-state qubit's frequency splitting. After the mapping π-pulse, electron shelving is carried out, as described in Section 3.2.1. The mapping pulse renders population in $|S'\rangle$ dark on the camera and the PMT during the final 5 ms of imaging. The durations of all pulses except for RF driving and mapping were kept the same for all experiments in this chapter.

Preparation routine

Before attempting measurements with the RF drive on the ion, a few preparation steps are carried out. First, clock operation as introduced in Section 3.2.3 is performed. Clock operation finds the resonant laser frequencies for optical qubit transitions between different Zeeman-levels and therefore ensures resonant driving for the $|S'\rangle$ to $3^2D_{5/2,m=+3/2}$ mapping pulse. Further, taking the difference between the obtained frequencies of the $|S\rangle$ to $3^2D_{5/2,m=+3/2}$ and $|S'\rangle$ to $3^2D_{5/2,m=+3/2}$ transition gives a first estimate for the $|S\rangle$ - $|S'\rangle$ transition frequency.

In the next step, the length of the 729 nm mapping π-pulse is calibrated. Calibration is done by turning off optical pumping during initialisation and scanning the length of a laser pulse on the $|S'\rangle$ to $3^2D_{5/2,m=+3/2}$ transition. Without pumping, a small population remains in the $|S'\rangle$ state. Rabi flops therefore have only a small amplitude but are sufficient to find a first estimate for the π-time.

Having set the length of the 729 nm mapping-pulse by the obtained π-time, the RF pulse is now included into the sequence. Radio frequency spectroscopy is performed to find the correct RF transition frequency of the ground-state qubit. For that, the frequency of a single RF pulse is scanned around the transition frequency that was predicted by the earlier clock operation. In the case where an expected value of the RF drive's Rabi frequency is known, the RF pulse length is set to be approximately a $\pi/2$-pulse. In the first experiments where the Rabi frequency was still unknown, the length of the RF pulse was set to 1 ms. An example RF spectrum of the ground-state qubit, taken after the Rabi frequency optimisation described below, is shown in Figure 5.6a. Fitting the spectrum's excitation data with a Gaussian function gives a centre frequency that is used as the RF drive frequency for subsequent measurements. During long data taking sessions, drifts of the transition frequency due to ambient magnetic field drifts need to be measured such that the RF frequency can be updated. Automated feedback to the RF drive frequency from clock operation was only implemented for the experiments in Section 5.2.5. During the experiments in Section 5.2.1, 5.2.2 and 5.2.3, resonant RF driving was ensured by rerecording a spectrum in regular time intervals of tens of minutes and updating the RF drive frequency accordingly.

Having found the resonance frequency of the $|S\rangle$ - $|S'\rangle$ transition, Rabi flops are recorded by scanning the length of the RF pulse. A first estimate of the Rabi frequency and π-time is extracted from the resulting data. It is likely that the amplitude of Rabi flops is not maximised yet. A more precise calibration of the mapping π-pulse duration is therefore performed now, not relying on the absence of optical pumping, but using an approximate RF π-pulse to achieve high probability of preparing the state $|S'\rangle$. Using the remeasured π-time for the mapping 729 nm pulse then should produce RF Rabi flops with near unit contrast.

Maximising the Rabi frequency

A series of experiments was carried out, aimed at increasing the Rabi frequency of $|S\rangle$ - $|S'\rangle$ Rabi flops with the RF drive. In the first instance, the coil was placed at a distance of 4(1) cm from and with its axis perpendicular to the CF100 viewport's surface. With the coil being centred with respect to the viewport, called the *on-axis* position in further discussions, the first observed Rabi flops had a π-time of 3 ms for 1.87 W of RF power at the amplifier output. With the coil in the on-axis position, the RF magnetic field produced by the coil at the ion position is angled at $\alpha = 45(11)^\circ$ with respect to the quantisation field, produced by the permanent magnets. Only the component of the RF field that is perpendicular to the quantisation field can drive the $|S\rangle$ to $|S'\rangle$ magnetic dipole transition. The RF field strength perpendicular to the quantisation field scales with $\cos(\alpha)$.

Steps for maximising the Rabi frequency by adjusting the coil position are indicated in Figure 5.6b, showing the coil in its final position. First, the coil was moved closer to the viewport, which gave only a marginal gain in Rabi frequency. The Rabi frequency was

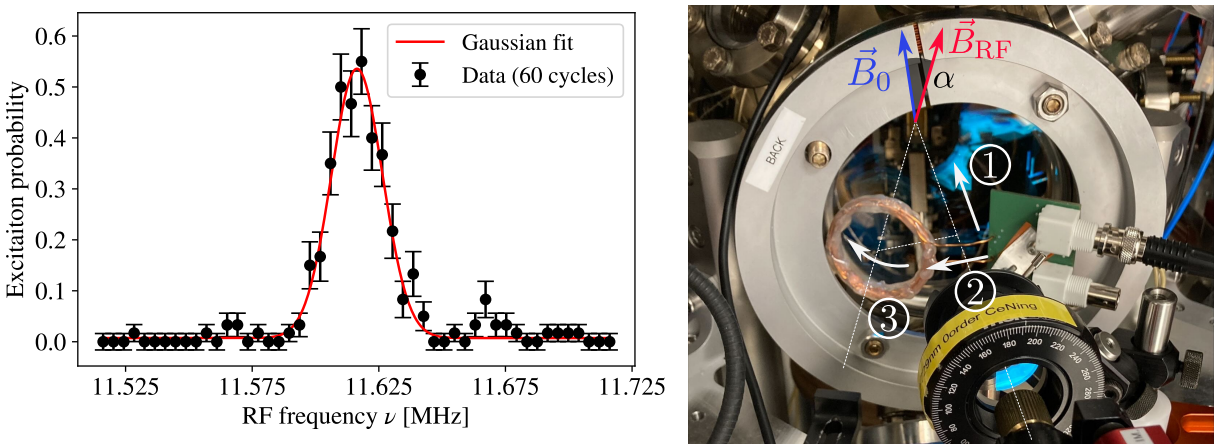

(a) **(b)**

Figure 5.6.: a) Radio frequency spectrum on the ground-state qubit transition recorded with a 30 µs long RF pulse on a single ion. A Gaussian least squares fit on the peak gives a centre frequency of 11.6164(5) MHz and a full-width-half-maximum of 23.8(9) kHz. **b)** Positioning of the coil at the vacuum chamber's CF100 viewport. The white arrows indicate moving directions for maximising the Rabi frequency (AC magnetic field strength at the ion position). The coil was placed as close as possible to the CF100 viewport (1). Moving the coil to an off-axis position (2) was found to give the largest improvement in Rabi frequency. Finally, the coil was tilted such that its axis points towards the ion trap (3). The coil's RF field $\vec{B}_{\mathrm{RF}}$ (red vector) is orientated at an angle $\alpha = 48(10)^\circ$ with respect to the quantisation field $\vec{B}_0$ (blue vector).

then greatly improved by displacing the coil from the viewport centre in radial direction, referred to as the *off-axis* position from now on. Finally, the coil was also tilted such that its axis points towards the ion trap. In the final position shown in Figure 5.6b, the coil wire is less than a centimetre away from the viewport, almost touching it with one side. In this final position, the coil's RF field at the ion position is angled at $\alpha = 48(10)^\circ$ with respect to the quantisation field. No significant difference of the angle α is found when comparing the on-axis and off-axis position of the coil. Therefore, the observed strong increase of the Rabi frequency at the off-axis position is not expected to be caused by the change of the angle α. A strong increase in Rabi frequency at the off-axis position is possibly explained by a reduction of induced currents in the viewport's circular metal structure.

When adjusting the coil's position, one should keep in mind that the coil-board's resonance shifts in dependence of the coil's distance to the metallic surfaces of the chamber. At the time of searching for the best coil position, the RF power was also increased to 2.66 W at the amplifier output, corresponding to 2.63 W at the bi-directional coupler's output going to the coil-board.

Time evolution of Rabi flops

With an RF power of 2.63 W being sent to the coil-board and with the optimised coil position in Figure 5.6b, $|S\rangle$ - $|S'\rangle$ Rabi flops were recorded in multiple segments of the RF pulse length τ. Each segment was measured by an individual scan of the RF pulse length. All segments had a length of at least 1 ms, covering multiple flops, but had different offsets in the RF pulse length, ranging from 0 ms to 80 ms. For each segment, Rabi flops are fitted (least squares) with a function $p(\tau) = 1/2 - A/2 \cdot \cos(\pi/t_\pi \cdot \tau)$, extracting the amplitude A and the π-time t_π. Rabi flops from two segments, with offsets of 0 ms and 50 ms are shown in Figure 5.7. In the segment with an offset of 0 ms, the sinusoidal fit yields an amplitude of $A = 0.99(1)$ and a π-time of $t_\pi = 57.89(4)$ µs, corresponding to a Rabi frequency of $\Omega = 2\pi \cdot 8.637(6)$ kHz. In the segment with an offset of 50 ms, the sinusoidal fit yields an amplitude of $A = 0.68(5)$ and a π-time of $t_\pi = 54.971(2)$ µs. In the segment at 50 ms, Rabi oscillations were visible only after the first six data points. These first data points are cut out in Figure 5.7 and will be discussed in Section 5.2.2.

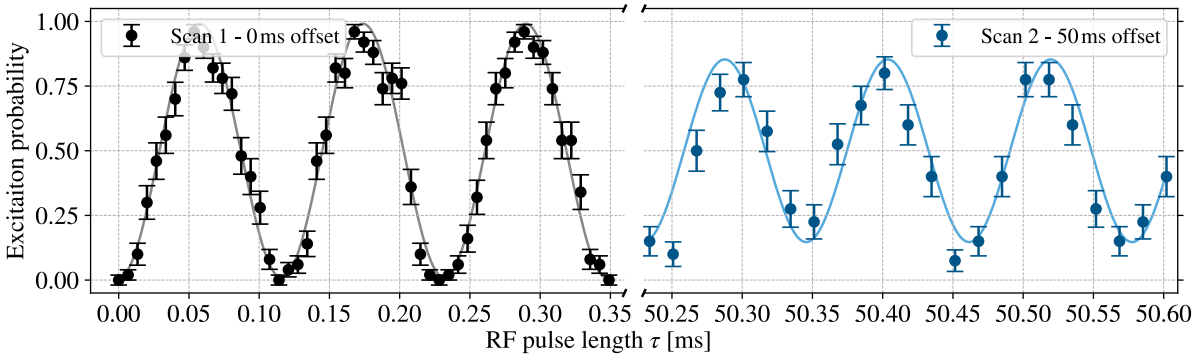

Figure 5.7.: Rabi flops on the $|S\rangle$ - $|S'\rangle$ ground-state qubit driven with an RF signal from the coil. The two segments starting at 0 ms (black data points) and 50 ms (blue data points) were recorded in two separate scans. The solid lines are sinusoidal fit-functions as described in the main text. For better visibility and due to issues discussed in Section 5.2.2, only a subset of data points in each of the two segments, covering three flops each, is plotted.

When comparing Rabi flops in a segment with an offset in the RF pulse length to the first segment at 0 ms (no offset), significant differences are found in both parameters of the sinusoidal fits. The evolution of the fit parameters, amplitude A and π-time t_π, with increasing pulse length offsets of the segments is shown in Figure 5.8.

The amplitude values of the Rabi flops shown in Figure 5.8 are fitted (least squares) with a linear function $A(\tau) = A_0 \cdot (1 - 1/2 \cdot \tau/\tau_{1/2})$. The amplitude decreases to half its initial value $A_0 = 0.99(1)$ after $\tau_{1/2} = 93(5)$ ms of continuous RF driving. Amplitude damping of the Rabi flops most likely comes from ambient magnetic field noise on timescales comparable to the duration of experimental sequences. The π-time shortens by 2.89(4) µs to 55.001(3) µs during the first 10 ms of RF driving, which is a relative change of 5.0(1)%. Between 10 ms and 50 ms, the π-time only varies by 0.030(3) µs peak to peak. From 50 ms

to 80 ms, the π-time increases by 1.008(2) µs. Therefore, the main change in π-time happens during the first 10 ms of RF driving. An investigation and discussion of the changing π-times (Rabi frequencies) can be found in Section 5.2.4.

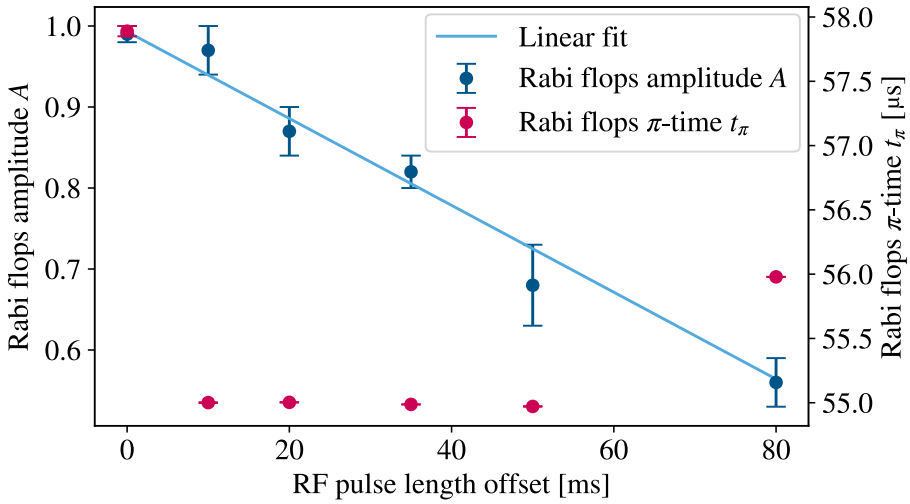

Figure 5.8.: Amplitude (blue) and π-time (red) of $|S\rangle$ - $|S'\rangle$ Rabi flops recorded from multiple segments with increasing offset in the RF pulse length. The data points are extracted fit parameters from Rabi flops in segments where the RF pulse length was scanned in a range of at least 1 ms. For the amplitude, a linear least squares fit is performed (blue line). Information on the fit-function and results are presented in the main text.

5.2.2. Test of a bigger RF-coil

We ideally would like to reach Rabi frequencies on the order of hundreds of kilohertz, corresponding to π-times on the order of microseconds (comparable to laser driving at 729 nm). In order to increase the Rabi frequency to such values, the magnetic field strength at the ion position, generated by the coil, needs to be increased. According to Equation 2.71, the magnetic field strength depends on the distance to the coil, the coil's radius, and the current in the coil, which is related to the RF power. The RF power cannot be increased without entering the non linear gain regime of the amplifier and the distance between coil and trap centre cannot be decreased due to geometrical constraints. The length scale at which the coil's field strength drops off in the axial direction is set by the coil radius. The model predicts that the field strength at the ion's position can be increased by using a coil with bigger radius.

A larger coil radius also increases the coil's inductance and for matching the ground-state qubit's transition frequency, capacitances on the picofarad level and below would be needed which are not feasible with the available surface mount components. While the inductance scales with the square of the number of coil windings N, the field strength only has a linear

dependence on N. Therefore, by reducing N it is possible to retain the coil's inductance value while increasing the field strength with a bigger coil radius. Doubling the coil radius to $R = 4.0(3)\,\mathrm{cm}$ and using $N = 3$ windings (instead of $N = 5$ windings for the smaller radius coil) is predicted (Equation 2.73) to yield an inductance of $L = 2.1(3)\,\mu\mathrm{H}$. The same model predicted an inductance of $2.5(7)\,\mu\mathrm{H}$ for the smaller radius coil. The atomic resonance frequency of $11.625(5)\,\mathrm{MHz}$ is then reached with a capacitance of $C_{\mathrm{res}} = 90(11)\,\mathrm{pF}$, which is feasible with the available SMC capacitors.

A coil with $N = 3$ windings, having an overall radius of $R = 4.0(3)\,\mathrm{cm}$ was built. Additionally, by reducing the resistive losses of the coil-board (increasing the quality factor), the current in the coil was increased. When optimising components on the coil-board with the method described in Section 5.1.2, I aimed for $Q \approx 20$ but reached only $Q = 15.2$ due to the now higher coil resistance R_{coil}. Reflection losses of $-27\,\mathrm{dB}$ were reached. A bigger coil cannot be placed as far off-axis as the initial coil (Figure 5.6b) without hitting the viewport's surrounding metal structure. Compared to the smaller radius coil, higher losses from inductive coupling to the viewport structure are expected.

With the bigger coil, Rabi flops were driven on a single ion. The first four flops during approximately 0.4 ms showed no significant change in contrast compared to the flops driven with the smaller coil (Figure 5.7). The same measurement yielded a π-time of $49.03(7)\,\mu\mathrm{s}$ which compares to the value of $57.85(6)\,\mu\mathrm{s}$ for the smaller coil at the same RF power. The measured π-time with the new bigger coil is reduced by a factor of 1.180(2) in comparison to the smaller coil. This reduction of the π-time is not as strong as intended. It is likely that absorption of the RF field by the viewport and other nearby metallic structures has increased. Furthermore, the problem, of the Rabi frequency changing dynamically as a function of the pulse length, was found to be worse when using the bigger coil. For RF driving of at least a few milliseconds, the first data points of a scan do to not show Rabi flops. The amount of data points after which Rabi flops become visible is dependent on the duration of RF driving and the number of cycles in the scan. The effect of Rabi flops not being visible in the first data points of a scan was already observed when recording the Rabi flops presented in Section 5.2.1, but was omitted there in order to focus on the Rabi frequency and amplitude damping.

The following measurements were carried out in order to investigate the origin of the described dynamic effects: In three repetitions, the length of an RF pulse was scanned from 5.0 ms to 5.4 ms. The second scan was started less than a second after the first one had finished. After the second scan finished, RF driving was completely turned off for approximately 20 s until starting the final scan. The results recorded during the three scans are shown in Figure 5.9. In both cases in which there was no preceding RF driving (first and last scan), Rabi flops only appear after the first approximately 25 data points. The three scans were carried out with 60 cycles for each data point and recording the first 25 points took 27 s in each scan. In the other case, where there was RF signal delivered to the coil immediately after the previous scan (second scan), Rabi flops start immediately with the first data point.

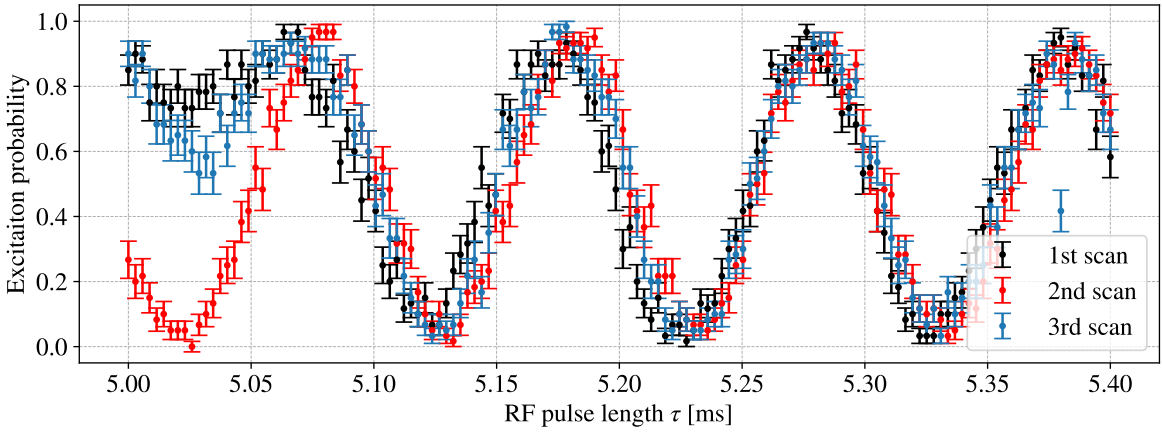

Figure 5.9.: Three repetitions of Rabi flops on the ground-state qubit driven with a bigger RF-coil compared to the one used in Section 5.2.1. The second scan (red) was started less than 1 s after the first scan (black) had finished. Before starting the third scan (blue), the RF drive was turned off for around 20 s. In each scan, recording the first 25 data points took 27 s. The outlier point during the last flop in the blue data points from the 3rd repetition resulted from a background gas collision event.

In the following, a hypothesis is discussed that provides an explanation of the observed dynamic effects. In the hypothesis, heating effects in the coil's drive circuit are considered, affecting the current that is sent through the coil, and consequently the magnetic field strength experienced by the ion, to which the Rabi frequency is proportional. For the first and third scan, the drive circuit would be initially in a "cold" state. During the time of recording the first 25 data points of these scans, taking 27 s, the drive circuit would heat up and the Rabi frequency would change significantly in between individual cycles. A single data point would therefore be an average out of cycles with different Rabi frequencies, preventing visible Rabi flops. After several cycles and data points, the coil current would eventually reach a stable "hot" equilibrium state and the Rabi frequency would stay constant for all cycles that contribute to a single data point. Starting the scan again directly afterwards would already have the drive circuit in the "hot" equilibrium state, making Rabi flops visible. Heating could be caused by power dissipation due to various ohmic resistances in the coil's drive circuit. Also the coil itself is, due to its ohmic resistance, expected to dissipate power and cause heating. With the higher ohmic resistance of the bigger coil, power dissipation and consequently heating are expected to be stronger. In the case of the smaller coil where heating is reduced, changes of the Rabi frequency during all cycles for a single data point could become negligible, however throughout multiple data points of a scan, the Rabi frequency could still change. In that case, the π-time of Rabi flops would change with the duration of driving, as observed in the experiments presented in Section 5.2.1. Further tests of the described hypothesis were performed in separate experiments and are discussed in Section 5.2.4.

The observed stronger dynamic effects on Rabi flops were the basis for our decision to go back to the smaller coil for all future experiments reported in this thesis. Rabi flops are not much slower with the smaller coil, but suffer significantly less from drifting Rabi frequencies.

5.2.3. Precision of RF pulses

The coil with the smaller radius was mounted again as close as possible to the position for a maximised Rabi frequency that was found in the experiments in Section 5.2.1. Rabi flops were measured again with a slightly longer π-time of 60.69(8) µs, extracted from the first four flops with a least squares fit. Maximum excitation probabilities of 0.996(2) were reached during the first four flops.

The precision of single qubit rotations, in particular π-pulses, performed with the RF drive was investigated. For these measurements the sequence from Figure 5.5 is altered by increasing the number of RF pulses from one to N_P, where all pulses have the same duration τ. For different numbers of RF pulses N_P, their length τ is scanned around the π-time that was obtained during Rabi flops, as shown in Figure 5.10.

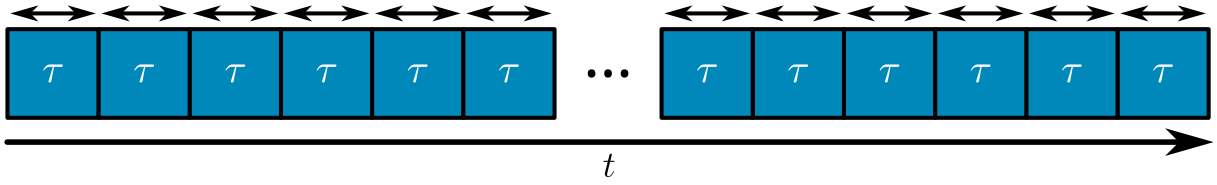

Figure 5.10.: Sequence of RF pulses for testing the precision of π-pulses. The pulse duration τ is varied around the π-time t_π.

Scanning the length τ of an even number of pulses around $\tau = t_\pi$ is expected to produce a minimum in excitation probability close to $p = 0$. The error for such low excitation probabilities is set by the rule of succession from Equation 3.4. Scans of the pulse length τ at $N_\mathrm{P} = 10$, $N_\mathrm{P} = 20$ and $N_\mathrm{P} = 40$ RF pulses were carried out and repeated at least three times. The repetitions were averaged to individual data sets with up to 480 cycles per data point[11]. The combined data from each setting of N_P is shown in Figure 5.11.

For each setting of N_P, the data in Figure 5.11 is fitted (least squares) with a quadratic function $p(\tau) = a \cdot (\tau - t_\pi)^2 + p_\mathrm{min}$. The fit gives the optimum π-time t_π which achieves minimum excitation probability p_min. The evolution of these two parameters when increasing the number of pulses N_P is shown in Figure 5.12.

The data in Figure 5.12a is fitted (least squares) with a linear function of the form $t_\pi(N_\mathrm{P}) = -a \cdot N_\mathrm{P} + b$. The pulse length for minimum excitation decreases by $a = 10.7(1)$ ns per pulse from an initial value of $b = 60.214(2)$ µs, showing again that the π-time (Rabi

[11] The scans with $N_\mathrm{P} = 40$ (red data points in Figure 5.11) had different ranges of pulse lengths, preventing averaging of data points. In this case, all three data sets were combined directly, giving bigger error bars but more data points.

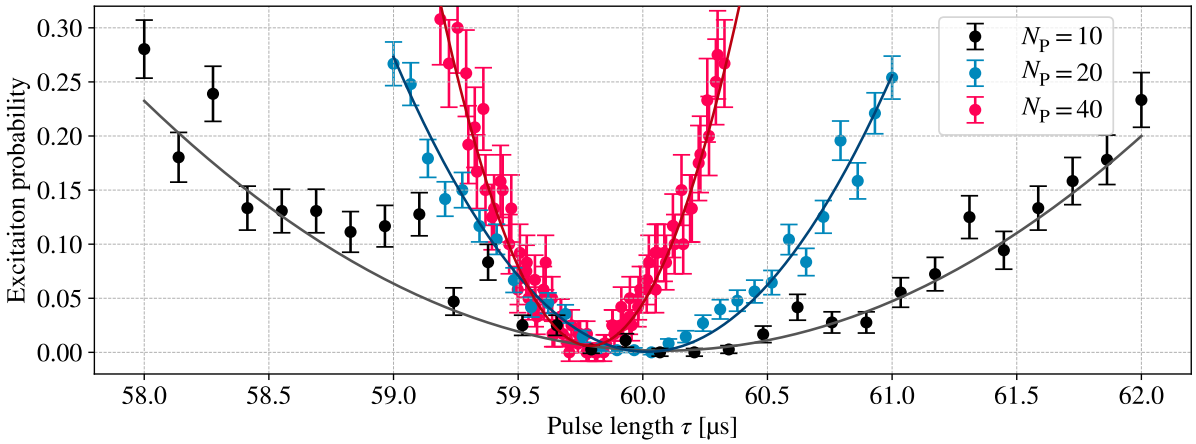

Figure 5.11.: Comparison of the excitation probability after $N_P = 10$ (black), $N_P = 20$ (blue) and $N_P = 40$ (red) pulses as a function of their pulse length τ, which was varied around the π-time. A minimum in excitation probability is expected for even numbers of pulses N_P. Quadratic least squares fits (solid lines) extract the pulse lengths t_π for minimum excitation probability $p_{\min}$ as described in the main text. The pulse sequence becomes increasingly sensitive to changes of the pulse length for minimum excitation when increasing the number of pulses N_P. The pulse length for minimum excitation decreases when increasing the pulse number N_P.

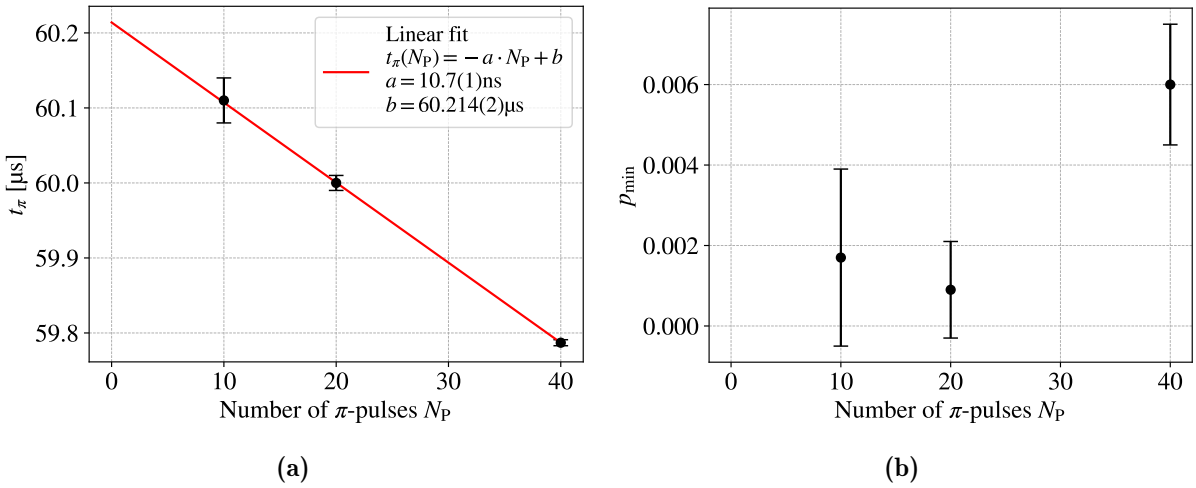

(a) **(b)**

Figure 5.12.: Evolution of the pulse length for minimum excitation t_π **(a)** and the minimum excitation $p_{\min}$ **(b)** after N_P pulses. The data points stem from fit parameters extracted from the data in Figure 5.11. The solid red line is a linear least squares fit.

frequency) changes over the duration of RF driving. The value of b is significantly smaller than the initially obtained π-time from the first four Rabi flops of 60.69(8) µs. It is not clear where this discrepancy comes from. To verify a non linear evolution of the optimum π-time, the experiment has to be repeated, probing more settings of N_P.

The minimum excitation probability $p_{\min}$ does not show a significant change during the first $N_P = 20$ pulses. Between $N_P = 20$ and $N_P = 40$ pulses, the minimum excitation

probability increases by $\Delta p_{\min} = 0.005(2)$ to $p_{\min} = 0.0060(15)$. This change in the minimum excitation probability deviates by 2.5 standard deviations from the case $\Delta p_{\min} = 0$ and is considered to be significant. It is not clear what the origin of the increase in the minimum excitation probability is.

The following numerical calculation was carried out in order to compare the measured changes of the minimum excitation probability (Figure 5.12b) to the change of the excitation probability that is caused by the measured change of the π-time (Figure 5.12a). Based on the model of Rabi flops in Equation 2.53, the excitation probability change after a single pulse with fixed length, when changing the the π-time, was calculated. The calculation yielded that at a pulse length of $N_{\mathrm{P}} \cdot b = 40 \cdot 60.214\,\mu\mathrm{s} = 2.408\,\mathrm{ms}$, the excitation probability changes from $p = 0$ to $p = 0.188(4)$ when changing the π-time from $60.214\,\mu\mathrm{s}$ to $59.7871(43)\,\mu\mathrm{s}$ which is the measured π-time change shown in Figure 5.12a. Such a change in excitation probability, caused by a changing π-time (Rabi frequency), is significantly bigger than the measured increase of the minimum excitation probability in Figure 5.12b to $p_{\min} = 0.0060(15)$. I conclude that the precision of RF pulses is mainly limited by dynamically changing Rabi frequencies during the pulse sequence.

5.2.4. Further investigation into system limitations

Investigating drifts of the Rabi frequency

During the measurements presented in the previous sections, drifts in the Rabi frequency were observed. In order to understand the origin of these drifts, further measurements were carried out. The starting point was a dummy scan, recording the ion's excitation to the $|S'\rangle$ state after a 50 ms long RF pulse (initial state $|S\rangle$). The results of this measurement are presented in Figure 5.13a. The scan took a total time of 505 s and each data point, involving 40 cycles, took 2.5 s to obtain. The excitation probability first dropped from 0.5 to approximately 0.1 during 8 s, then increased to around 0.9 during 497 s. By a numerical calculation (illustrated in Figure 5.13b) it was found that such a drift could be caused by a change in π-time from originally $60.000\,\mu\mathrm{s}$ to $59.957\,\mu\mathrm{s}$ which is a fractional change of $7.2 \cdot 10^{-4}$.

The Rabi frequency Ω scales with the square root of the RF power P_{coil} that is delivered to the coil. From Gaussian error propagation it follows that a fractional change in RF power $\Delta P_{\mathrm{coil}}/P_{\mathrm{coil}}$ is halved when translating it to a Rabi frequency or π-time as

$$\left|\frac{\Delta\Omega}{\Omega}\right| = \left|\frac{\Delta t_\pi}{t_\pi}\right| = \frac{1}{2}\left|\frac{\Delta P_{\mathrm{coil}}}{P_{\mathrm{coil}}}\right|. \tag{5.1}$$

To cause the change in Rabi frequency associated with the measured excitation drift in Figure 5.13a, the RF power has to show fractional changes of $1.4 \cdot 10^{-3}$.

The stability of the RF power that is delivered to the coil was measured by recording time traces of the power at the amplifier output and the bi-directional coupler's reflection pickoff

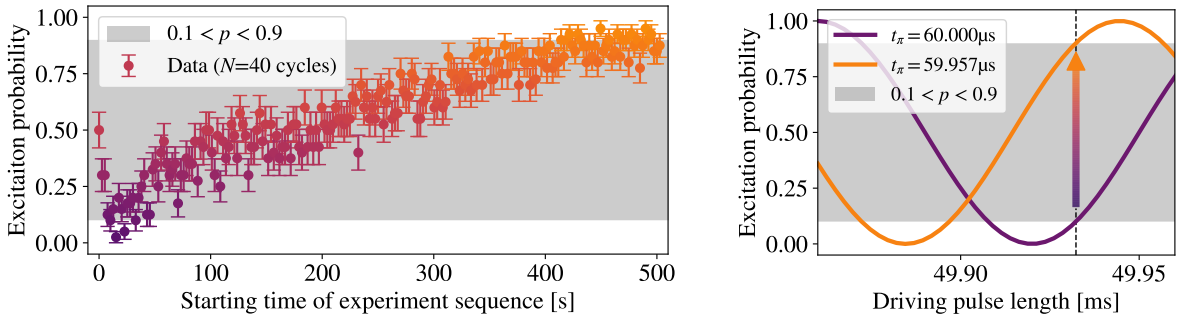

(a) **(b)**

Figure 5.13.: a) Excitation probability in $|S'\rangle$ after a 50 ms long RF pulse in a dummy scan. During 497 s the excitation probability increased from around $p_1 = 0.1$ to $p_2 = 0.9$. **b)** Numerical simulation of Rabi flops for two different Rabi frequencies (and corresponding π-times as labelled in the legend) at a pulse length close to 50 ms. At the driving pulse length where, with the original π-time of 60 µs, an excitation probability of 0.1 is reached, decreasing the π-time by 43 ns increases the excitation probability to 0.9. In both panels, colors of data points and curves indicate different Rabi frequencies.

output using an RF powermeter[12]. The time traces were recorded from continuous RF signals. During 30 min after switching the continuous RF signal on, the power delivered the coil increased from 2.559(1) W to 2.592(1) W, which is a fractional change of $1.25(8) \cdot 10^{-2}$. Details, showing how the power drift at the coil is a combination of changes in the amplifier output power and the power reflected from the coil-board, can be found in Appendix B.4. The power drift at the coil was found to be mainly caused by a power drift at the amplifier output. The measured change in the power that is delivered to the coil is significantly larger than the estimated power change for causing the excitation drift in Figure 5.13a. However, there are two differences between these experiments that likely explain their mismatch in the power change. These differences are discussed in the following.

First, the two measurements have different timescales. The direct RF power drift measurement took 30 minutes, covering the complete evolution to a new stable value (Appendix B.4), while measuring the ion's excitation dummy scan took only around eight minutes. The measurement duration for this dummy scan was set such that roughly a full inversion of the excitation probability was covered, which is likely not equal to the duration for reaching the new stable power value. After the excitation dummy scan's duration of 505 s, the directly measured RF power at the coil shows a fractional change of $9.5(7) \cdot 10^{-3}$ which is still bigger than the power change that was estimated from the excitation drift.

The second difference between both measurements is that RF power time traces were recorded from continuous RF signals while the estimation from the excitation drift is based on multiple RF pulses. If the duration of RF operation in an experimental sequence is

[12]Mini-Circuits PWR-SEN-4GHS

comparable to the total sequence length, the average RF power throughout the sequence is approximately equal to the RF power in continuous operation. In the dummy scan experiment that showed the excitation drift, the RF pulse had a length of 50 ms. State preparation and readout only take 10 to 20 ms. Dead times between sequence repetitions occur only when changing pulse sequence parameters for the next data point in a scan. These dead times vary but are typically on the order of milliseconds[13]. Under these conditions, RF pulses only make up approximately half of the sequence duration and power dissipation in the coil and its drive circuit is significantly lower compared to the case of continuous operation.

The timescales of RF power and excitation probability drifts are both on the order of minutes. Further the reversibility of the RF power drift was tested: The coil's drive circuit was first prepared in its "cold" equilibrium state by keeping the RF signal off for several minutes. A continuous RF signal was then applied for several minutes until a new stable power was reached in the "hot" equilibrium state. The RF signal was subsequently switched off and, after a waiting time, switched on again to immediately measure its power. The experiment was repeated with increasing the waiting times, showing the power drifting down again to the initial value in the "cold" equilibrium state. Power drifts are therefore reversible.

The two observed characteristics of the power drift, timescale and reversibility, are typical for temperature effects, suggesting that the origin of the drifting Rabi frequencies is indeed heating in the coil's drive circuit, confirming the hypothesis discussed in Section 5.2.2. Heating is present in particular at the amplifier. In Appendix B.4, it is shown that there are also drifts happening in the power that is reflected from the coil board, presumably due to heating of the coil. However, these drifts are significantly smaller than the power drifts at the amplifier output. The amount of heating in the coil and its drive circuit depends on the specific sequence of pulses being run.

Suggestions for improvements

Heating in the coil and its drive circuit, and consequently drifts of the RF power, are expected to be reduced by lowering the RF power. However, lowering the RF power comes at the cost of reducing the Rabi frequency, which is not desirable. In the following, suggestions for reducing RF power drifts while maintaining the Rabi frequency are presented.

As described in Appendix B.4, the amplifier is responsible for the dominant contribution to the power drift. Running the amplifier constantly in its hot equilibrium state by performing pulse generation after amplification should cancel the amplifier's contribution to the power drift. Electronic switching devices that can operate at the amplifier's output power of several Watts are commercially available but their switching time is rarely below 1 µs [141].

[13] V. Krutianskii, private communication, 25.07.2023

For compensating power drifts originating from a combination of heating at the amplifier and the coil-board, the RF power that is distributed to the coil could be stabilised by a feedback loop that is similar to the one used for stabilising the trap's RF power (as described in detail in Section 4.1.2). For such a feedback loop, the coil-board's reflection signal could be used as a pickoff signal and RF pulses could be generated by a sample-and-hold function.

A different approach is the method of stabilising the area of RF pulses. Pulse area stabilisation with the use of a digital controller was recently implemented for a laser system in the QCosmo experiment, lead by Philipp Schindler. The controller's bandwidth is on the order of hundreds of kilohertz, limited by analogue to digital conversion[14]. To provide stability below the 10^{-4} level for pulse lengths of tens of microseconds, a substantially higher feedback bandwidth would be required.

Motivated by the model of the coil's magnetic field in Section 2.4.3, a valuable option for maintaining Rabi frequencies at lower RF powers (which are expected to reduce heating) is decreasing the distance between the coil and the ion. In our experimental setup, the size of the vacuum chamber sets a limitation to the coil-ion distance. The coil has already been placed with its wire only a few millimetres away from the viewport's surface, having a distance of 12(1) cm to the ion. Reducing the coil-ion distance to 5(1) cm is expected to result in a field strength, and consequently a Rabi frequency, bigger by a factor of 11(2). An off-axis position of the coil with respect to the viewport where it is mounted showed a significant improvement of the field strength experienced by the ion. In order to enable an off-axis position of the coil (comparable to the coil position in Figure 5.6b), in a new vacuum chamber design with reduced ion to viewport distance, the viewport radius should be bigger than the coil radius by at least roughly a factor of two.

Ultimately, when setting up a completely new experimental system, one should aim for an in-vacuum coil. In-vacuum microwave antennas have been implemented previously in neutral atom [142] and trapped-ion experiments [143]. To my current knowledge, trapped-ion experiments have not yet used in-vacuum RF-antennas. A coil placed inside the vacuum chamber can be positioned very close to the ion, although flexibility for changes in the coil's geometry and position is barely given. Another problem is that an in-vacuum coil cannot easily exchange heat with its environment and RF power drifts may become relevant again.

On a final note, increasing the Rabi frequency is only reasonable as long as it stays significantly smaller than the RF transition frequency. Especially for a radio frequency drive as presented in this thesis, breakdown of the rotating wave approximation, used in the theory for Rabi flops, can potentially be reached by the suggested methods. Currently we are far from this limit.

5.2.5. Dynamical decoupling

Experiments for testing dynamical decoupling of the ground-state qubit were carried out. In these experiments, Ramsey-like sequences of RF pulses are used, requiring phase control of

[14]Mu Guanqun at QCosmo, private communication, 12.09.2023

the RF pulses. The previously used free-running DDS from the bus system does not provide phase control. However, DDS modules at the Pulse Box are capable of both phase control and pulse shaping. Further, the output signal spectrum of a Pulse Box DDS at a frequency of 11.6 MHz does not contain higher order harmonic peaks. Due to these properties, the band-pass filter and the TTL switch were removed from the original drive circuit (Figure 5.1) when changing the RF signal source to a DDS at the Pulse Box.

At the time of installing the updated RF drive setup, all DDS units of the Pulse Box were already in use for driving acousto-optic devices in laser beam paths. A two-output RF switch was installed at the output of one of the Pulse Box DDS', such that it can supply an RF signal either to its original acousto-optical deflector (AOD) or the RF-coil, depending on the switch status. It was found that the Pulse Box DDS output power increases by 2.5 dB when lowering the frequency from 130 MHz (value sent to the AOD) to the 11.6 MHz required for the RF-coil. A 41 MHz high-pass filter was placed at the switch output going towards the AOD. The high-pass filter prevents any over-powered 11.6 MHz signal from reaching the AOD in case of an incorrect switch setting. Accidentally sending 130 MHz towards the RF-coil will result in almost the full signal power getting reflected from the coil-board. All the reflected power enters the bi-directional coupler in reverse direction where it will be absorbed, generating heat. In order to reduce such heating, a 48 MHz low-pass filter was placed at the switch output going to the RF-coil. All other parts of the circuit remain like they were in the original setup (presented in Section 5.1.1). Figure 5.14 shows a schematic of the RF-coil's drive circuit that uses a Pulse Box DDS as the RF signal source.

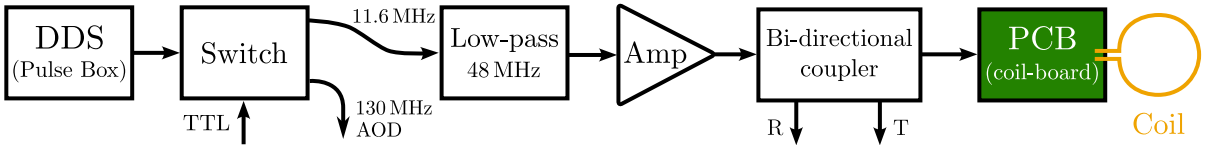

Figure 5.14.: Altered drive circuit for the coil, compared to Figure 5.1, providing phase control over the RF signal.

The output power of the Pulse Box DDS is significantly lower compared to the previously used free running DDS in the bus system (Figure 5.1). At the lowest attenuation setting, the Pulse Box DDS produces an output power of 0.74 mW = −1.3 dBm at a frequency of 11.60 MHz. The reduced RF power is expected to result in a lower Rabi frequency. According to the measured amplifier gain shown in Figure 5.2b, sending a signal at the maximum output power of the Pulse Box DDS into the amplifier results in a slightly higher amplifier gain compared to the previously used bus system DDS output power. The maximum amplifier output power is now 1.46 W — lower by a factor of 1.82 than the previous 2.66 W that were achieved with the bus system DDS. The Rabi frequency is expected to be lower by a factor of $\sqrt{1.82} \approx 1.35$. With π-times of around 60 µs measured with the previous drive circuit, the new drive circuit is expected to achieve a π-time of approximately 80 µs. Rabi flops with a π-time of $t_\pi = 107.9(1)$ µs were observed experimentally with the new

drive circuit. The difference between the measured and predicted π-time likely stems from a readjustment of the RF-coil which was carried out to ensure no blocking of the radial 729 nm beam.

Multiple π-pulses - dynamical decoupling sequences

The ability of multiple RF π-pulses (spin echos), to produce an output state that is insensitive to imperfections of the pulses, was investigated. Two different settings of the π-pulses' phases were tested in order to check which of them is more robust to pulse imperfections and therefore favourable to use for dynamical decoupling. A single ion, initialised in $|S\rangle$, was used. The applied RF pulse sequence consisted of N π-pulses, spaced by gaps of $\tau_G = 100\,\mu s$. The length of individual π-pulses was set to 108.0 µs, determined from measured Rabi flops after changing to the Pulse Box DDS drive[15]. The phase of the i-th pulse alternated between the values ϕ_{odd} and ϕ_{even} for i being an odd and an even number, respectively. The total number of π-pulses N was scanned in steps of $\Delta N = 1$ for a constant setting of the pulse phases ϕ_{odd} and ϕ_{even}. The scan was repeated for a second setting of ϕ_{odd} and ϕ_{even}. For perfect π-pulses, the excitation probability is expected to be $p = 1$ after an odd number of π-pulses and $p = 0$ after an even number of π-pulses, independent of the pulse phases. I define the contrast as the difference between excitation probabilities after N and $N + 1$ pulses.

In the first tested setting, the pulse phases alternated between $\phi_{odd} = 0$ and $\phi_{even} = \pi$, which is called the *X-2* sequence in the following. In the X-2 sequence, the later pulse ideally reverses the rotation applied by the former. Therefore, errors in rotation angle, coming from an imperfect calibration of the π-time or by a Rabi frequency drift that is slow compared to the time between two sequential pulses in the sequence, are expected to be cancelled. Experimental results from the X-2 sequence are shown in Figure 5.15 by the red data points. With the X-2 sequence, the contrast systematically decreases and revives when increasing the number of pulses N. Contrast vanishes at $N = 106(10)$ pulses and inverts such that an even number of pulses produces higher excitation than an odd number of pulses.

The X-2 sequence experiment was simulated based on the model of Rabi flops in Equation 2.53 with pulse imperfections in rotation angle and detuning taken into account. In the simulation, pulse lengths are normalised by the π-time and detunings are normalised by the Rabi frequency. The point of vanishing contrast at $N = 106(10)$ was uniquely reproduced by the simulation with a pulse length deviating by 10% from the perfect π-time and a detuning of $\Delta = 0.010(1) \cdot \Omega_0$. The error bar of Δ was obtained by matching the error bar of N in the result of the simulation. The excitation probabilities calculated by the simulation are shown in Figure 5.15 by the black curves. Decreasing the detuning in the model was found to shift the predicted point of vanishing contrast to a higher number of pulses N. With

[15]The value of 108.0 µs was a rough guide by eye. Analysis on the data containing fractionally more than the first two flops was performed afterwards and yielded $t_\pi = 108.2(3)\,\mu s$.

the experiment's Rabi frequency of $\Omega_0 = \pi/t_\pi = 2\pi \cdot 4.62(1)\,\mathrm{kHz}$ ($t_\pi = 108.2(3)\,\mu\mathrm{s}$), the detuning for matching the point of vanishing contrast is $\Delta = 2\pi \cdot 46(5)\,\mathrm{Hz}$. A frequency shift of 46(5) Hz would be caused by an ambient magnetic field drift of 16.5(16) µG according to Equation 2.35. Since ambient magnetic field drifts are typically on the order of $1\,\mu\mathrm{G\,min}^{-1}$ in our setup (Appendix B.3), and clock operation had been carried out 15 min before recording the data in Figure 5.15, the RF drive easily could have been off resonant by 46(5) Hz.

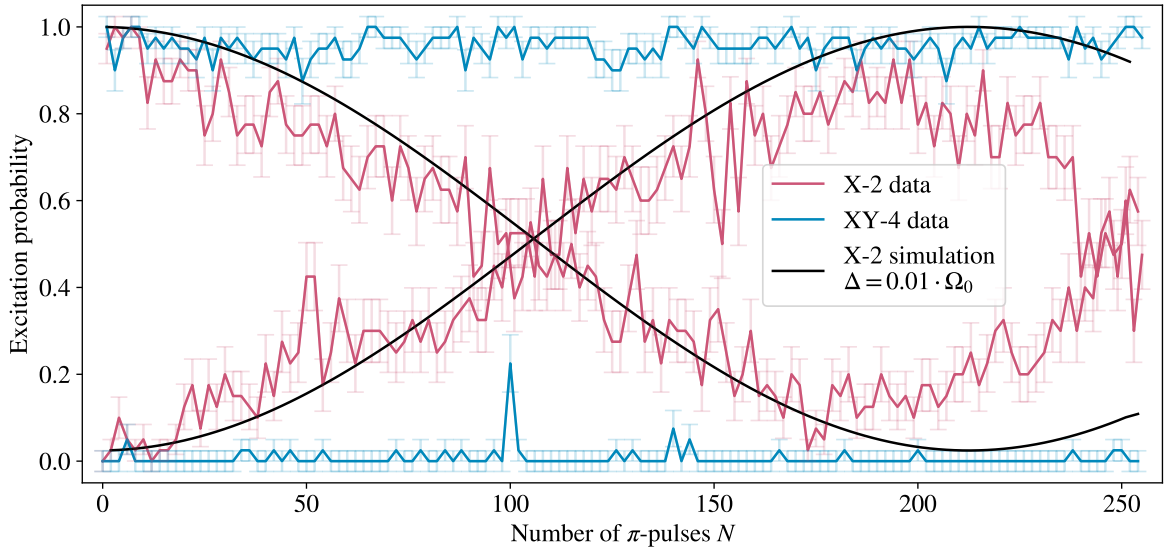

Figure 5.15.: Excitation probability after N π-pulses of the X-2 sequence (red) and XY-4 sequence (blue). The π-pulses were spaced by 100 µs. For better visibility, data points are grouped into even and odd pulse numbers. The black curves correspond to a simulation of the X-2 sequence with a detuning of $\Delta = 0.01 \cdot \Omega_0$ where Ω_0 is the Rabi frequency. For the XY-4 sequence, the contrast does not show such a systematic variation with the number of pulses. The data point at $N = 100$ with an excitation probability of 0.225 likely originated from a collision event between the ion and a background gas molecule, according to the measured PMT counts.

To cancel the influence from off-resonant driving, a second pulse sequence was tested where the pulse phases alternated between $\phi_{\mathrm{odd}} = 0$ and $\phi_{\mathrm{even}} = \pi/2$ (Equation 2.84) which is commonly called the *XY-4* sequence [105]. The measured excitation probability after N pulses of the XY-4 sequence in dependence of the pulse number N is shown by the blue data points in Figure 5.15. With the XY-4 sequence, no trend of the contrast decreasing and reviving with the number of pulses N is visible. The logical states $|0\rangle = |S\rangle$ and $|1\rangle = |S'\rangle$ are still reached with high probability after $N = 254$ pulses.

With the pulse phases of the XY-4 sequence, rotations are applied around the Bloch sphere's x- and y-axis. Four pulses of the XY-4 sequence are equal to a process that has a close to unity fidelity with the identity operation, even in the presence of constant imperfections of the rotation angles and the detunings. For example, the state evolution

during $N = 4$ pulses of the XY-4 sequence, with a pulse length deviating constantly by 10% from the perfect π-time, and a constant detuning of $\Delta = 0.1 \cdot \Omega_0$ with Rabi frequency Ω_0, is visualised on the Bloch-sphere in Figure 5.16b and also compared to the X-2 sequence with the same pulse imperfections (Figure 5.16a). When the pulse imperfections vary dynamically, additional rotations are introduced and the rotation angle depends on the amplitude of the dynamically changing imperfections. The fact that no significant reduction of contrast was observed motivates using the XY-4 sequence for all following dynamical decoupling measurements.

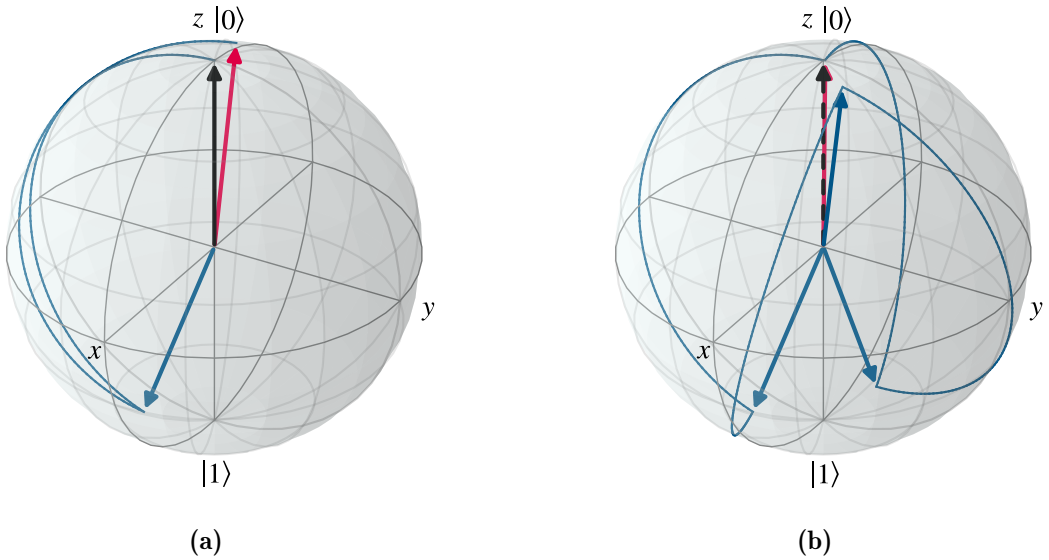

Figure 5.16.: Comparison of the state evolution during the X-2 sequence **(a)** and XY-4 sequence **(b)** on the Bloch sphere with the same constant pulse imperfections, starting with the initial state $|0\rangle$. In both cases, the pulse durations were set to deviate from the perfect π-time by 10% and detuning was set to $\Delta = 0.1 \cdot \Omega_0$ with the Rabi frequency Ω_0. For both sequences, the initial state (black vector) is compared to the final state (red vector). Blue vectors show the intermediate steps after single pulses. With the X-2 sequence, the final state vector deviates from the initial state by a rotation around the y-axis. With the XY-4 sequence, initial and final state vector are very similar and overlap in the drawing, as indicated by the dashed vector.

Ramsey contrast

For measuring the ground-state qubit's coherence time, a Ramsey experiment as introduced in Section 2.5.1 is used. Starting with the ion initialised in the state $|S\rangle$, the sequence shown in Figure 5.17 was implemented, followed by state readout of the ground-state qubit which is done with a π-pulse from $|S'\rangle$ to $3^2D_{5/2}$ and subsequent electron shelving.

The Ramsey experiment with $\phi_1 = 0$ has a total wait time of τ into which N_{SE} spin echos of the XY-4 sequence are inserted where the spin echo's phases ϕ_{SE} alternate between $\phi_{\mathrm{SE}} = 0$ and $\phi_{\mathrm{SE}} = \pi/2$. Spin echos with duration t_π are equally spaced by a time gap τ_{G}

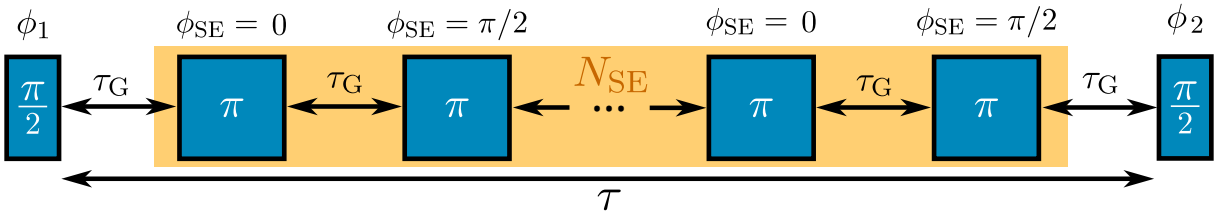

Figure 5.17.: Pulse sequence for experiments probing the coherence of the ground-state qubit. The basic structure is a Ramsey experiment with variable phases of both $\pi/2$-pulses $\phi_{1,2}$. Spin echo pulses are inserted into the Ramsey experiment's wait time τ. There are a total of N_{SE} spin echo pulses, each spaced from one another by τ_G. The phase of spin echo pulses with the XY-4 sequence alternates between $\phi_{SE} = 0$ and $\phi_{SE} = \pi/2$.

such that the Ramsey experiment's total wait time τ equals

$$\tau = N_{SE} \cdot (t_\pi + \tau_G) + \tau_G. \tag{5.2}$$

The length of spin echo pulses was set to $t_\pi = 110\,\mu s$. Rabi flops, involving the first five flops, taken on the same day, showed a π-time of $107.9(1)\,\mu s$ but were only analysed after the Ramsey experiments were carried out. The influence of such a constant calibration error on the output state after the spin echos is almost completely cancelled out with the XY-4 sequence if $N_{SE}/4$ is an integer number. The phase of the Ramsey experiment's first $\pi/2$-pulse was set to $\phi_1 = 0$. By scanning the Ramsey experiment's second pulse's phase $\phi_2 = \phi$, Ramsey fringes are obtained.

Ramsey fringes are fitted with the function given by Equation 2.78, returning the fringe contrast C and a phase shift ϕ_0. In order to limit the contrast to physical values of $0 < C < 1$, the fit was obtained using a Bayesian method with the prior-likelihood being set to zero for contrast values outside the physical range. The fit returns a median value and a surrounding confidence interval for both fit parameters, contrast and phase shift. A confidence interval of 68.27% was chosen which, in the case of the fit parameter following a Gaussian distribution, corresponds to one standard deviation. With the used Bayesian method, obtained error bars for the fit parameters are generally asymmetric. More details on the fitting algorithm and an example fit of data from a Ramsey experiment can be found in Appendix C.1. Repeating the experiment and fit for different settings of the wait time τ reveals how the contrast varies in dependence of τ.

In a basic Ramsey experiment with no spin echos, the measured contrast decay is fitted (least squares) with a Gaussian function $C(\tau) = C_0 \cdot \exp(-(\tau/T_2)^2)$, plotted in Figure 5.18a. The data and fit in Figure 5.18a do not consider a data point at a wait time of $\tau = 20\,ms$ with revived contrast due to the wait time being equal to the power line cycle period. The contrast shows decay to the $1/e$ fraction of its initial value during $T_2 = 3.9(3)\,ms$, which is commonly called the qubit's T_2-*time*. For the same Ramsey experiment, but with active line-trigger, the measured contrast decay is fitted (least squares) with an exponential function $C(\tau) = C_0 \cdot \exp(-\tau/\tau_{LT})$, plotted in Figure 5.18b. With active line-trigger, decay

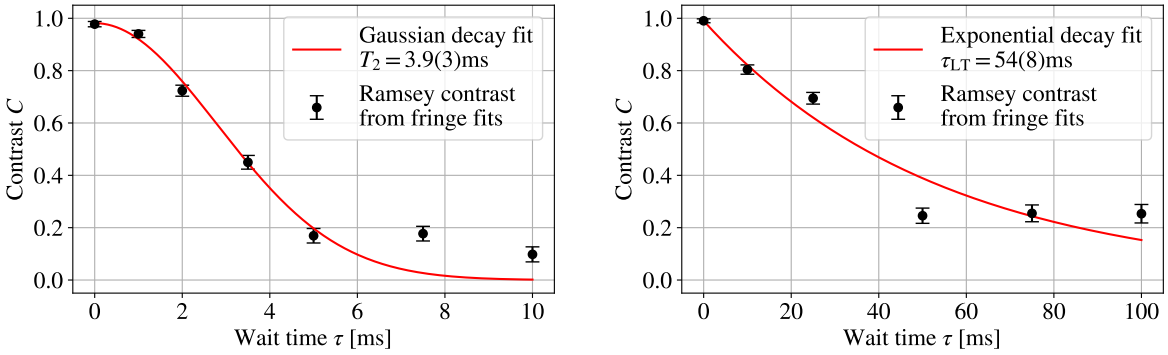

(a) **(b)**

Figure 5.18.: Decay of Ramsey contrast C for Ramsey experiments on the ground-state qubit in dependence of the wait time of the Ramsey experiments τ. The contrast values of the data points have been extracted from Ramsey fringes by fitting and have asymmetric error bars, corresponding to a 68.27% confidence interval. With deactivated line-trigger **(a)**, the contrast decays with Gaussian shape to $1/e$ contrast after 3.9(3) ms. When activating the line-trigger **(b)** the contrast decay was fitted with an exponential function, yielding $1/e$ contrast after 54(8) ms. The decay functions were fitted with least squares optimisation, weighted by symmetrised error bars.

to $1/e$ contrast after $\tau_{\mathrm{LT}} = 54(8)$ ms is found. Both decay fits are based on least squares optimisation, with weights being set by symmetrised error bars[16] of the contrast data points. Ideally one should continue with the Bayesian analysis for the decay fits instead of the presented least squares fits, however doing so involves an overhead for creating complex data structures. For the purposes of this thesis, we are only interested in the decay time's order of magnitude for which least squares fitting is sufficient. The decay time is approximately one order of magnitude longer with activated line-trigger. We are therefore strongly affected by 50 Hz noise in the ambient magnetic field.

The evolution of Ramsey contrast during the wait time τ in the case of applying spin echos was tested for three different settings for the pulse gap (τ_{G}) of 100 µs, 1.0 ms and 3.0 ms. Every configuration was tested with and without using the line-trigger system. Figure 5.19 shows the evolution of Ramsey contrast during the wait time for all tested configurations. For pulse gaps of $\tau_{\mathrm{G}} = 100$ µs — significantly shorter than the ground-state qubit's T_2-time of 3.9(3) ms — no reduction of contrast is observable up to the longest measured wait times of $\tau = 210.1$ ms. For longer gaps of $\tau_{\mathrm{G}} = 1.0$ ms and $\tau_{\mathrm{G}} = 3.0$ ms, contrast decay over the timescale of several tens of milliseconds is clearly evident. Line-trigger improves the contrast for pulse gaps that are larger than the ground state qubit's T_2-time of 3.9(3) ms (Figure 5.18a).

Ramsey fringes after $N_{\mathrm{SE}} = 10$, $N_{\mathrm{SE}} = 100$ and $N_{\mathrm{SE}} = 1000$ are shown in Figure 5.20. In each case a spin echo gap of $\tau_{\mathrm{G}} = 100$ µs was used. A shift in the phase of Ramsey fringes

[16] Calculated as the average of upper and lower error.

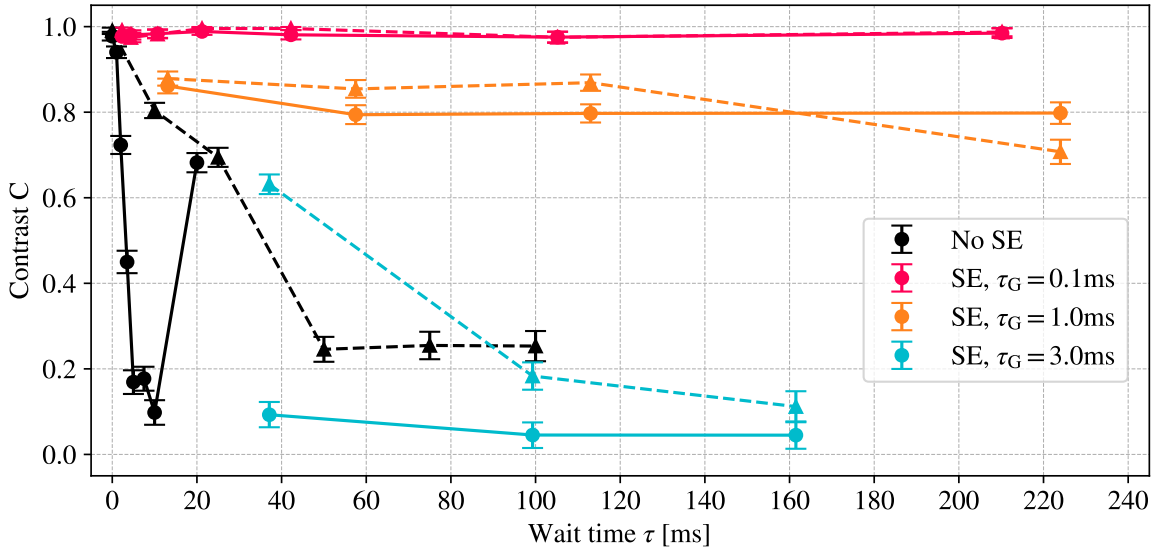

Figure 5.19.: Summary of ground-state Ramsey contrast measurements in various configurations indicated by colors. Solid lines with circles correspond to deactivated line-trigger, dashed lines with triangles correspond to the same experiments (matching colors) but with activated line-trigger. The black data points are from Ramsey experiments with no spin echos. The contrast revives at the last data point at 20 ms because of matching a single period of the 50 Hz power line cycle. Spin echo pulses were applied for three different settings of the pulse gap τ_G (defined in Figure 5.17) as shown in the legend.

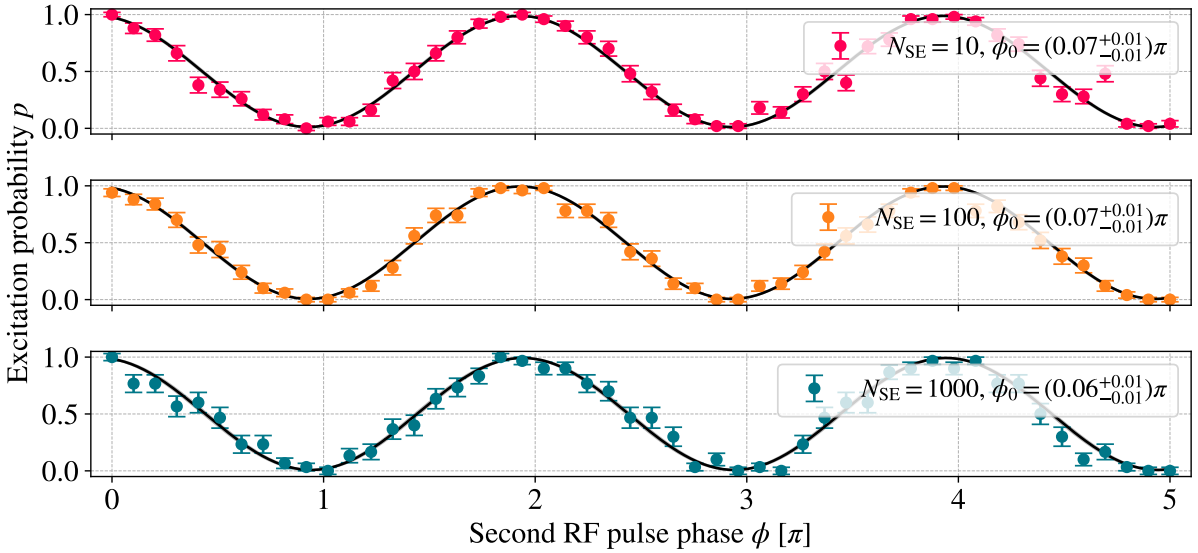

Figure 5.20.: Ramsey fringes for spin echo sequences with $N_{SE} = 10$ (red circles, top), $N_{SE} = 100$ (orange circles, middle) and $N_{SE} = 1000$ (blue circles, bottom) spin echos spaced by time gaps of $\tau_G = 100\,\mu s$. A function $p(\phi) = 1/2 + A/2 \cdot \cos(\pi(\phi + \phi_0))$ is fitted to the data by a Bayesian maximum likelihood method (black lines).

ϕ_0 as the number of pulses N_{SE} is changed would be indicative of dynamically-changing detuning during a single round of four XY-4 spin echos. Phase shifts ϕ_0 are extracted from the fringes by fitting the function given by Equation 2.78 using a Bayesian algorithm. No statistically-significant change in the phase is evident in the data. To increase the confidence that the fringe phase is not changing when increasing the number of spin echos, fringes should be recorded at an even higher number of spin echo pulses.

State tomography

The last measurement with the ground-state RF drive aimed at pushing the duration of dynamical decoupling as far as possible while characterising the quality of the ground-state quantum memory. The Ramsey experiments in the previous subsection only measured the coherence of the output state after dynamical decoupling. For a complete characterisation of the output state, quantum state tomography was performed. Furthermore, the output states were reconstructed for the input states $|0\rangle$, $|+\rangle$ and $|+i\rangle$. The pulse sequence shown in Figure 5.17 was used, with the following difference: The $\pi/2$-pulses were optional and their phases were adjusted. Specifically, the first $\pi/2$-pulse with phase ϕ_1 was used to prepare certain input states. A phase of $\phi_1 = 0$ prepares the state $|+\rangle$. A phase of $\phi_1 = \pi/2$ prepares the state $|+i\rangle$. Omitting the pulse entirely prepares the state $|0\rangle$. In the same way, the basis of the final projective measurement is determined by the second $\pi/2$-pulse. If there is no second $\pi/2$-pulse applied, the qubit is measured in the logical basis. Performing the second $\pi/2$-pulse with $\phi_2 = 0$ rotates the qubit such that population in $|+\rangle$ is transferred to $|1\rangle$. Therefore, the measured excitation probability now corresponds to the probability for finding the state $|+\rangle$, implementing a projective measurement in the $\pm$ basis. When setting $\phi_2 = \pi/2$, the measured excitation probability represents the probability of finding the state $|+i\rangle$, implementing a projective measurement in the $\pm i$ basis. In total there are nine different combinations of input states and measurement bases.

The nine different combinations of input state and output state measurement basis were executed for a dynamical decoupling sequence consisting of $N_{\mathrm{SE}} = 2 \cdot 10^4$ XY-4 spin echos. The spin echo pulse length was set to 108 µs and the gap between spin echos was set to $\tau_{\mathrm{G}} = 100\,\mu\mathrm{s}$. According to Equation 5.2, the full wait time between state preparation and projective measurement is then $\tau = 4.1601\,\mathrm{s}$. Such long pulse sequences were found to operate the Pulse Box at its memory limit, preventing measurements at longer wait times. The measured excitation probabilities for all nine combinations of input states and measurement bases are listed in Table 5.1.

State reconstruction was performed with a maximum likelihood method [144, 145] using pre-existing Python code written within the Quantum Optics & Spectroscopy group. More information on the implementation is given in Appendix C.2. Reconstructed density matrices for the input states $|0\rangle$, $|+\rangle$ and $|+i\rangle$ are shown in Figure 5.21. From the reconstructed density matrices, fidelities with the respective input states were calculated using Equation 2.21. Uncertainties in quantities derived from the reconstructed density

Table 5.1.: Measured probabilities for state tomography after $2 \cdot 10^4$ XY-4 spin echos over a total time of 4.16 s. Probabilities were measured for nine combinations of input state and measurement basis. The numbers of cycles for estimating each probability are listed in the outer right column.

Input state	Measurement basis	Excitation probability	Cycles
$\|0\rangle$	$\pm$	0.575(78)	40
$\|0\rangle$	$\pm i$	0.550(111)	20
$\|0\rangle$	logical	0.150(80)	20
$\|+\rangle$	$\pm$	0.800(63)	40
$\|+\rangle$	$\pm i$	0.775(66)	40
$\|+\rangle$	logical	0.350(75)	40
$\|+i\rangle$	$\pm$	0.383(63)	60
$\|+i\rangle$	$\pm i$	0.750(68)	40
$\|+i\rangle$	logical	0.425(78)	40

matrices (e.g., the fidelity) were estimated via the Monte-Carlo technique as described in Appendix C.2. The obtained state fidelities from reconstructed density matrices and their confidence interval boundaries are listed in Table 5.2. Histograms of the fidelity distributions can be found in Appendix C.2. An average state fidelity of $F = 0.80^{+6}_{-10}$ is found where the errors represent a 68.27% confidence interval. The coherence time of the ground-state qubit in our setup was previously characterised by a Ramsey contrast of 0.67(3) after 66 ms [42]. To make a comparison to this best previous coherence time, a Ramsey contrast for the output state in the case of the input state $|+\rangle$ was calculated from the reconstructed density matrix. After 4.16 s of XY-4 dynamical decoupling, a Ramsey contrast of 0.81^{+9}_{-15} was found.

Table 5.2.: Obtained output state fidelities after 4.1601 s of XY-4 dynamical decoupling for the input states $|0\rangle$, $|+\rangle$ and $|+i\rangle$. The fidelities of the reconstructed maximum likelihood density matrices are shown. Upper and lower bounds correspond to a 68.27% confidence interval that was obtained by Monte-Carlo sampling of density matrices.

Input state	Maximum likelihood fidelity	Lower bound	Upper bound
$\|0\rangle$	0.850	0.740	0.897
$\|+\rangle$	0.800	0.721	0.844
$\|+i\rangle$	0.750	0.675	0.807

Based on the reconstructed density matrices, there may be evidence of a unitary rotation in addition to decoherence. Given the statistical uncertainties, it is not absolutely clear from the data if there is a unitary rotation present. In order to verify and characterise a unitary rotation, quantum process tomography could be carried out, which requires a fourth input state (e.g. the state $|1\rangle$). At the time of writing this thesis, process tomography of spin echos was carried out by PhD student James Bate. The preliminary results confirm

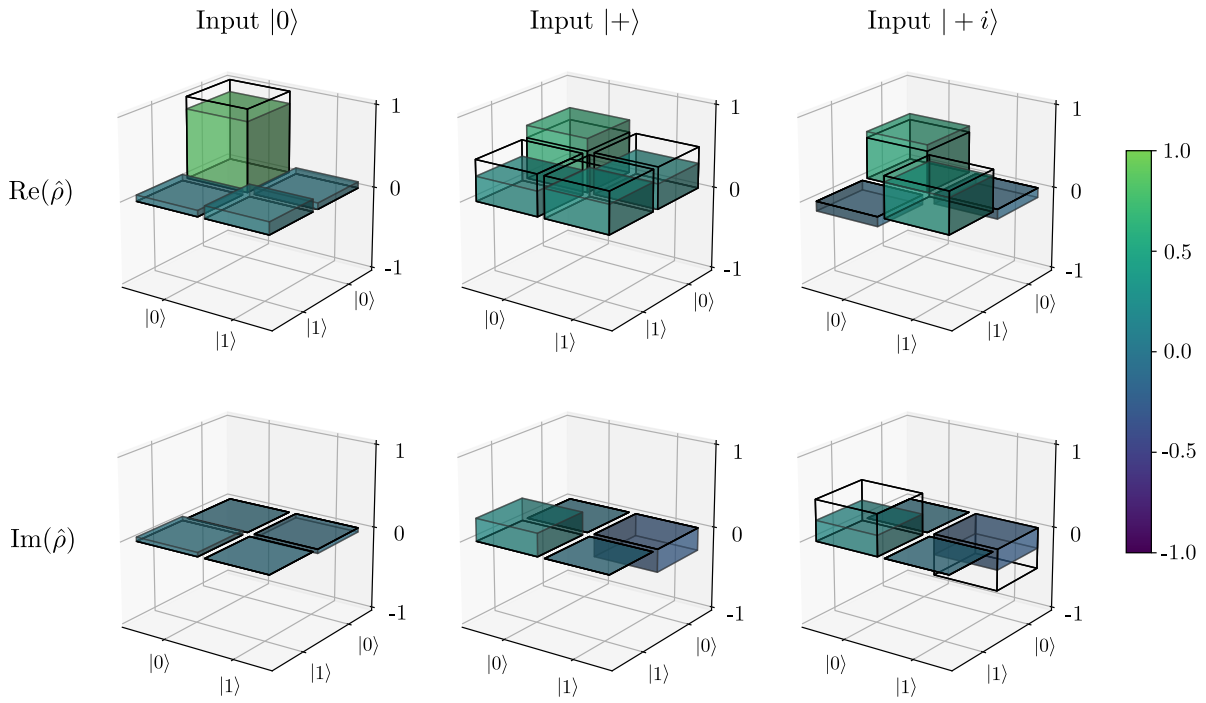

Figure 5.21.: Reconstructed density matrices from the input states $|0\rangle$, $|+\rangle$ and $|+i\rangle$ after applying $2 \cdot 10^4$ XY-4 spin echos for dynamical decoupling. With the gap between spin echo pulses being 100 µs and a pulse length of 108 µs, the total wait time is 4.1601 s. Density matrix entries are plotted separately in their real and imaginary parts where the colors represent their amplitude. The black lined edges indicate the input states which ideally should be reproduced by dynamical decoupling.

the presence of a unitary rotation that is caused by the spin echos. The infidelities of the qubit states could be a result of pulse imperfections that vary during the duration of four spin echo pulses of the XY-4 sequence. With pulse gaps of $\tau_G = 100\,\mu s$ and pulse lengths of $t_\pi = 108\,\mu s$, such a cycle of four spin echos has a duration of 732 µs. Consequently, noise at frequencies in the kilohertz regime and higher in the Rabi frequency and in detuning could lead to pulse imperfections which can not be compensated by the XY-4 sequence. There exist more advanced decoupling sequences which have proven to be robust against pulse imperfections that change between individual pulses [106, 110, 111]. Testing the performance of these sequences in our experimental system is left for future work.

5.3. Conclusion

This chapter presented the development and integration of a radio frequency (RF) drive for the $^{40}Ca^+$ ground-state qubit into the existing experimental setup. An electronic circuit including an RF antenna was set up. The antenna has the shape of a coil and produces a magnetic field which oscillates at a frequency of 11.62 MHz. Driving of the $4^2S_{1/2,m=-1/2}$

to $4^2S_{1/2,m=+1/2}$ ground state transition in a single trapped $^{40}Ca^+$ ion was achieved with a Rabi frequency of up to $\Omega_0 = 2\pi \cdot 8.637(6)\,\mathrm{kHz}$, corresponding to a π-time of 57.89(4) µs. To achieve that Rabi frequency, it was important to adjust the coil position at one of the vacuum chamber's viewports, probably to minimise currents induced in the bulk of the vacuum chamber, and consequently to maximise the magnetic field strength at the ion position. Specifically, an off-centre coil placement with respect to the viewport showed a significant increase of the Rabi frequency. Rabi flops have little damping, showing an amplitude of 0.68(5) after 50 ms of continuous driving (corresponding to 863 flips between the logical states), but suffer from systematic dynamic changes of the Rabi frequency through the duration of RF driving on the 10^{-2} level. Flops are dampened if the Rabi frequency fluctuates randomly during multiple repetitions of the pulse sequence. In our setup, such random fluctuations can be caused by ambient magnetic field noise. The systematic dynamic change of the Rabi frequency was found to be caused by heating in the coil's drive circuit, specifically at the amplifier.

In the present experimental setup, the Rabi frequency cannot easily be increased for several reasons. First, the distance between the coil and the ion cannot be reduced further, given the size of our vacuum chamber. Increasing the coil's radius did not result in the desired increase of field strength at the ion's position, presumably due to higher coupling of the magnetic field to surrounding metallic parts. In addition, drifts of the Rabi frequency are stronger with a bigger radius coil, presumably due to an increased resistance of the coil which causes stronger heating of the coil-board due to power dissipation. The precision of pulses is mainly limited by the dynamic changes of the Rabi frequency, caused by heating in the coil and its drive circuit. Increasing the Rabi frequency by a higher RF power is not favourable because heating effects are expected to become stronger. In order to minimise dynamic changes of the Rabi frequency without reducing the RF power, I suggest implementing an active feedback loop for stabilising the RF power.

To perform dynamical decoupling of the ground-state qubit using the direct RF drive, self-correcting pulse sequences, robust to constant imperfections of pulse length and detuning, were used. These pulse sequences suppressed the influence of pulse imperfections on the ground-state qubit's memory performance, originating from fluctuating detuning and the drifting Rabi frequency. Without dynamical decoupling, the coherence time of the ground-state qubit was determined to be 3.9(3) ms ($1/e$ contrast), which increased to 54(8) ms ($1/e$ contrast) when triggering the experiment always at the same phase of the 50 Hz power line cycle in our laboratory. When using the XY-4 dynamical decoupling sequence [105] with spin echos spaced by 100 µs and without line-trigger, no reduction of the Ramsey contrast could be resolved for wait times up to 210.1 ms. Finally, the ability to protect various initial qubit states by XY-4 dynamical decoupling was demonstrated. After 4.1601 s, the average fidelity of the qubit state with respect to the initial state was found to be $F = 0.80^{+6}_{-10}$. The infidelity can have contributions from background magnetic field noise and varying pulse imperfections, both on timescales significantly faster than 732 µs, which corresponds to the duration of four spin echo pulses and their spacings. The corresponding frequencies

which affect us are therefore on the order of several kilohertz and higher. It is likely that the results can be improved by using more complex dynamical decoupling sequences, such as Knill decoupling [110] combined with composite pulses [106]. Going to even longer wait times is currently not possible due to hardware and software limitations of the experiment control system. The best previous memory performance in our setup was characterised by a Ramsey contrast of 0.67(3) after 66 ms [42]. The Ramsey contrast of 0.81^{+9}_{-15} after 4.16 s reported here is consistent with a significant improvement of the coherence time. To further extend the memory's coherence time, one should consider using a different ion species with non-zero nuclear spin, providing microwave transitions between hyperfine states which, in first order approximation, are insensitive to changes of the ambient magnetic field [108]. Having measured quantum coherence after more than four seconds shows that the presented implementation surpasses the 1.15 s life time of the optical qubit in $^{40}Ca^{+}$, truly utilising the potential of the ground-state qubit for a quantum memory.

6. Summary and outlook

Summary

Two radio frequency (RF) control implementations were presented that enhance the functionalities and the performance of a trapped $^{40}Ca^{+}$ ion quantum network node. Both implementations are steps towards a multi-qubit processing node that can store quantum states on the timescale of seconds.

The first radio frequency control implementation was presented in Chapter 4 and deals with the aspect of multi-qubit processing. In order to perform quantum information processing and especially fast high-fidelity entangling gates on a linear string of trapped-ion qubits, it is favourable to use the ion trap's radial motional modes. In our setup, the radial modes' frequencies previously showed drifts of several kilohertz on the timescale of minutes, which prevented coherently driving these modes. To overcome this problem, the mode frequencies were stabilised by an active feedback loop for the power in the ion trap's radio frequency drive circuit.

The feedback loop inductively picks off a part from the radial trap electrode's drive signal and applies attenuation to it, based on a stabilisation unit with proportional-integral control. Radial motional mode frequency stability was probed on two different timescales. During one hour, a timescale much longer than individual experiments, a standard deviation of 35(3) Hz around a mean radial mode frequency of 2.682 342(10) MHz was observed for a single trapped ion, yielding a fractional stability of $1.3(1) \cdot 10^{-5}$. Short time stability on timescales of individual experiments (milliseconds) was tested by measuring the motional coherence of the radial blue sideband, which showed $1/e$ decay after 13(1) ms. Long-term stability is currently strongly affected by changes in the laboratory humidity. Short-term stability, characterised by the motional coherence time, is dominantly affected by electronic noise in the stabilisation unit.

At the time of writing this thesis, an updated version of the stabilisation unit has already been tested in the 2D crystals experiment, lead by Christian Roos, where improved motional coherence times have been measured. The radial modes in our system are now ready to be used for entangling operations that exploit them [146]. With the achieved radial mode frequencies of almost 3 MHz being significantly higher than their axial counterpart for strings of around ten ions, entangling gates between ions are expected to be faster using the radial modes. Further, at the achieved mode frequencies, radial mode heating rates of a trapped ion are lower than those in the axial mode, which also improves the fidelity of the entangling operations. From a geometrical perspective, in our experimental setup both

the cavity and the addressed 393 nm beam for photon generation are oriented in the radial direction, making the photon generation process susceptible to ion motion in this direction. The stabilised radial frequencies now enable to accurately set up and validate sideband cooling of the radial motional modes. A more careful investigation of the influence of ion motion in the radial plane on the photon generation process can now be carried out.

The second radio frequency control implementation was presented in Chapter 5 and is aimed at improving the lifetime of the quantum network node's memory. In our experiment, the quantum memory is implemented by the $^{40}Ca^{+}$ ground-state qubit with the basis states $4^2S_{1/2,m=-1/2}$ and $4^2S_{1/2,m=+1/2}$. Previously, Ramsey contrast decay to 0.67(3) after 66 ms was reported for the ground-state qubit in our experimental system [42]. For these previous memory experiments, the method of dynamical decoupling was used, implemented by laser pulses. The main source of infidelity of the memory was identified to be imperfections of the dynamical decoupling pulses due to the laser light coupling to the ion's motion. For increasing the fidelity of dynamical decoupling operations, a direct drive for the qubit's transition frequency of 11.62 MHz was implemented in the context of this thesis. At such radio frequency drive fields, the coupling to an ion's motion becomes negligible.

The magnetic dipole transition between the $4^2S_{1/2,m=\pm1/2}$ states was driven by an oscillating magnetic field, produced by a coil-shaped RF antenna which is mounted outside of our vacuum chamber. Rabi flops with a π-time of 57.89(4) µs were observed. These Rabi flops show only weak amplitude damping: 68(5)% of the amplitude is left after 50 ms of continuous driving, corresponding to 863 spin flips between the logical states. The Rabi frequency is mainly limited by the distance between the coil and the ion, which in our setup can only be decreased by placing the coil inside the vacuum chamber. An approach to increase the magnetic field strength at the ion position by utilising a coil with larger radius was not successful. Separately, heating in the coil and its drive circuit was found to cause drifts of the RF power and consequently also drifts of the Rabi frequency. Dynamic changes of the Rabi frequency through several sequence repetitions have a fractional amplitude on the order of 10^{-2} and are detectable when performing RF driving for at least tens of milliseconds. The drifting Rabi frequency limits the precision of qubit rotations that are performed by individual RF pulses.

While being aware of the pulse imperfections, the ground-state qubit's coherence was investigated when applying dynamical decoupling. The XY-4 pulse sequence [105] was used where, in the presence of constant pulse imperfections, the unitary from four subsequent pulses has a high fidelity with the identity operation. For dynamic pulse imperfections, this fidelity with the identity operation is expected to reduce. In Ramsey experiments with 210.1 ms of XY-4 dynamical decoupling, having gaps of 100 µs in between the decoupling pulses, no significant reduction of the Ramsey contrast was observed. The transformation of three different input states during 4.16 s of the same dynamical decoupling sequence was investigated by quantum state tomography. An average state fidelity of $F = 0.80^{+6}_{-10}$ between output and input state was found. The infidelity likely has its origin in the drive circuit's heating effects as well as drifts and fluctuations of the ambient magnetic field.

The use of dynamical decoupling sequences which are more robust against dynamically changing pulse imperfections [110, 112] are expected to improve the state fidelity of our quantum memory. The Ramsey contrast after 4.16 s was estimated from the data to be 0.81^{+9}_{-15} and compares to the best previous value of 0.67(3) after 66 ms. This improvement of the Ramsey contrast is consistent with a significant increase of the ground-state qubit's coherence time.

Outlook

Combining both presented extensions to the experimental setup enables novel quantum network experiments with trapped ions. During the time of writing this thesis, experiments were carried out by PhD students James Bate and Marco Canteri, picking up where both projects presented in this thesis left off. The first group of these new experiments involves axially shuttled strings of up to ten ions, from which a train of single photons is emitted, each photon entangled with one of the ions. These experiments investigate the possibilities of multimoding [120] and enhanced entanglement distribution. Quantum logic operations, as required for such experiments, were previously only achieved in our system for up to three ions using the axial motional modes. For a string of ten ions, quantum logic operations using the axial motional modes have unfavourably low fidelity. In contrast, the radial modes are stable and ready now for the implementation of quantum logic gates on a ten ion string.

The second group of recent experiments focusses on investigating the lifetime of entangled ion-photon states with long lasting quantum memories in the ion. Dynamical decoupling with direct RF driving, as presented in this thesis, was already tested in combination with ion-photon entanglement, showing promising results with lifetimes on the order of a second for the entangled ion-photon state[1].

The uniformity of Rabi frequencies from the ground-state RF drive with respect to the axial position of an ion remains still to be determined. With a similar implementation of a direct RF drive for the $^{40}Ca^{+}$ ground-state qubit in the 2D crystals experiment in the group of Christian Roos, Rabi frequencies differing by 2% were found in a two-dimensional crystal of 91 ions[2]. However, the spatial profile of the RF magnetic field strength strongly depends on the trap and chamber geometry, which is different in our setup. It is not clear yet how such differences of the Rabi frequency across the ion string will affect the fidelities of the dynamically decoupled quantum memories. Successfully combining strings that contain on the order of ten ions with memory lifetimes on the order of seconds will push the boundaries for quantum network nodes. In particular, using such nodes as quantum repeaters is expected to enable quantum network applications on inter-city distances and beyond, as investigated in the recent paper from my group using two ions [42].

[1] J. Bate, private communication, 06.09.2023
[2] M. Bock, private communication, 26.08.2022

A. Setup details

A.1. Circuit drawing of the trap RF power stabilisation unit

The contents of this Appendix have been removed at the request of the owner of the copyright of the circuit diagrams that it originally contained.

A.2. Coil-board component values

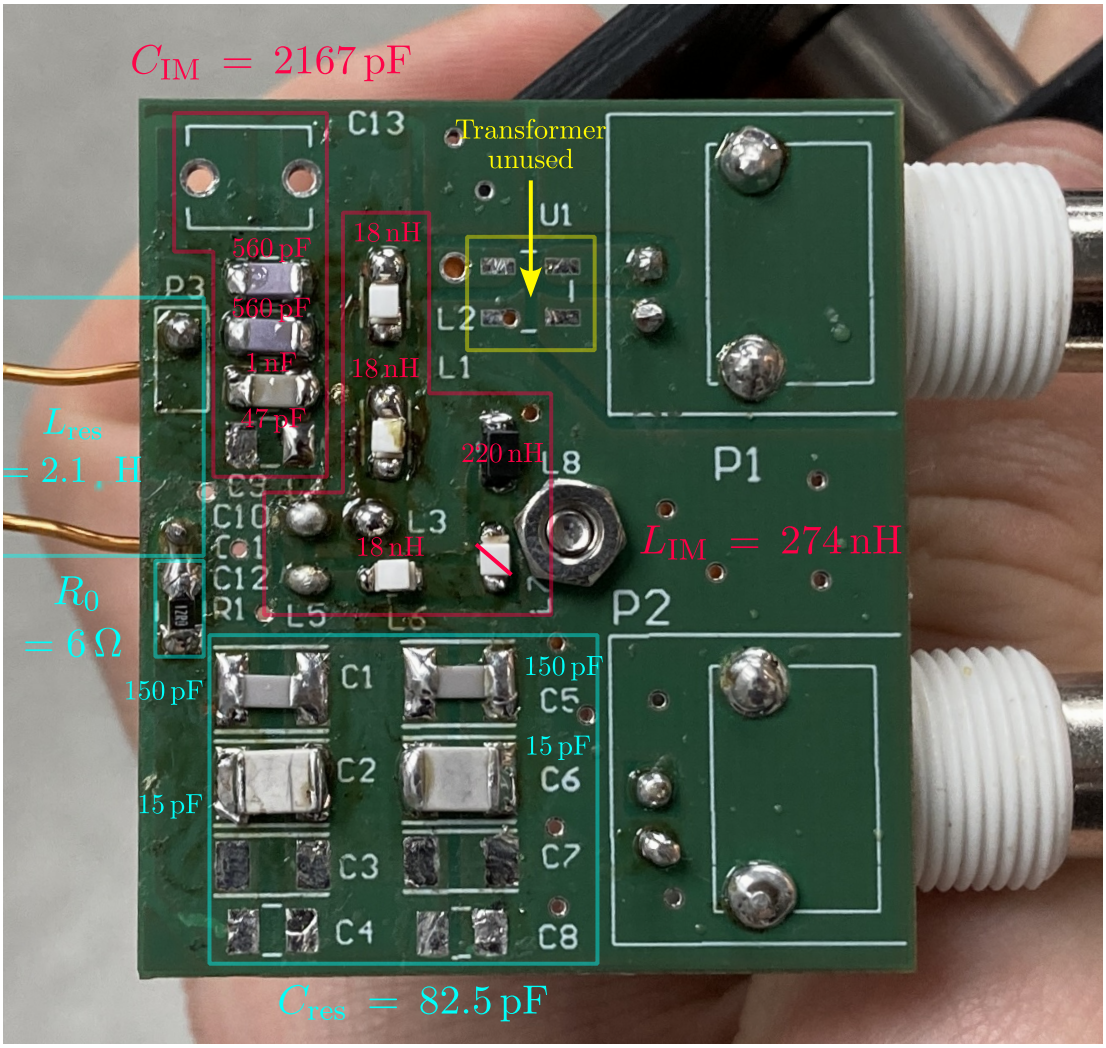

Figure A.1.: Photograph of the coil-board with component values indicated. The photograph was taken in an earlier configuration (14.12.2022), but labels specify component values at solder pads from the final configuration (03.02.2023), which produced the reflection spectrum in Figure 5.4 and was used to take all data in Section 5.2, except for Section 5.2.2. Blue labels correspond to components for the RLC resonance circuit, red labels correspond to components for impedance matching. The coil-board has two BNC input ports P1 and P2. The BNC port P1 features solder pads for a transformer (yellow label) before connecting to the impedance matching and RLC resonance circuit. The BNC port P2 is directly connected to the impedance matching and RLC resonance circuit. For the implementation presented in this thesis, no transformer was placed at the designated solder pads, and consequently the BNC port P2 was used.

B. Supplementary measurement details

B.1. Final calibration of the radial motional mode frequencies

The calibration of the radial motional mode frequencies in Section 4.2.1 showed the dependence of radial mode frequencies on the stabilisation unit's pickoff monitor output power. It was noted there that these measurements were not taken in the final configuration of the trap's RF drive circuit. After the measurement presented in Section 4.2.1, the following changes were made to the trap's RF drive circuit: First, the power supply socket for the stabilisation unit was changed such that the whole trap RF drive circuit is powered from a single multi-socket. With such star-shaped power distribution, ground-loops are expected to be reduced [139]. Second, a 1:1 transformer was added to the RF pickoff signal for further galvanic isolation. Third, the pickoff signal's attenuation before entering the stabilisation unit was changed.

In this appendix section, a calibration of the trap's radial motional mode frequencies is presented that was carried out with the latest circuit configuration from Figure 4.1. The procedure was similar to what is described in Section 4.2.1 with the following differences: First, the carrier frequency was not measured directly by a spectroscopy scan, but was calculated as the frequency in the middle between the red and blue sideband peak's centre frequencies. The centre frequencies of the red and blue sideband peaks were measured by spectroscopy scans. Second, the stabilisation unit's pickoff monitor output power was not logged during the calibration measurement. Therefore, the obtained calibration curve only gives the dependence of radial mode frequencies on the stabilisation unit's digital 10-bit set-point x, shown in Figure B.1a.

As the set-point is related to the output voltage from the pickoff signal's RMS detection, the set-point is proportional to the blade voltage and a linear dependence is obtained for the radial mode frequencies. Functions $\nu_\mathrm{r}(x) = a \cdot x + b$ are fitted to the data (least squares), giving $a = 3.437(3)\,\mathrm{kHz}$, $b = -0.59(3)\,\mathrm{MHz}$ for the higher frequency radial mode and $a = 3.510(6)\,\mathrm{kHz}$, $b = -1.45(5)\,\mathrm{MHz}$ for the lower frequency radial mode. In agreement with the results presented in Section 4.2.1, the negative offset b suggests that there currently exists a power threshold in our setup below which no voltage is applied to the trap's radial electrodes.

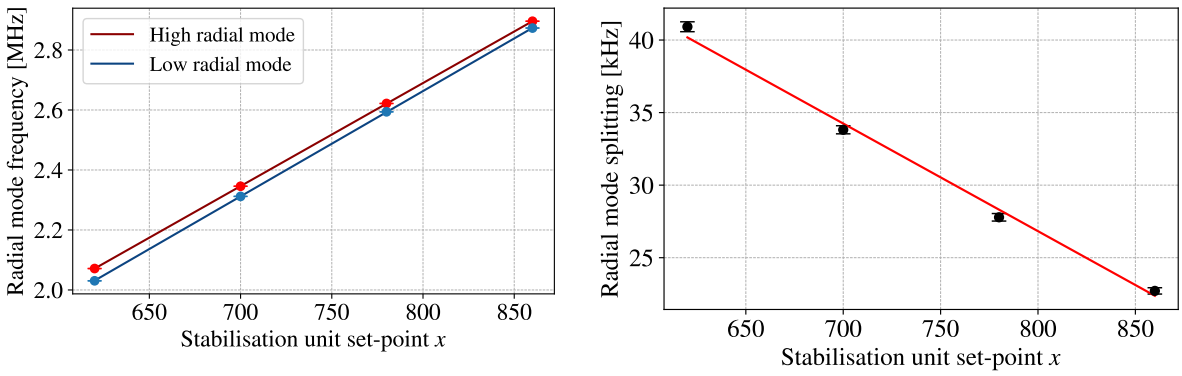

(a) **(b)**

Figure B.1.: a) Radial mode frequencies in dependence of the stabilisation unit's set-point. The data was obtained with the final configuration of the trap's RF drive circuit (shown in Figure 4.1). **b)** The frequency splitting between the higher and lower frequency radial mode in dependence of the stabilisation unit's set-point. All solid lines are least squares fits with functions of the form $y = a \cdot x + b$.

The frequency splitting between the higher and the lower frequency radial mode decreases with increasing set-points. This frequency splitting is caused by an offset voltage of 1.5 V that is applied to the radial trap electrode pair which is held at a DC voltage. The linear least squares fit on the radial mode's frequency splitting $\Delta\nu_{\mathrm{r}}(x) = a \cdot x + b$, shown in Figure B.1b, yields $a = -74(4)$ Hz and $b = 86(3)$ kHz. The fit has $\chi^2/\mathrm{d.o.f.} = 6.8$, however it relies only on four data points. For a more precise test of the assumption of a linear dependence, more calibration data points are needed.

B.2. Radial mode stability during one hour - carrier frequency drift

During the one-hour-long measurement of the radial mode frequency stability in Section 4.2.2, the frequencies of the 729 nm laser and the $4^2S_{1/2,m=-1/2}$ to $3^2D_{5/2,m=-5/2}$ carrier transition were drifting apart. Such drifts can be caused by drifts of both the ambient magnetic field and the length of the reference cavity. In order to keep the laser on resonance with the carrier transition, clock operation (as explained in Section 3.2.3) was carried out in between individual spectroscopy scans of the radial red sideband. Running the clock adjusts the frequency of an AOM in the 729 nm beam path. The same AOM was used to set the laser frequency for the radial sideband spectroscopy scans. Consequently, the radial mode frequency was calculated as the difference between the AOM frequencies for resonant driving of the red sideband and the carrier transition. From one block of clock operation in between two sideband spectroscopy scans, a carrier AOM frequency is calculated as an average, weighted by the wait time in the clock's Ramsey experiments. The carrier

AOM frequency at the time stamp where the spectroscopy scan reached the peak's centre frequency was estimated by a linear interpolation between the neighbouring data points of the carrier AOM frequency. Figure B.2 shows the evolution of the carrier AOM frequency during the one hour stability measurement. During 62 min the carrier AOM frequency drifted by −509 Hz.

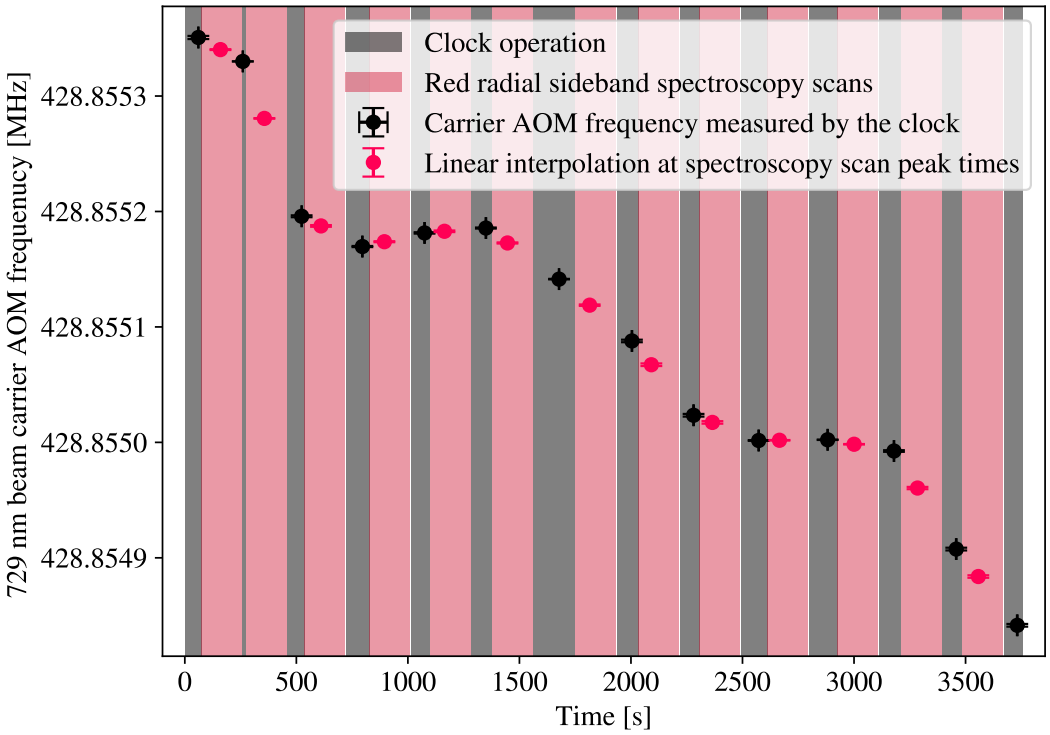

Figure B.2.: Drift of the carrier AOM frequency of the 729 nm laser during 62 min as part of the long time radial mode frequency stability measurement from Section 4.2.2. The carrier AOM frequency (black data points) is, by running the clock, set to provide resonant laser driving of the $4^2S_{1/2,m=-1/2}$ to $3^2D_{5/2,m=-5/2}$ carrier transition. The data was recorded by multiple blocks of clock operation (grey shading) in between spectroscopy scans on the radial red sideband (red shading). The red data points are linear interpolations of the carrier AOM frequency at the time stamps where, in the radial sideband spectroscopy scans, the radial mode peak's centre frequency was reached.

B.3. Ambient magnetic field fluctuations

Drifts and fluctuations of the ambient magnetic field were measured by clock operation (explained in Section 3.2.3). The magnetic field measurement was done twice: once with open mu-metal shield door on 03.02.2023 (Figure B.3a), and once with closed mu-metal shield door 17 days later on 20.02.2023 (Figure B.3a). For both measurements, the drift rate was determined by a linear least squares fit. After subtracting the linear drift, the magnetic

field only shows fluctuations around a mean value. These fluctuations are characterised by fitting a Gaussian function to the histogram of the fluctuations (least squares minimisation), which extracts their standard deviation (half-width-half-maximum). For open shield door, a linear drift rate of $0.6(1)\,\mu\mathrm{G\,min^{-1}}$ and fluctuations with a standard deviation of $4.2(2)\,\mu\mathrm{G}$ were found. Closing the shield door reduced the fluctuations to a standard deviation of $2.5(1)\,\mu\mathrm{G}$. The measured linear drift rate of $1.04(2)\,\mu\mathrm{G\,min^{-1}}$ is higher with the closed shield door which is likely explained by changes happening during the 17 days in between both measurements.

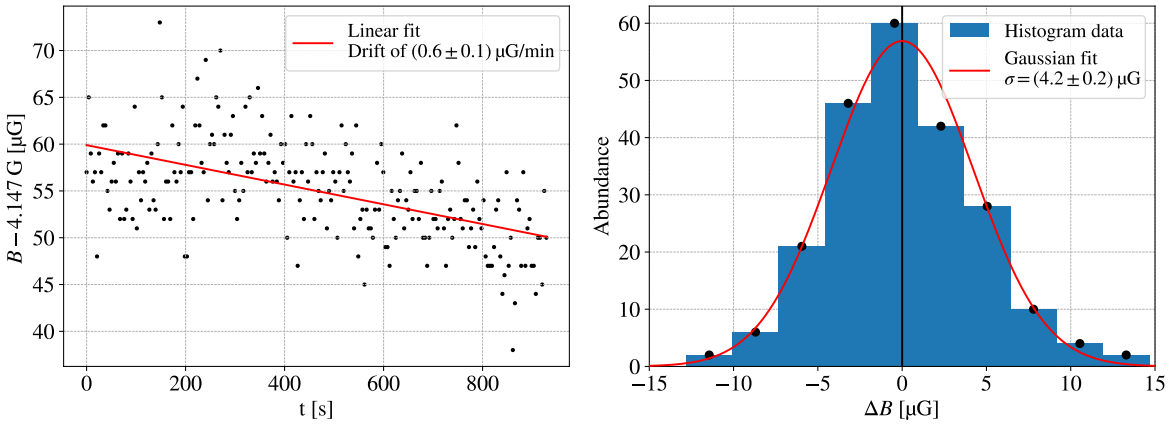

(a)

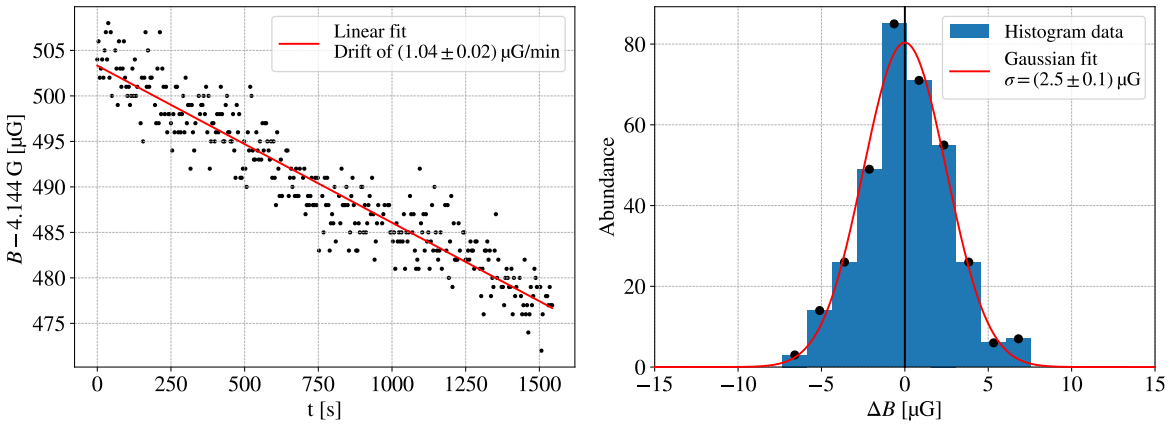

(b)

Figure B.3.: Ambient magnetic field drifts and fluctuations, measured by clock operation, with open **(a)** and closed **(b)** mu-metal shield door. Time traces on the left show the linear fit for the drift rate. The histograms on the right are based on data where this drift was subtracted and only fluctuations on timescales shorter than tens of seconds remain. A Gaussian fit on the histogram's bin centres extracts the standard deviation of the fluctuations.

B.4. Power stability in the RF-coil's drive circuit

In Section 5.2.4, power drifts in the RF-coil's drive circuit (see Figure 5.1) were reported. This appendix section discusses more details of the underlying measurement. Power time traces were recorded separately at the amplifier output and the reflection pickoff output of the bi-directional coupler using an RF powermeter[1]. The RF signal was operated continuously at a frequency of 11.60 MHz, which is off-resonant to the coil-board's resonance frequency by roughly 20 kHz, but the detuning is comparably small considering the coil-board's bandwidth of 824 kHz. Recording the power time traces was started after switching the RF signal on by the TTL switch and stopped after the power reached a stable value in the "hot" equilibrium state. The time traces were recorded separately with 10 min of waiting in between such that the system can return to its initial "cold" state. The time traces are shown in Figure B.4.

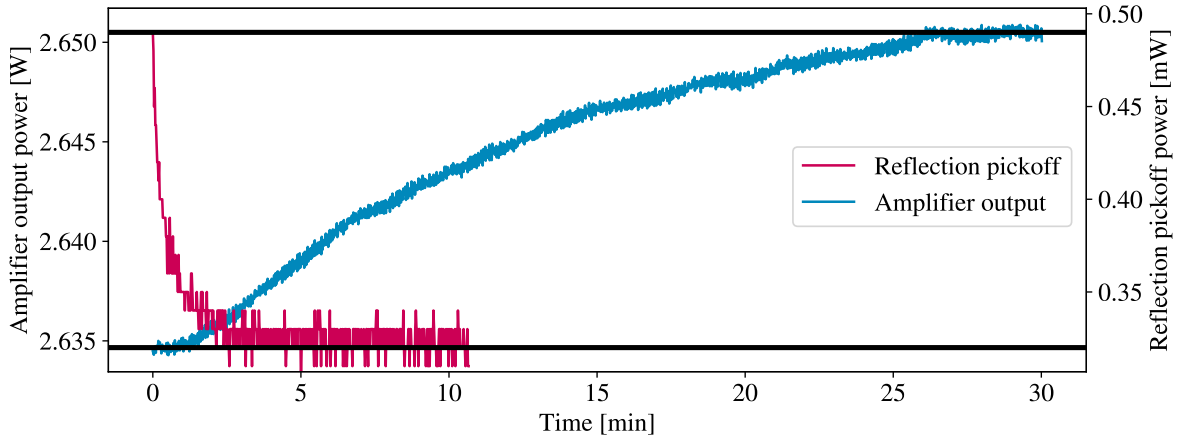

Figure B.4.: Time traces of the RF power measured at the amplifier output (blue) and the bi-directional coupler's reflection pickoff output (red). Both time traces were recorded separately with approximately 10 min of waiting in between. The horizontal black lines indicate the power values in the initial and final stable equilibrium state.

The amplifier output power P_{amp} drifted from 2.6346(3) W up to 2.6505(3) W during approximately 30 min. The power at the bi-directional coupler's reflection pickoff P_{ref} decreased from 0.49(1) mW to 0.32(1) mW during approximately 10 min.

A drift in reflection power can be caused by a drift of the amplifier output power, but can also have a contribution from a drift of the coil-board's resonance frequency. The latter can happen if components on the coil-board heat up as their reactance depends on the temperature. Because the coil-board was driven off-resonantly at 11.60 MHz, it is not surprising to find the reflection power decreasing as, apparently, the coil-board's resonance was shifted towards the applied drive frequency. In a situation where the atomic transition

[1] Mini-Circuits PWR-SEN4GHS

is driven, the drive frequency is set to be on resonance with both the atomic transition and the coil-board. Here, the coil-board's resonance frequency is expected to be shifted away from the drive frequency, and consequently the reflected power should increase.

The drifts of the amplifier output power P_{amp} and the reflection pickoff power P_{ref} combine when considering the power that is distributed to the coil P_{coil}, expressed as

$$P_{\mathrm{coil}} = P_{\mathrm{amp}} \cdot (1 - c) - \frac{1}{c} \cdot P_{\mathrm{ref}} \tag{B.1}$$

where c is the pickoff ratio of the bi-directional coupler. The data sheet of the bi-directional coupler specifies $c = -20\,\mathrm{dB} = 0.01$ [147]. Using the power values that were extracted from the time traces in Figure B.4, corresponding to the initial "cold" state and final stable "hot" equilibrium state, results in a coil power of $P_{\mathrm{coil}} = 2.559(1)\,\mathrm{W}$ at $t = 0$ and $P_{\mathrm{coil}} = 2.592(1)\,\mathrm{W}$ at the new stable equilibrium after $t = 30\,\mathrm{min}$. Therefore, the power distributed to the coil changed by $33(2)\,\mathrm{mW}$ which is a fractional change of $1.25(8) \cdot 10^{-2}$. This fractional change of the coil power is on the same order of magnitude as the fractional power change that was measured directly at the amplifier output. Therefore, a shift of the coil-board's resonance frequency from heating at the coil-board has no significant contribution to drifts of the power that is distributed to the coil. These drifts are mainly caused by power drifts at the amplifier output.

C. Analysis methods

C.1. Bayesian fitting of Ramsey fringe data

By fitting experimentally recorded data of Ramsey fringes with a function described by Equation 2.78, the contrast C as a measure for coherence and the phase ϕ_0 as a measure for detuning were obtained in the context of different experiments in this thesis. Both parameters, the contrast C and the phase ϕ_0, are naturally bounded: Only contrast values of $0 < C < 1$ are physical and, due to the periodicity of Ramsey fringes, the phase can be restricted to the interval $0 \leq \phi_0 < 2\pi$. For Ramsey fringe data with almost unity contrast, as recorded in the dynamical decoupling experiments in Section 5.2.5, a fit based on least squares optimisation methods can return non-physical results for the contrast. In order to constrain the fit parameters C and ϕ_0 to their respective intervals, a fitting method based on a maximum likelihood approach and Bayesian statistics was used, which is discussed in this Section.

The fitting algorithm optimises both fit parameters C and ϕ_0 to maximise the so called *posterior* probability of the model M describing the data D. The posterior probability is calculated by Baye's theorem [148]

$$P(M|D) = \frac{P(D|M)P(M)}{P(D)} \tag{C.1}$$

where $P(D|M)$ is the likelihood of the data describing the model, $P(M)$ is the prior probability and $P(D)$ is the data probability. The probabilities $P(D|M)$, $P(M)$ and $P(D)$ are discussed in the following.

The likelihood is proportional to the frequentist's likelihood

$$P(D|M) \sim L(D|M) = \prod_{i=1}^{N} P(D_i|M) \tag{C.2}$$

for N data points and $P(D_i|M)$ is the probability of a single data point D_i given the model M. For data points that represent an excitation probability p, the underlying distribution is the Binomial distribution [100]

$$P(n, x) = \binom{n}{x} p^x (1-p)^{n-x} \tag{C.3}$$

where n is the number of cycles (number of measurements per data point) and x is the number out of n that the excited state is found. Calculating binomial probabilities is

computationally expensive. To reduce the computational complexity of the fitting routine, data points with Gaussian distribution have been assumed, although this approximation is only valid for large numbers n, x and $n - x$. For the example data shown in Figure C.1a, the number of cycles was $n = 50$ but especially for excitation probabilities close to $p = 0$ and $p = 1$, the numbers x and $n - x$ are small. For $P(D_i|M)$ following a Gaussian distribution where data points D_i have standard deviations σ_i, the logarithmic likelihood is calculated by

$$\log(L(D|M)) = -\frac{1}{2}\sum_{i=1}^{N}\left(\log(2\pi\sigma_i^2) + \frac{(D_i - M_i)^2}{\sigma_i^2}\right). \tag{C.4}$$

The prior probability $P(M)$ represents our knowledge about the model M prior to recording the data D. Here, constraints of the fit parameters are implemented: The prior probability is set to zero for fit parameter values outside the physical intervals. For valid parameter values, a flat prior of $P(M) = 1$ has been used, although this is a rather naive approach [149]. Choosing a non-informative prior is a non trivial task [150].

The data probability $P(D)$ only applies a constant factor to the posterior probability. Therefore it can be ignored (e.g. set to $P(D) = 1$) when optimising the fit parameters for a maximum posterior probability.

Maximising the posterior probability is performed in the following steps: First, a numerical optimisation of the fit parameters is performed using the *scipy.optimise* Python library, starting at a manual guess for the fit parameters. Then, the fit parameter space is sampled by a Markov-Chain-Monte-Carlo (MCMC) method. For the analysis performed in this thesis, the Python-package *emcee* [151] was used. The MCMC initialises 50 walkers at positions in the fit parameter space, randomly scattered around the numerically optimised fit parameters. The walkers perform 2000 steps from which the first 1000 steps are only used as a *burn-in period* for the Markov-Chain trace to stabilise. The burn-in steps are thrown away and the remaining samples of fit parameters $S_i = (C_i, \phi_{0,i})$ approximate the distribution of the posterior probability. Distributions of the individual fit parameters C and ϕ are formed by only taking the respective sample point coordinates C_i and $\phi_{0,i}$. From the distributions of the individual fit parameters, a mean value and a 68.27% confidence interval, corresponding to one standard deviation in case of a Gaussian distribution, are calculated.

Figure C.1 shows an example where the described method has been applied to Ramsey fringe data from the $^{40}Ca^{+}$ ground-state qubit. In the example, the Ramsey experiment had no wait time, no spin echos were performed, and the line-trigger was not active. For the example data, the fit parameters were determined to $C = 0.978^{+10}_{-10}$ and $\phi_0 = 0.014^{+6}_{-6} \cdot \pi$. Error bars for the fit parameters are generally not symmetric.

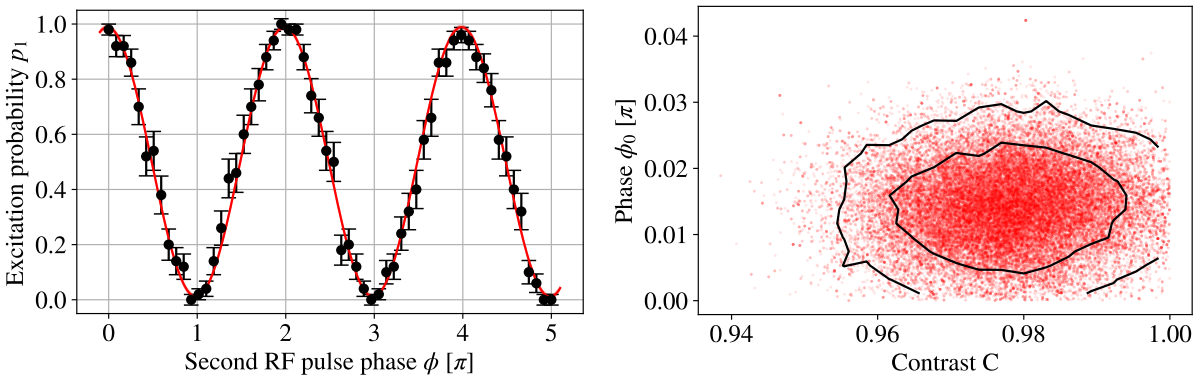

(a) **(b)**

Figure C.1.: a) Ramsey fringes on the $^{40}Ca^{+}$ ground-state qubit at no wait time, with no spin echos and deactivated line-trigger. The recorded data (black points) is fitted (red line) using the Markov-Chain-Monte-Carlo (MCMC) method described in this appendix section. **b)** The posterior distribution of the fit parameters, contrast C and phase ϕ_0, is reconstructed by sampling the fit parameter space (red points). The black lines indicate the boundaries of the 68.27% and 95.5% confidence intervals.

C.2. State tomography with maximum likelihood and Monte-Carlo methods

The single qubit density matrix representation from Equation 2.18 is the foundation for reconstructing an unknown quantum state that was prepared in the laboratory [50]. By preparing and measuring multiple copies of that state, it is possible to estimate the expectation values of the Pauli matrices from the excitation probabilities in the $\pm$, $\pm i$ and the logical basis. However, directly plugging in the estimated probabilities (Equation 2.20), also called a *linear reconstruction*, potentially results in a non-physical density matrix outcome[1] due to statistical fluctuations in the outcomes of a finite number of measurements. An alternative approach is to maximise the likelihood for a density matrix to produce the obtained probabilities [144]. By choosing a physical parametrisation of the density matrix, such a reconstruction will always produce physical density matrices. A discussion of disadvantages of the maximum likelihood method and methods to tackle these problems can be found in the PhD thesis of Thomas Monz [152]. In the following, the method of quantum state tomography with the maximum likelihood approach is exemplified.

In the experiment described in Section 5.2.5, state tomography was performed on three different quantum states that were prepared in the laboratory. These three states are the output states after time evolution from three initial states during the application of dynamical decoupling. For each of the three output states, the qubit's excitation probabilities p_+, p_{+i} and p_1 were measured by projective measurements in the $\pm$, $\pm i$ and

[1] Corresponding to a state vector that is outside of the Bloch sphere.

the logical basis, respectively. Each excitation probability was estimated from up to 60 cycles of the experimental sequence, ending with a projective measurement. For reconstructing a density matrix with the maximum likelihood method, an iterative algorithm [145] starting with a fully mixed state, was used. The algorithm requires estimates from the probabilities p_+, p_-, p_{+i}, p_{-i}, p_0 and p_1. As only p_+, p_{+i} and p_1 were estimated in the experiment, the remaining probabilities were set to $p_- = 1 - p_+$, $p_{-i} = 1 - p_{+i}$ and $p_0 = 1 - p_1$.

For estimating errors, a Monte-Carlo method was used. First, the probability estimates, together with their corresponding numbers of experiment cycles, are used to construct a multinomial probability distribution. The multinomial probability distribution is then used to samples sets of the probabilities p_0, p_1, p_+, p_-, p_{+i} and p_{-i}. For each sampled set of probabilities, an artificial density matrix is reconstructed, using the iterative maximum likelihood algorithm. For each of the three reconstructed output states, 1000 artificial density matrices were sampled. Then, for each sampled density matrix, the fidelity with respect to the original input state was calculated according to Equation 2.21, yielding a distribution of state fidelities among all density matrix samples. From the distribution of state fidelities, a 68.27% confidence interval that surrounds the median value is calculated. Histograms showing the fidelity distributions from the three input states $|0\rangle$, $|+\rangle$ and $|+i\rangle$ are shown in Figure C.2. Combining the sampled fidelity values from all three input states results in the distribution of the average state fidelity, which is shown in the bottom right part of Figure C.2.

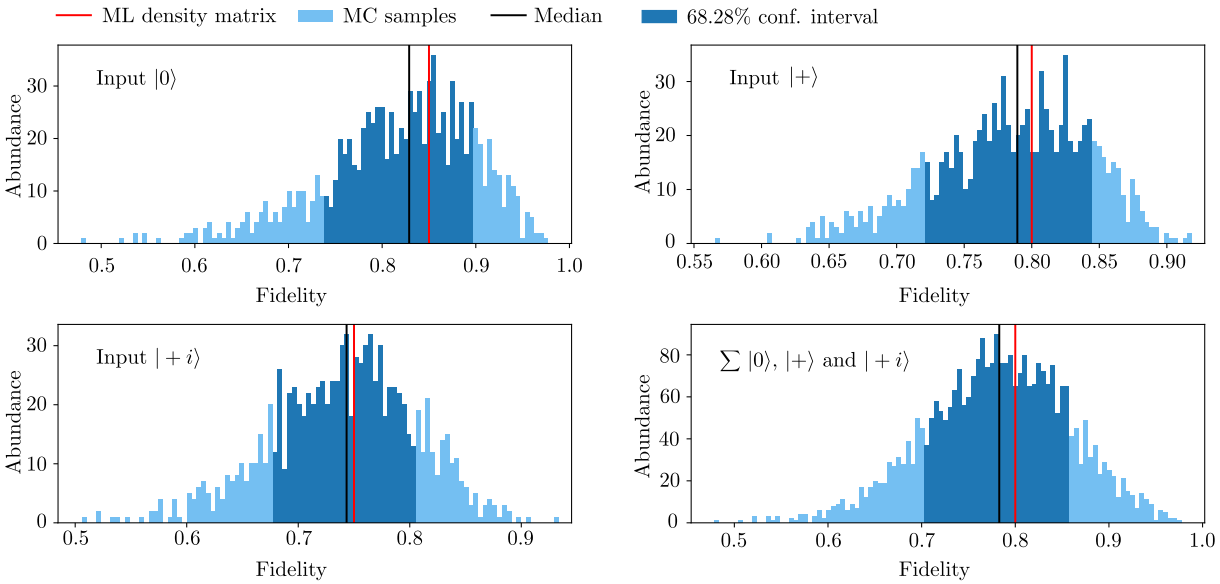

Figure C.2.: Histograms of fidelities from output state Monte-Carlo samples with respect to input states after 4.16 s of XY-4 dynamical decoupling on the $^{40}Ca^{+}$ ground-state qubit. Output state density matrices were reconstructed for the three input states $|0\rangle$, $|+\rangle$ and $|+i\rangle$ by a maximum likelihood method. The fidelity of the maximum likelihood density matrix is indicated by the red line. The dark blue area marks a 68.27% confidence interval around the sampled fidelity distribution's median fidelity value (black line). The plot on the lower right shows the histogram of the combined sampled fidelities from all three cases of the input state, which is associated with the average state fidelity.

Bibliography

[1] T. Demarie and E. Munro. *Quantum Revolutions*. URL: https://medium.com/@quantum_wa/quantum-revolutions-74d9a33b5659. viewed on 18.09.2023.

[2] K. A. Peacock. *The Quantum Revolution: A Historical Perspective*. Bloomsbury Publishing, 2007.

[3] R. Awati. *What is a transistor and how does it work?* URL: https://www.techtarget.com/whatis/definition/transistor. viewed on 21.12.2023.

[4] National Research Council. "Optics in Information Technology and Telecommunications". In: *Harnessing Light: Optical Science and Engineering for the 21st Century*. The National Academies Press, 1998. Chap. 1, pp. 29–82.

[5] National Institute of Standards and Technology. *UTC(NIST) Time Scale*. URL: https://www.nist.gov/pml/time-and-frequency-division/time-realization/utcnist-time-scale-0. viewed on 18.09.2023.

[6] A. G. J. MacFarlane, J. P. Dowling, and G. J. Milburn. "Quantum technology: the second quantum revolution". In: *Philosophical Transactions of the Royal Society of London. Series A: Mathematical, Physical and Engineering Sciences* 361 (2003), pp. 1655–1674. DOI: 10.1098/rsta.2003.1227.

[7] D. Deutsch and R. Jozsa. "Rapid solution of problems by quantum computation". In: *Proceedings of the Royal Society of London. Series A: Mathematical and Physical Sciences* 439 (1992), pp. 553–558. DOI: 10.1098/rspa.1992.0167.

[8] R. P. Feynman. "Simulating physics with computers". In: *International Journal of Theoretical Physics* 21 (1982). DOI: 10.1007/BF02650179.

[9] J. I. Cirac and P. Zoller. "Goals and opportunities in quantum simulation". In: *Nature Physics* 8 (2012). DOI: 10.1038/nphys2275.

[10] N. Gisin and R. Thew. "Quantum communication". In: *Nature Photonics* 1 (2007). DOI: 10.1038/nphoton.2007.22.

[11] V. Giovannetti, S. Lloyd, and L. Maccone. "Quantum-Enhanced Measurements: Beating the Standard Quantum Limit". In: *Science* 306 (2004), pp. 1330–1336. DOI: 10.1126/science.1104149.

[12] F. Arute et al. "Quantum supremacy using a programmable superconducting processor". In: *Nature* 574 (2019), pp. 505–510. DOI: 10.1038/s41586-019-1666-5.

[13] J. Yin et al. “Entanglement-based secure quantum cryptography over 1,120 kilometres”. In: *Nature* 582 (2020), pp. 501–505. DOI: 10.1038/s41586-020-2401-y.

[14] J. Aasi et al. “Enhanced sensitivity of the LIGO gravitational wave detector by using squeezed states of light”. In: *Nature Photonics* 7 (2013), pp. 613–619. DOI: 10.1038/nphoton.2013.177.

[15] H. J. Kimble. “The quantum internet”. In: *Nature* 453 (2008). DOI: 10.1038/nature07127.

[16] C. Monroe and J. Kim. “Scaling the Ion Trap Quantum Processor”. In: *Science* 339 (2013), pp. 1164–1169. DOI: 10.1126/science.1231298.

[17] V. Giovannetti, S. Lloyd, and L. Maccone. “Quantum-Enhanced Measurements: Beating the Standard Quantum Limit”. In: *Science* 306 (2004), pp. 1330–1336. DOI: 10.1126/science.1104149.

[18] K. Beloy et al. “Frequency ratio measurements at 18-digit accuracy using an optical clock network”. In: *Nature* 591 (2021), pp. 564–569. DOI: 10.1038/s41586-021-03253-4.

[19] B. C. Nichol et al. “An elementary quantum network of entangled optical atomic clocks”. In: *Nature* 609 (2022), pp. 689–694. DOI: 10.1038/s41586-022-05088-z.

[20] R. Bondarescu et al. “Ground-based optical atomic clocks as a tool to monitor vertical surface motion”. In: *Geophysical Journal International* 202 (2015), pp. 1770–1774. DOI: 10.1093/gji/ggv246.

[21] J. Flury. “Relativistic geodesy”. In: *Journal of Physics: Conference Series* 723 (2016), p. 012051. DOI: 10.1088/1742-6596/723/1/012051.

[22] D. Gottesman, T. Jennewein, and S. Croke. “Longer-Baseline Telescopes Using Quantum Repeaters”. In: *Phys. Rev. Lett.* 109 (2012), p. 070503. DOI: 10.1103/PhysRevLett.109.070503.

[23] P. W. Shor. “Polynomial-Time Algorithms for Prime Factorization and Discrete Logarithms on a Quantum Computer”. In: *SIAM Journal on Computing* 26 (1997), pp. 1484–1509. DOI: 10.1137/S0097539795293172.

[24] R. L. Rivest, A. Shamir, and L. Adleman. “A Method for Obtaining Digital Signatures and Public-Key Cryptosystems”. In: *Commun. ACM* 21 (1978), pp. 120–126. DOI: 10.1145/359340.359342.

[25] C. H. Bennett and G. Brassard. “Quantum cryptography: Public key distribution and coin tossing”. In: *Theoretical Computer Science* 560 (2014), pp. 7–11. DOI: 10.1016/j.tcs.2014.05.025.

[26] M. H. Devoret and R. J. Schoelkopf. “Superconducting Circuits for Quantum Information: An Outlook”. In: *Science* 339 (2013), pp. 1169–1174. DOI: 10.1126/science.1231930.

[27] W. B. Gao et al. “Coherent manipulation, measurement and entanglement of individual solid-state spins using optical fields”. In: *Nature Photonics* 9 (2015), pp. 363–373. DOI: 10.1038/nphoton.2015.58.

[28] J. L. O’Brien. “Optical Quantum Computing”. In: *Science* 318 (2007), pp. 1567–1570. DOI: 10.1126/science.1142892.

[29] I. Bloch. “Quantum coherence and entanglement with ultracold atoms in optical lattices”. In: *Nature* 453 (2008), pp. 1016–1022. DOI: 10.1038/nature07126.

[30] J. I. Cirac and P. Zoller. “Quantum Computations with Cold Trapped Ions”. In: *Phys. Rev. Lett.* 74 (1995), pp. 4091–4094. DOI: 10.1103/PhysRevLett.74.4091.

[31] F. Schmidt-Kaler et al. “Realization of the Cirac–Zoller controlled-NOT quantum gate”. In: *Nature* 422 (2003). DOI: 10.1038/nature01494.

[32] D. P. DiVincenzo. “The Physical Implementation of Quantum Computation”. In: *Fortschritte der Physik* 48 (2000), pp. 771–783. DOI: 10.1002/1521-3978(200009)48:9/11<771::AID-PROP771>3.0.CO;2-E.

[33] Matthias Keller et al. “Continuous generation of single photons with controlled waveform in an ion-trap cavity system”. In: *Nature* 431 (2004), pp. 1075–1078. DOI: 10.1038/nature02961.

[34] B. B. Blinov et al. “Observation of entanglement between a single trapped atom and a single photon”. In: *Nature* 428 (2004), pp. 153–157. DOI: 10.1038/nature02377.

[35] L. J. Stephenson et al. “High-Rate, High-Fidelity Entanglement of Qubits Across an Elementary Quantum Network”. In: *Phys. Rev. Lett.* 124 (2020), p. 110501. DOI: 10.1103/PhysRevLett.124.110501.

[36] V. Krutyanskiy et al. “Entanglement of Trapped-Ion Qubits Separated by 230 Meters”. In: *Phys. Rev. Lett.* 130 (2023), p. 050803. DOI: 10.1103/PhysRevLett.130.050803.

[37] Stephan Ritter et al. “An elementary quantum network of single atoms in optical cavities”. In: *Nature* 484 (2012), pp. 195–200. DOI: 10.1038/nature11023.

[38] M. Pompili et al. “Realization of a multinode quantum network of remote solid-state qubits”. In: *Science* 372 (2021), pp. 259–264. DOI: doi:10.1126/science.abg1919.

[39] R. Paschotta. *Optical Fiber Communications*. URL: https://www.rp-photonics.com/optical_fiber_communications.html. viewed on 18.09.2023.

[40] M. A. Nielsen and I. L. Chuang. *Quantum Computation and Quantum Information*. Cambridge University Press, 2010.

[41] H.-J. Briegel et al. “Quantum Repeaters: The Role of Imperfect Local Operations in Quantum Communication”. In: *Phys. Rev. Lett.* 81 (1998), pp. 5932–5935. DOI: 10.1103/PhysRevLett.81.5932.

[42] V. Krutyanskiy et al. “Telecom-Wavelength Quantum Repeater Node Based on a Trapped-Ion Processor”. In: *Phys. Rev. Lett.* 130 (2023), p. 213601. DOI: 10.1103/PhysRevLett.130.213601.

[43] A. Sørensen and K. Mølmer. “Quantum Computation with Ions in Thermal Motion”. In: *Phys. Rev. Lett.* 82 (1999), pp. 1971–1974. DOI: 10.1103/PhysRevLett.82.1971.

[44] C.J. Foot. *Atomic Physics*. OUP Oxford, 2005.

[45] L. Viola and S. Lloyd. “Dynamical suppression of decoherence in two-state quantum systems”. In: *Phys. Rev. A* 58 (1998), pp. 2733–2744. DOI: 10.1103/PhysRevA.58.2733.

[46] Rolf Landauer. “Information is a physical entity”. In: *Physica A: Statistical Mechanics and its Applications* 263 (1999), pp. 63–67. DOI: https://doi.org/10.1016/S0378-4371(98)00513-5.

[47] *What is the Bloch Sphere, and why is it crucial to understanding Qubits or Quantum Computing?* URL: https://quantumzeitgeist.com/what-is-the-bloch-sphere-and-why-is-it-crucial-to-understanding-qubits-or-quantum-computing/. viewed on 12.07.2023.

[48] B. Palais, R. Palais, and S. Rodi. “A Disorienting Look at Euler’s Theorem on the Axis of a Rotation”. In: *The American Mathematical Monthly* 116 (2009), pp. 892–909. DOI: 10.4169/000298909X477014.

[49] U. Fano. “Description of States in Quantum Mechanics by Density Matrix and Operator Techniques”. In: *Rev. Mod. Phys.* 29 (1957), pp. 74–93. DOI: 10.1103/RevModPhys.29.74.

[50] J. B. Altepeter, D. F. V. James, and P. G. Kwiat. “Quantum State Tomography”. In: *Quantum State Estimation*. Springer Berlin Heidelberg, 2004, pp. 113–145.

[51] R. Jozsa. “Fidelity for Mixed Quantum States”. In: *Journal of Modern Optics* 41 (1994), pp. 2315–2323. DOI: 10.1080/09500349414552171.

[52] L. K. Grover. “A Fast Quantum Mechanical Algorithm for Database Search”. In: *Proceedings of the Twenty-Eighth Annual ACM Symposium on Theory of Computing*. Association for Computing Machinery, 1996, pp. 212–219. DOI: 10.1145/237814.237866.

[53] H. Klauck. “Quantum Time-Space Tradeoffs for Sorting”. In: *Proceedings of the Thirty-Fifth Annual ACM Symposium on Theory of Computing*. Association for Computing Machinery, 2003, pp. 69–76. DOI: 10.1145/780542.780553.

[54] D. Leibfried et al. “Quantum dynamics of single trapped ions”. In: *Rev. Mod. Phys.* 75 (2003), pp. 281–324. DOI: 10.1103/RevModPhys.75.281.

[55] S. Earnshaw. *On the Nature of the Molecular Forces which Regulate the Constitution of the Luminiferous Ether*. Camb. Phil. Soc. trans. 1839.

[56] H. Dehmelt. "Stored-Ion Spectroscopy". In: *Advances in Laser Spectroscopy*. Springer US, 1983, pp. 153–187.

[57] W. Paul. "Electromagnetic traps for charged and neutral particles". In: *Rev. Mod. Phys.* 62 (1990), pp. 531–540. DOI: 10.1103/RevModPhys.62.531.

[58] C. F. Roos. "Controlling the quantum state of trapped ions". PhD thesis. Universität Innsbruck, 2000.

[59] H.G. Dehmelt. "Radiofrequency Spectroscopy of Stored Ions I: Storage**Part II: Spectroscopy is now scheduled to appear in Volume V of this series." In: vol. 3. Advances in Atomic and Molecular Physics. 1968, pp. 53–72. DOI: https://doi.org/10.1016/S0065-2199(08)60170-0.

[60] J. Jin and D. A. Church. "Precision lifetimes for the Ca^+4p^2P levels: Experiment challenges theory at the 1% level". In: *Phys. Rev. Lett.* 70 (1993), pp. 3213–3216. DOI: 10.1103/PhysRevLett.70.3213.

[61] P. Staanum et al. "Lifetime measurement of the metastable $3d^2D_{5/2}$ state in the $^{40}Ca^+$ ion using the shelving technique on a few-ion string". In: *Phys. Rev. A* 69 (2004), p. 032503. DOI: 10.1103/PhysRevA.69.032503.

[62] *NIST Atomic Spectra Database*. URL: https://physics.nist.gov/PhysRefData/ASD/lines_form.html. viewed on 21.06.2023.

[63] C. R. Nave. *Magnetic Interactions and the Landé g-Factor*. URL: http://hyperphysics.phy-astr.gsu.edu/hbase/quantum/Lande.html. viewed on 12.07.2023.

[64] *The NIST reference on Constants, Units, and Uncertainty - reduced Planck constant*. URL: https://physics.nist.gov/cgi-bin/cuu/Value?hbar. viewed on 13.07.2023.

[65] C. Hempel. "Digital quantum simulation, Schrödinger cat state spectroscopy and setting up a linear ion trap". PhD thesis. Universität Innsbruck, 2014.

[66] J. J. Sakurai and J. Napolitano. *Modern Quantum Mechanics*. Cambridge University Press, 2017.

[67] W. Benenson et al. *Handbook of Physics*. Springer New York, 2006.

[68] G. Morigi et al. "Laser cooling of two trapped ions: Sideband cooling beyond the Lamb-Dicke limit". In: *Phys. Rev. A* 59 (1999), pp. 3797–3808. DOI: 10.1103/PhysRevA.59.3797.

[69] M. Chwalla. "Precision spectroscopy with $^{40}Ca^+$ ions in a Paul trap". PhD thesis. Universität Innsbruck, 2009.

[70] J. Vanier and C. Audoin. *The Quantum Physics of Atomic Frequency Standards*. Adam Hilger, 1989.

[71] *The NIST reference on Constants, Units, and Uncertainty - electron gyromagnetic ratio in MHz/T*. URL: https://physics.nist.gov/cgi-bin/cuu/Value?gammaebar. viewed on 13.07.2023.

[72] *Guide to Passive Devices*. URL: https://www.electronics-tutorials.ws/blog/passive-devices.html. viewed on 13.07.2023.

[73] J. F. James. *A Student's Guide to Fourier Transforms: With Applications in Physics and Engineering*. Cambridge University Press, 2011.

[74] P. Horowitz and W. Hill. *The Art of Electronics*. Cambridge University Press, 2015.

[75] Robert Johnson. *Using complex numbers in circuit analysis and review of the algebra of complex numbers*. URL: https://www.its.caltech.edu/~jpelab/phys1cp/AC%20Circuits%20and%20Complex%20Impedances.pdf. viewed on 18.10.2023.

[76] *Kirchhoffs Circuit Law*. URL: https://www.electronics-tutorials.ws/dccircuits/dcp_4.html. viewed on 13.07.2023.

[77] M. James. *Transfer Functions*. URL: https://users.cecs.anu.edu.au/~Matthew.James/engn2211-2002/notes/frnode1.html. viewed on 13.07.2023.

[78] *Series Resonance Circuit*. URL: https://www.electronics-tutorials.ws/accircuits/series-resonance.html. viewed on 13.07.2023.

[79] *What Is a Transmission Line?* URL: https://www.allaboutcircuits.com/textbook/radio-frequency-analysis-design/real-life-rf-signals/what-is-a-transmission-line/. viewed on 13.07.2023.

[80] S. W. Ellingson, R. Browder, and A. Walz. *Electromagnetics, Volume 1*. Virginia Tech University Libraries, 2018.

[81] O. Duffy. *Telegrapher's Equation*. URL: https://owenduffy.net/transmissionline/TE/TE.htm. viewed on 30.08.2023.

[82] *Derivation of Characteristic Impedance of Transmission line*. URL: https://web.archive.org/web/20180909221832/https://gateece.org/2016/04/16/derivation-of-characteristic-impedance-of-transmission-line/. viewed on 18.10.2023.

[83] S. W. Ellingson. *Voltage Reflection Coefficient*. URL: https://batch.libretexts.org/print/url=https:/eng.libretexts.org/Bookshelves/Electrical_Engineering/Electro-Optics/Book%3A_Electromagnetics_I_(Ellingson)/03%3A_Transmission_Lines/3.12%3A_Voltage_Reflection_Coefficient.pdf. viewed on 12.09.2023.

[84] H. Johnson. *Why Reflections Happen*. URL: http://www.signalintegrity.com/Pubs/edn/whyreflectionshappen.htm. viewed on 13.07.2023.

[85] B. Mishkind. *Why Is 50 Ohms The Standard?* URL: https://www.thebdr.net/why-is-50-ohms-the-standard/. viewed on 13.07.2023.

[86] *Understanding Matching Networks*. URL: https://www.allaboutcircuits.com/textbook/radio-frequency-analysis-design/selected-topics/understanding-matching-networks/. viewed on 13.07.2023.

[87] A. Niknejad. *Resonance and Impedance Matching*. URL: http://bwrcs.eecs.berkeley.edu/Classes/icdesign/ee142_f10/Lectures/ProfNiknejad_chap7.pdf. viewed on 13.07.2023.

[88] D. Fleisch. *A Student's Guide to Maxwell's Equations*. Cambridge University Press, 2008.

[89] D. J. Griffiths. *Introduction to Electrodynamics*. Cambridge University Press, 2017.

[90] *The NIST reference on Constants, Units, and Uncertainty - vacuum magnetic permeability*. URL: https://physics.nist.gov/cgi-bin/cuu/Value?mu0. viewed on 13.07.2023.

[91] C. R. Nave. *Magnetic Field of Current Loop*. URL: http://hyperphysics.phy-astr.gsu.edu/hbase/magnetic/curloo.html. viewed on 13.07.2023.

[92] R. Dengler. "Self inductance of a wire loop as a curve integral". In: *Advanced Electromagnetics* 5 (2016), pp. 1–8. DOI: 10.7716/aem.v5i1.331.

[93] *Inductance of a coil*. URL: https://www.electronics-tutorials.ws/inductor/inductance.html. viewed on 10.07.2023.

[94] "Statistical Optics". In: *Fundamentals of Photonics*. John Wiley & Sons, Ltd, 1991. Chap. 10, pp. 342–383.

[95] N. F. Ramsey. "A Molecular Beam Resonance Method with Separated Oscillating Fields". In: *Phys. Rev.* 78 (1950), pp. 695–699. DOI: 10.1103/PhysRev.78.695.

[96] M. Guevara-Bertsch. "Optical clocks with trapped ions". PhD thesis. Universität Innsbruck, 2023.

[97] P. W. Milonni. "Why spontaneous emission?" In: *American Journal of Physics* 52 (1984), pp. 340–343. DOI: 10.1119/1.13886.

[98] J. Franke. "Magnetic field noise cancellation for quantum simulation experiment with trapped ions". MA thesis. Universität Innsbruck, 2021.

[99] A. Erhard. "Towards scalable quantum computation with trapped ions". PhD thesis. Universität Innsbruck, 2021.

[100] J. R. Taylor. *An Introduction to Error Analysis: The Study of Uncertainties in Physical Measurements*. University Science Books, 1997.

[101] W. Feller. *An Introduction to Probability Theory and Its Applications*. Wiley, 1957.

[102] H. Nyquist. "Thermal Agitation of Electric Charge in Conductors". In: *Phys. Rev.* 32 (1928), pp. 110–113. DOI: 10.1103/PhysRev.32.110.

[103] W. Schottky. "Über spontane Stromschwankungen in verschiedenen Elektrizitätsleitern". In: *Annalen der Physik* 362 (1918), pp. 541–567. DOI: 10.1002/andp.19183622304.

[104] E. L. Hahn. "Spin Echoes". In: *Phys. Rev.* 80 (1950), pp. 580–594. DOI: 10.1103/PhysRev.80.580.

[105] T. Gullion, D. B. Baker, and M. S. Conradi. "New, compensated Carr-Purcell sequences". In: *Journal of Magnetic Resonance (1969)* 89 (1990), pp. 479–484. DOI: 10.1016/0022-2364(90)90331-3.

[106] M. H. Levitt. "Composite pulses". In: *Progress in Nuclear Magnetic Resonance Spectroscopy* 18 (1986), pp. 61–122. DOI: 10.1016/0079-6565(86)80005-X.

[107] P. Drmota et al. "Robust Quantum Memory in a Trapped-Ion Quantum Network Node". In: *Phys. Rev. Lett.* 130 (2023), p. 090803. DOI: 10.1103/PhysRevLett.130.090803.

[108] P. Wang et al. "Single ion qubit with estimated coherence time exceeding one hour". In: *Nature Communications* 12 (2021). DOI: 10.1038/s41467-020-20330-w.

[109] M. K. Gupta et al. "Preserving photon qubits in an unknown quantum state with Knill dynamical decoupling: Towards an all optical quantum memory". In: *Phys. Rev. A* 91 (2015), p. 032329. DOI: 10.1103/PhysRevA.91.032329.

[110] L. Viola, E. Knill, and S. Lloyd. "Dynamical Decoupling of Open Quantum Systems". In: *Phys. Rev. Lett.* 82 (1999), pp. 2417–2421. DOI: 10.1103/PhysRevLett.82.2417.

[111] G. T. Genov et al. "Arbitrarily Accurate Pulse Sequences for Robust Dynamical Decoupling". In: *Phys. Rev. Lett.* 118 (2017), p. 133202. DOI: 10.1103/PhysRevLett.118.133202.

[112] A. M. Souza, G. A. Álvarez, and D. Suter. "Robust Dynamical Decoupling for Quantum Computing and Quantum Memory". In: *Phys. Rev. Lett.* 106 (2011), p. 240501. DOI: 10.1103/PhysRevLett.106.240501.

[113] Lanyon B. P. *Distributed Quantum Systems*. URL: https://quantumoptics.at/en/research/photon-conversion.html. viewed on 30.08.2023.

[114] J. Schupp. "Interface between trapped-ions qubits and travelling photons with close-to-optimal eficiency". PhD thesis. Universität Innsbruck, 2022.

[115] M. Meraner. "A photonic quantum interface between trapped-ions and the telecom C-band". PhD thesis. Universität Innsbruck, 2022.

[116] V. Krčmarský. "A trapped-ion quantum network over 230m". PhD thesis. Universität Innsbruck, to be published.

[117] A. Winkler. "Frequency Stabilization of a 729 nm Ti:Sa Laser for Qubit Manipulation in Trapped Calcium Ions". MA thesis. Universität Innsbruck, 2023.

[118] M. Guggemos. "Precision spectroscopy with trapped $^{40}Ca^{+}$ and $^{27}Al^{+}$ ions". PhD thesis. Universität Innsbruck, 2017.

[119] M. Canteri. "Single-atom-focused laser for photon generation and qubit control". MA thesis. Universität Innsbruck, 2020.

[120] V. Krutyanskiy et al. *Multimode ion-photon entanglement over 101 kilometers of optical fiber*. 2023. DOI: 10.48550/arXiv.2308.08891.

[121] C. M. da Silva Baptista Russo. "Photon statistics of a single ion coupled to a high-finesse cavity". PhD thesis. Universität Innsbruck, 2008.

[122] "Acousto-Optics". In: *Fundamentals of Photonics*. John Wiley & Sons, Ltd, 1991. Chap. 20, pp. 799–831.

[123] *ULE Corning Code 7972 Ultra Low Expansion Glass*. URL: https://www.corning.com/media/worldwide/csm/documents/7972%20ULE%20Product%20Information%20Jan%202016.pdf. viewed on 19.07.2023.

[124] H. Hainzer. "Laser Locking For Trapped-Ion Quantum Networks". MA thesis. Universität Innsbruck, 2018.

[125] P. Schindler. "Frequency synthesis and pulse shaping for quantum information processing with trapped ions." Diploma thesis. Universität Innsbruck, 2008.

[126] M. Ramm et al. "Precision Measurement Method for Branching Fractions of Excited $P_{1/2}$ States Applied to $^{40}Ca^{+}$". In: *Phys. Rev. Lett.* 111 (2013), p. 023004. DOI: 10.1103/PhysRevLett.111.023004.

[127] A. H. Myerson et al. "High-Fidelity Readout of Trapped-Ion Qubits". In: *Phys. Rev. Lett.* 100 (2008), p. 200502. DOI: 10.1103/PhysRevLett.100.200502.

[128] W. M. Itano et al. "Quantum projection noise: Population fluctuations in two-level systems". In: *Phys. Rev. A* 47 (1993), pp. 3554–3570. DOI: 10.1103/PhysRevA.47.3554.

[129] P. S. Laplace. "Essai philosophique sur les probabilités". In: (1814).

[130] J. Weisberg. *Laplace's rule of succession*. URL: https://jonathanweisberg.org/post/inductive-logic-2/. viewed on 21.09.2023.

[131] H. C. Nägerl et al. "Addressing and Cooling of Single Ions in Paul Traps". In: *Fortschritte der Physik* 48 (2000), pp. 623–636. DOI: 10.1002/(SICI)1521-3978(200005)48:5/7<623::AID-PROP623>3.0.CO;2-S.

[132] G. Kirchmair. "Quantum non-demolition measurements and quantum simulation". PhD thesis. Universität Innsbruck, 2010.

[133] P. Jurcevic. "Quantum Computation and Many-Body Physics with Trapped Ions". PhD thesis. Universität Innsbruck, 2017.

[134] *USB Power Sensor PWR-4GHS*. Mini-Circuits. URL: https://www.minicircuits.com/pdfs/PWR-4GHS.pdf.

[135] J. D. Siverns et al. "On the application of radio frequency voltages to ion traps via helical resonators". In: *Applied Physics B* 107 (2012), pp. 921–934. DOI: 10.1007/s00340-011-4837-0.

[136] Y. Park et al. "A Feedback Control Method to Maintain the Amplitude of the RF Signal Applied to Ion Traps". In: *Applied Sciences* 11 (2021). DOI: 10.3390/app11020837.

[137] D. Kiesenhofer et al. "Controlling Two-Dimensional Coulomb Crystals of More Than 100 Ions in a Monolithic Radio-Frequency Trap". In: *PRX Quantum* 4 (2023), p. 020317. DOI: 10.1103/PRXQuantum.4.020317.

[138] C. F. Roos et al. "Quantum information processing and Ramsey spectroscopy with trapped ions". In: *Laser Spectroscopy*, pp. 53–62. DOI: 10.1142/9789812813206_0005.

[139] H. W. Ott. "Electromagnetic Compatibility Engineering". In: Wiley Publishing, 2009, pp. 142–147.

[140] M. Körber et al. "Decoherence-protected memory for a single-photon qubit". In: *Nature Photonics* 12 (2018). DOI: 10.1038/s41566-017-0050-y.

[141] *RF-Lambda - PIN, GaAs and GaN Switch (High Speed)*. URL: https://www.rflambda.com/search_switchers.jsp. viewed on 25.07.2023.

[142] D. Niemietz. "Nondestructive Detection of Photonic Qubits with Single Atoms in Crossed Fiber Cavities". PhD thesis. Technische Universität München, 2021.

[143] D. P. L. Aude Craik. "Near-field microwave addressing of trapped-ion qubits for scalable quantum computation". PhD thesis. University of Oxford, 2016.

[144] Z. Hradil et al. "Maximum-Likelihood Methods in Quantum Mechanics". In: *Quantum State Estimation*. Springer Berlin Heidelberg, 2004, pp. 59–112.

[145] J. Řeháček, Z. Hradil, and M. Ježek. "Iterative algorithm for reconstruction of entangled states". In: *Phys. Rev. A* 63 (2001), p. 040303. DOI: 10.1103/PhysRevA.63.040303.

[146] I. Pogorelov et al. "Compact Ion-Trap Quantum Computing Demonstrator". In: *PRX Quantum* 2 (2021), p. 020343. DOI: 10.1103/PRXQuantum.2.020343.

[147] *Bi-Directional Coupler ZFBDC20-61HP+*. Mini-Circuits. URL: https://www.minicircuits.com/pdfs/ZFBDC20-61HP+.pdf.

[148] Phil Gregory. *Bayesian Logical Data Analysis for the Physical Sciences: A Comparative Approach with Mathematica® Support*. Cambridge University Press, 2005.

[149] *Lost causes in statistics II: Noninformative Priors*. URL: https://normaldeviate.wordpress.com/2013/07/13/lost-causes-in-statistics-ii-noninformative-priors/comment-page-1/. viewed on 13.10.2023.

[150] Robert E. Kass and Larry Wasserman. "The Selection of Prior Distributions by Formal Rules". In: *Journal of the American Statistical Association* 91 (1996), pp. 1343–1370. DOI: 10.1080/01621459.1996.10477003.

[151] D. Foreman-Mackey and contributors. *emcee - Fitting a model to data*. URL: https://emcee.readthedocs.io/en/stable/tutorials/line/. viewed on 11.10.2023.

[152] T. Monz. "Quantum information processing beyond ten ion-qubits". PhD thesis. Universität Innsbruck, 2011.